Lanthanide-doped upconversion nanomaterials

Liangliang Liang, Jiaye Chen, and Xiaogang Liu, National University of Singapore, Singapore, Singapore

1 Introduction

As a special class of nonlinear optical nanomaterials, lanthanide-doped upconversion nanocrystals can convert near-infrared (NIR) excitation into programmable emission from the ultraviolet (UV) to NIR regions.[1–6] Upconversion nanocrystals exhibit tunable luminescent lifetimes, sharp emission bandwidths, large anti-Stokes shifts, and high photostability.[7–9] Moreover, their optical properties can be extensively customized by controlling the material composition and the core-shell structure.[10–15] With such intrinsic characteristics, upconversion nanocrystals offer solutions for challenging problems in photonic and biological applications.[16–27] For example, characteristics, such as luminescence saturation, long excited-state lifetime and high photostability, make upconversion nanocrystals promising biomarkers for low-power continuous-wave (CW) mediated super-resolution imaging.[28–32] Meanwhile, upconversion nanocrystals are also suitable for low-threshold UV-Vis-NIR lasing applications because of their tunable emission bands and long luminescence lifetimes.[33–35] Moreover, with a responsivity beyond 1000 nm, upconversion nanocrystals have been integrated into photovoltaic devices, such as photodetectors, to extend their spectral responses.[36–38] What's more, NIR light exhibits relatively low attenuation in biological tissues, making upconversion nanocrystals ideal as optogenetic nano-light sources to activate or silence neuronal activities.[39–46] In this book chapter, we first introduce basic functional principles of lanthanide-doped upconversion nanocrystals. We summarize complex energy harvesting, transport, and dissipation in the upconversion system, as well as general approaches for optimizing energy flux pathways. Moreover, we highlight recent developments in boosting emission brightness. We also discuss the latest research directions in developing upconversion approaches for emerging applications. Although the IUPAC-recommended group name is "lanthanoids," to avoid confusion with other groups where the "ide" ending indicates a negative charge, in this chapter we have followed the still common practice in using the old group name, "lanthanides."

2 Functional principles of lanthanide upconversion

Lanthanide upconversion is usually carried out in inorganic host lattices doped with lanthanide ions. Upon NIR excitation, these upconversion nanocrystals emit photons of higher energy than the photons used for excitation (Fig. 1A). Hence, the term 'upconversion' refers to what occurs in the frequency domain. Quite unlike traditional nonlinear optical transitions, such as multiphoton absorption luminescence[47,48] and second/third-harmonic generation luminescence,[49] the nonlinear process of lanthanide upconversion is orders of magnitude more efficient. This is because lanthanide-mediated upconversion can be achieved through a sequential population of physically existing intermediate excited states with ultralong lifetimes. The lanthanide series consists of 15 metallic elements in the periodic table with atomic numbers from 57 to 71. Fig. 1B shows the energy levels of commonly used trivalent lanthanide dopants (Ln^{3+}) in upconversion nanocrystals. Most of them have multiple excited electronic energy levels that are close enough to provide each lanthanide ion with manifold absorption and emission bands. The emission color and corresponding optical transitions of commonly used lanthanide emitters are illustrated in Fig. 1C. Lanthanide luminescence covers the spectral region from the UV to NIR, with ample opportunities for luminescence modulation in the visible region. Notably, fast nonradiative relaxation occurs due to the narrow energy gap between adjacent energy levels of lanthanide ions, with

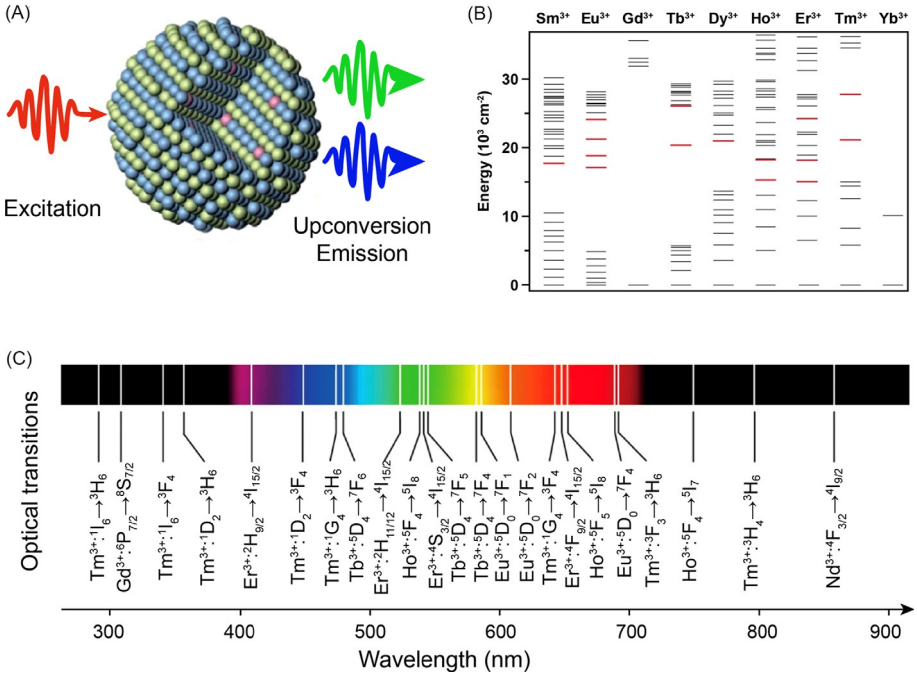

Fig. 1 (A) Illustration of the lanthanide upconversion process by which high-energy photons are emitted from lanthanide-doped nanocrystals after absorbing low-energy photons. (B) Energy levels of lanthanide dopants typically used for photon upconversion. (C) Typical emission colors of lanthanide ions and their corresponding energy level transitions.

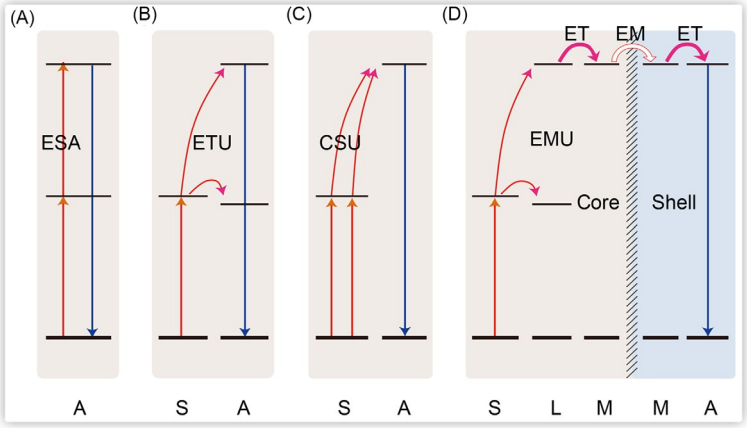

Fig. 2 Typical upconversion mechanisms. (A) Excited-state absorption (ESA). (B) Energy transfer upconversion (ETU). (C) Cooperative sensitization upconversion (CSU). (D) Energy migration upconversion (EMU). *A*, activator; *S*, sensitizer; *L*, Ladder; *M*, Migrator.

only specific radiative transitions being intensive at room temperature. Moreover, the electronic energy levels of each lanthanide ion are quite different, and these differences endow lanthanide systems with numerous options for frequency modulation. Compared to organic dyes and quantum dots, lanthanide ions feature much narrower band widths, with full widths at half-maximum (FWHM) smaller than 20 nm. Because electric dipole transitions are prolonged due to parity-forbidden intra-4f transitions, lanthanide luminescence displays micro- and even millisecond lifetimes, over three orders of magnitude longer than those of organic dyes and quantum dots.

Lanthanide-mediated upconversion mechanisms are usually classified into four types: excited-state absorption (ESA),[50] energy transfer upconversion (ETU),[51] cooperative sensitization upconversion (CSU),[52] and energy migration upconversion (EMU).[53,54] For nanocrystals doped only with activators, the whole process, including photon absorption, intermediated state population, and high energy photon emission, occurs among doped activators (Fig. 2A). However, lanthanide sensitizers are usually codoped with activators to enhance upconversion efficiency. This is because of the low absorption cross-section of commonly used lanthanide activators (such as Er^{3+}, Ho^{3+}, and Tm^{3+}). For energy transfer upconversion, sensitizers with large absorption cross-sections (Yb^{3+} and Nd^{3+}) are suitable for harvesting and transferring incident NIR photons to adjacent activators (Fig. 2B). Subsequently, energy

transfer to activators occurs, usually governed by Förster resonance energy transfer (FRET). The probability of FRET becomes negligible if there is no spectral overlap between the sensitizer and the activator. However, if the photon energy of the activator (e.g., Tb^{3+}, Eu^{3+}, Dy^{3+}, or Sm^{3+}) is nearly twice that of the sensitizer (e.g., Yb^{3+}), photon upconversion can still occur through cooperative sensitization (Fig. 2C). Cooperative sensitization upconversion is much less efficient than energy transfer upconversion, and a high excitation photon flux is generally required to trigger bright luminescence. To achieve upconversion for lanthanide ions without intermediate states, energy migration upconversion involving core-shell nanoparticles can be employed (Fig. 2D). In the core, a sensitizer ion first transfers its excitation energy to an activator ladder ion. The energy transfer from the high-lying excited state of the ladder to a migrator ion then occurs. Activators in the shell layer then accept the energy from the migrator ion sublattice. Through this energy migration design, upconversion luminescence can be achieved for lanthanide activators that cannot be directly sensitized by Yb^{3+}.

Despite different existential mechanisms, one should contemplate that many upconversion processes coincide in single nanoparticles. As a case in point, ESA through a single type of lanthanide ion (e.g., Er^{3+} and Tm^{3+}) competes with ETU because of the energy transfer between adjacent activators, especially at high doping concentrations. Moreover, ETU and EMU are frequently used to customize upconversion nanocrystals with specific optical characteristics.

3 Manipulation of energy transfer

Although lanthanide-doped crystals offer much more efficient upconversion processes than multiphoton absorption and second-harmonic generation, their energy conversion efficiency is still extremely low compared to luminescent organic dyes and quantum dots.[4,55] Let's say $NaYF_4$:Yb/Er is the most frequent upconversion design for bioimaging applications. However, its absolute quantum yield is usually lower than 1% under 10 W cm^{-2} laser excitation.[56] An intense laser is generally required to achieve upconversion, but with potential overheating or safety issues.[57] In addition, the low brightness of upconversion nanocrystals may also hinder their applications in super-resolution imaging, single-particle tracking, lasing, and optogenetics.

For an upconversion process to proceed, incident NIR energy should be first harvested by sensitizers. Activators are activated by sensitizers through energy transfer and further populated to excited states. High-energy photons are released to complete the upconversion process. During photon upconversion, overall conversion efficiency is determined by three key steps: energy harvesting, energy transfer, and energy dissipation. Next, we summarize commonly used strategies for achieving efficient upconversion by optimizing the three energy flow steps.

3.1 Enhancing NIR energy harvesting

Although lanthanide activators Er^{3+}, Ho^{3+} and Tm^{3+} can harvest incident NIR photons directly through ground-state absorption (GSA) and ESA, activator-only upconversion design has been rarely used due to its low conversion efficiency. This is because the absorption cross-sections of these activators are extremely small (ca. 1×10^{-21} cm^2) since 4*f*-4*f* absorption transitions are parity forbidden.[58] Therefore, as illustrated in Fig. 3A, almost all currently used upconversion nanocrystals are sensitized with ions having larger absorption cross-sections. With an absorption cross-section of about 1.3×10^{-20} cm,[2] almost one order of magnitude larger than the abovementioned activators, Yb^{3+} is the most frequently used sensitizer for achieving high-efficiency upconversion. Upon NIR excitation (900–1050 nm), efficient transfer of excitation energies can occur from Yb^{3+} to adjacent activators (e.g., Er^{3+}, Ho^{3+}, or Tm^{3+}), populating their high-lying excited states for upconversion luminescence. Apart from large absorption cross-sections, high doping of Yb^{3+} sensitizers (>20% in molar ratio) can promote NIR harvesting.

Although Yb^{3+}-sensitized upconversion provides handy design and high efficiency, it only responds to single-wavelength excitation at 980 nm. To overcome this deficiency, Nd^{3+} can be codoped as a sensitizer with Yb^{3+} for cascade energy transfer. Unlike Yb^{3+}, Nd^{3+} features multiple absorption bands in the optical window (730 nm, 800 nm, 860 nm), largely mitigating

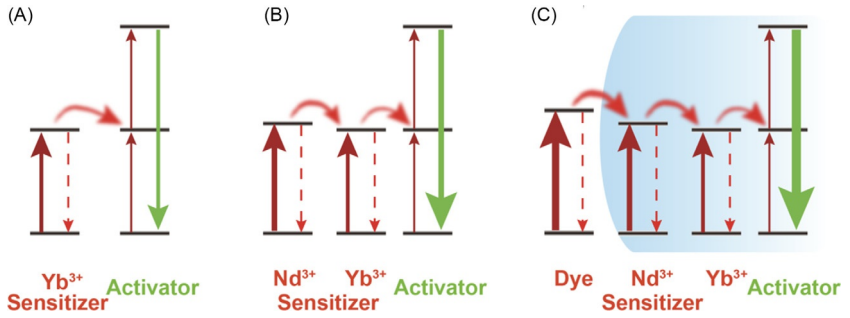

Fig. 3 Three major schemes of NIR-harvesting using lanthanide-doped upconversion nanocrystals. (A) Yb^{3+} sensitization, (B) Nd^{3+}/Yb^{3+} co-sensitization, (C) organic dye-mediated upconversion sensitization. Printed with permission from Ref. Liang, L.; Qin, X.; Zheng, K.; Liu, X. *Acc. Chem. Res.* **2019**, *52*, 228–236.

solution overheating, typically associated with continuous 980-nm excitation.[59–61] As shown in Fig. 3B, Nd^{3+}-sensitized excitation energy can be transferred to Yb^{3+} and activators in succession. Notably, the absorption cross-section of Nd^{3+} is one order-of-magnitude larger than that of Yb^{3+}. Energy transfer efficiency from Nd^{3+} to Yb^{3+} is exceptionally high (>50%); therefore, one can expect much brighter upconversion nanocrystals co-sensitized with Nd^{3+} and Yb^{3+} than those sensitized with solely Yb^{3+}. However, direct contact between Nd^{3+} sensitizers and activators may severely quench luminescence. In this regard, core-shell structures are usually designed to ensure spatial isolation for bright emission.[62]

The absorption cross-section of organic molecules is around 1×10^{-16} cm^2, over three orders of magnitude larger than those of lanthanides. To boost light-harvesting of lanthanide-doped nanoparticles, organic dyes have been introduced.[63,64] Organic dyes can be tethered to nanoparticle surfaces for enhanced NIR absorption (Fig. 3C). Nd^{3+} and Yb^{3+} sensitizers are activated by energy transfer from dye molecules to Nd^{3+} and Yb^{3+}. Subsequent energy transfer from Yb^{3+} to emitters gives rise to luminescence. Although dye sensitization can enhance upconversion luminescence, especially under low-power excitation, this design only works well in low-oxygen environments where limited triplet states are quenched.[65,66] Moreover, dye sensitizers generally have low photostability, making their long-term application impractical.

3.2 Optimization of energy transfer pathways

Energy cross-talk between lanthanide activators is usually the major factor leading to severe luminescence quenching (Fig. 4A).[67,68] Excited-state depopulation of upconversion nanocrystals with low activator doping through cross-relaxation is insignificant. However, with an increase in activator concentration, upconversion luminescence may increase initially but then declines rapidly. Although more activators facilitate energy transfer from sensitizers, energy cross-talk between activators occurs, depopulating excited states and ultimately luminescence intensity. Furthermore, energy back transfer from activators to sensitizers depopulates the excited states.

Quite unlike Yb^{3+}, the energy levels of Nd^{3+} are highly complex. Significant energy cross-talk between common activators (Er^{3+}, Ho^{3+}, and Tm^{3+}) and Nd^{3+} sensitizer can occur.[60] For Nd^{3+}-sensitized upconversion nanocrystals, core-shell structures can be employed to tune luminescence (Fig. 4B). Confinement of Nd^{3+} and activators in different spatial layers substantially mitigates energy cross-talk. It should be noted that Yb^{3+} sensitizers are doped in both core and shell layers as linkers to bridge energy transfer from Nd^{3+} to activators. An additional layer of doped Yb^{3+} is usually inserted between layers of Nd^{3+} and activators to eliminate cross-relaxation through the core-shell interface.

An interesting observation for activators is that the optimal doping concentration can be substantially increased. For example, for the commonly used $NaYF_4$:Yb/Er host, the optimum doping concentration of Er^{3+} is around 2%. However, this value can be increased to 20% under 10^6 W cm^2 excitation.[69] Under low-power irradiance, a high doping concentration leads to severe cross-relaxation between activators, and high-lying excited energy levels are likely to undergo significant depopulation (Fig. 4C). However, when irradiance is markedly increased, intermediate excited states are immediately populated to higher excited states through ESA, albeit energy cross-relaxation continues to occur. In other words, a high photon flux could combat cross-relaxation and alleviate the overall depopulation of excited states, making high-concentration doping possible. For applications involving high excitation irradiance, such as super-resolution imaging, highly doped upconversion nanocrystals are usually employed. For $NaGdF_4$ nanocrystals codoped with Yb/Er ions, the luminescence intensity of 2% Er-activated samples is higher than those doped with 20% Er^{3+} when the excitation power is below 3×10^5 W cm^2 (Fig. 4D). However, with increased power density, the luminescence intensity of 2% Er-activated samples saturates while their counterparts show drastically increased intensities. Microscopic imaging of single nanoparticles indicates that the emitted photons from low doping samples are suppressed by highly doped ones at high excitation irradiance (Fig. 4E). Similar phenomena have also been verified using Tm^{3+}- or Nd^{3+}-activated upconversion nanocrystals (Fig. 4F and G).[70,71]

As described above, energy mitigation represents an effective way of ensuring bright upconversion luminescence. Notably, this method enhances all emission bands without selectivity. However, multiple emission bands may interfere with luminescence detection and post-analysis. Introducing energy reservoir centers can improve the luminescence intensity of a specified emission band. Upon NIR excitation, activators in high-lying excited states depopulate by transferring their energy to adjacent reservoir centers. Subsequently, energy back transfer from reservoir centers to activators populates low-lying excited states, enhancing photon emission at long wavelengths. Energy reservoir centers can redistribute activator populations by promoting low-lying excited states.

Mn^{2+} is frequently used as the energy reservoir in lanthanide-doped upconversion nanocrystals to achieve quasi-single-band luminescence.[72,73] Upon Mn^{2+} codoping, the green emission band of Yb^{3+}/Er^{3+}-codoped $KMnF_3$ nanocrystals disappears, leaving only a red emission band (Fig. 5A). Similarly, for Yb^{3+}/Tm^{3+}-codoped samples, only 800-nm NIR emission is detectable. After population with Er^{3+}/Tm^{3+} ions in high-lying excited states, Mn^{2+} reservoir centers transfer energy back to activators for population redistribution in low-lying excited states.

In addition to Mn^{2+}, Tm^{3+} has been used as the energy reservoir to enhance upconversion emission at long wavelengths.[74] Quasi-single-band red emission can be further enhanced by codoping Tm^{3+} with Er^{3+} in $NaErF_4$ nanocrystals. As an energy reservoir, Mn^{2+} performs much better than Tm^{3+}, but the latter is much easier to integrate into $NaLnF_4$ lattices.

Yb^{3+} can also work as an energy reservoir center in special lattice environments.[75] In KYb_2F_7:Er^{3+} nanocrystals, Yb^{3+} and Er^{3+} ions distribute in arrays of tetrad clusters (Fig. 5B). Yb-Yb distances between inter clusters are much larger than those between

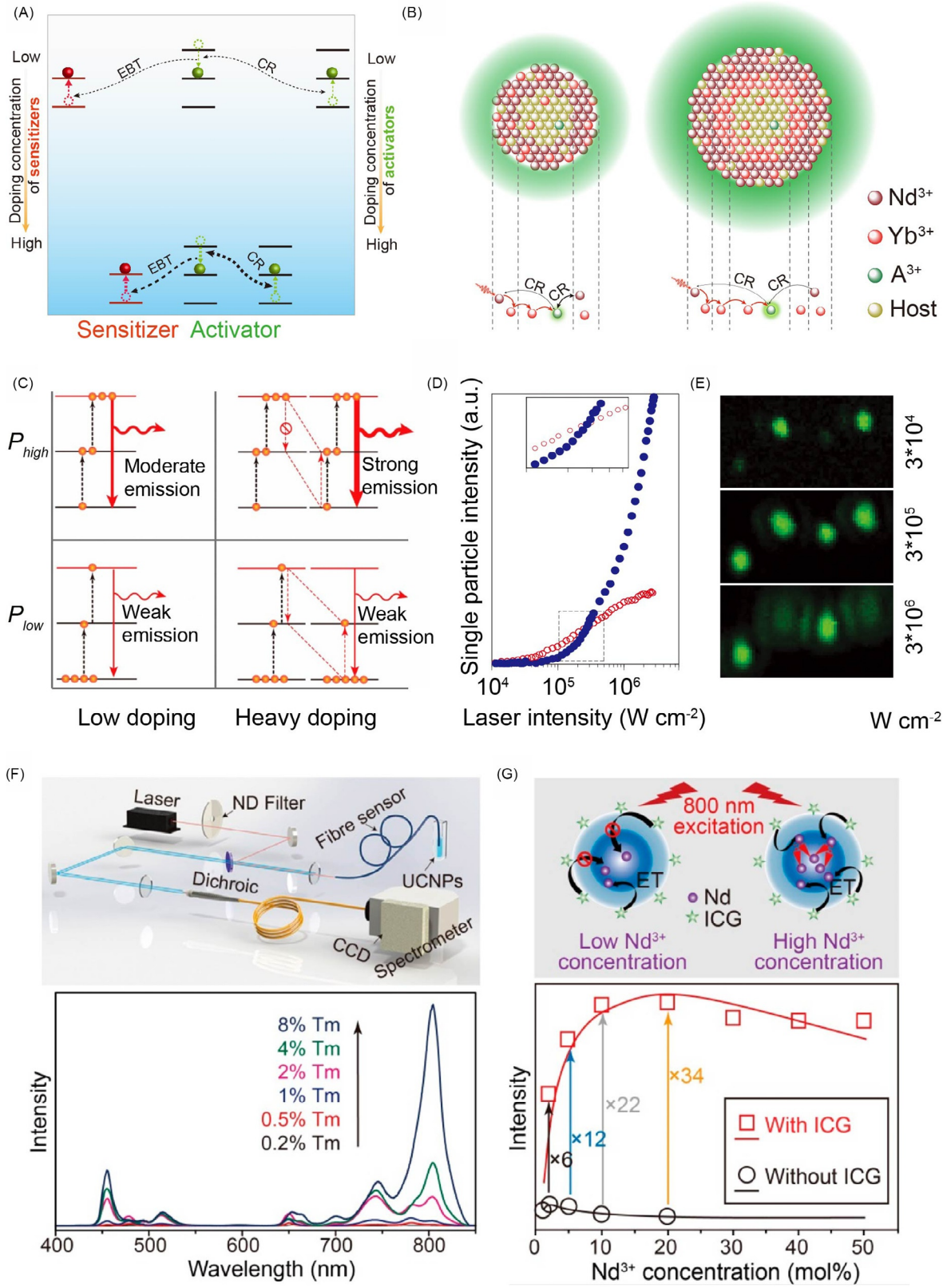

Fig. 4 (A) Energy cross-talk between activators and sensitizers. EBT: energy back transfer; CR: cross-relaxation. (B) Design of core-shell upconversion nanocrystals with minimized energy cross-talk. (C) Dependence of excited-state population in upconversion nanocrystals on dopant concentration and power density. (D) Luminescence intensity of single 8-nm upconversion nanocrystals with 20% (blue circles) and 2% (red circles) Er^{3+}, each codoped with 20% Yb^{3+}. (E) Confocal luminescence images of single UCNPs containing a mixture of 2% and 20% Er^{3+}. (F) Emission spectra of $NaYF_4$:Yb/Tm (20/0.2–8 mol%) UCNPs as a function of Tm^{3+} doping concentration upon 980 nm excitation ($\sim 2.5 \times 10^6$ W cm^2) through a microstructure optical fiber (top panel). (G) Schematic of ICG-sensitized upconversion in $NaYF_4$:Nd nanoparticles (top panel) and emission intensity of $NaYF_4$:Nd (1–50 mol%) nanocrystals versus Nd^{3+} doping concentration with and without Indocyanine green (ICG) sensitization (bottom panel). (A, B) Printed with permission from Ref. Liang, L.; Qin, X.; Zheng, K.; Liu, X *Acc. Chem. Res.* **2019**, *52*, 228–236. Copyright © 2018 American Chemical Society. (D, E) Printed with permission from Ref. Gargas, D. J. et al. *Nat. Nanotechnol.* **2014**, *9*, 300–305. Copyright © 2014, Nature Publishing Group. (F) Printed with permission from Ref. Zhao, J. et al. *Nat. Nanotechnol.* **2013**, *8*, 729–734. Copyright © 2013, Nature Publishing Group. (G) Printed with permission from Ref. Wei, W. et al. *J. Am. Chem. Soc.* **2016**, *138*, 15130–15133. Copyright © 2016 American Chemical Society.

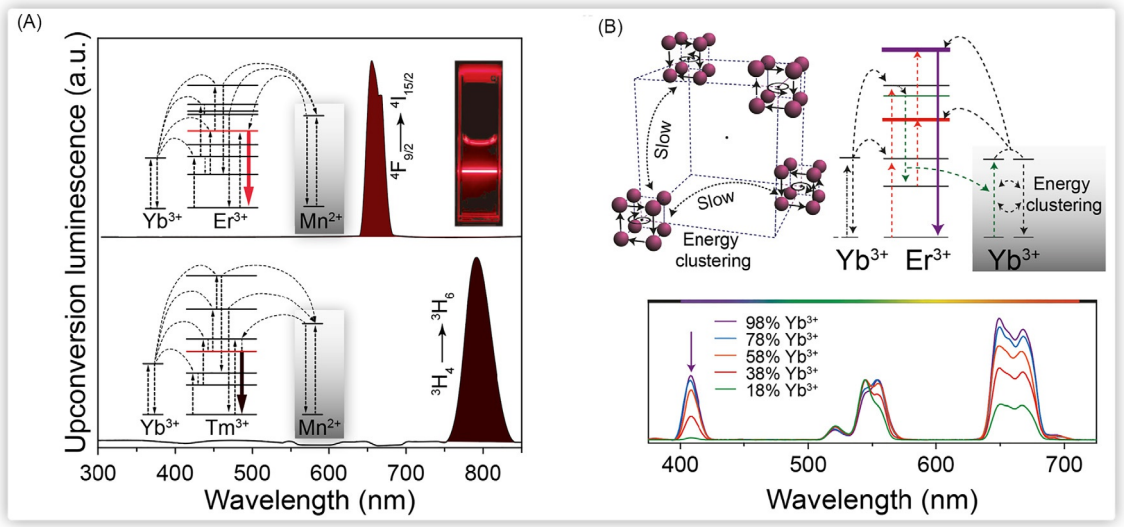

Fig. 5 (A) Working mechanism of upconversion nanocrystals with Mn^{2+} ions as reservoir centers and single-band emission spectra of $KMnF_3$:Yb/Er (top panel) and $KMnF_3$:Yb/Tm (bottom panel) nanocrystals. (B) Illustration of topological energy clustering within crystal sublattice and population processes of upconversion nanocrystals with Yb^{3+} energy clusters (top panel). Emission spectra of KYb_2F_7:Er/Lu (2/0–80 mol%) nanocrystals upon 980 nm excitation (bottom panel). (A) Printed with permission from Ref. Wang, J.; Wang, F.; Wang, C.; Liu, Z.; Liu, X. *Angew. Chem. Int. Ed.* **2011**, *123*, 10553–10556. Copyright © 2011 WILEY-VCH Verlag GmbH & Co. KGaA, Weinheim. (B) Printed with permission from Ref. Wang, J. et al. *Nat. Mater.* **2014**, *13*, 157–162. Copyright © 2013, Nature Publishing Group.

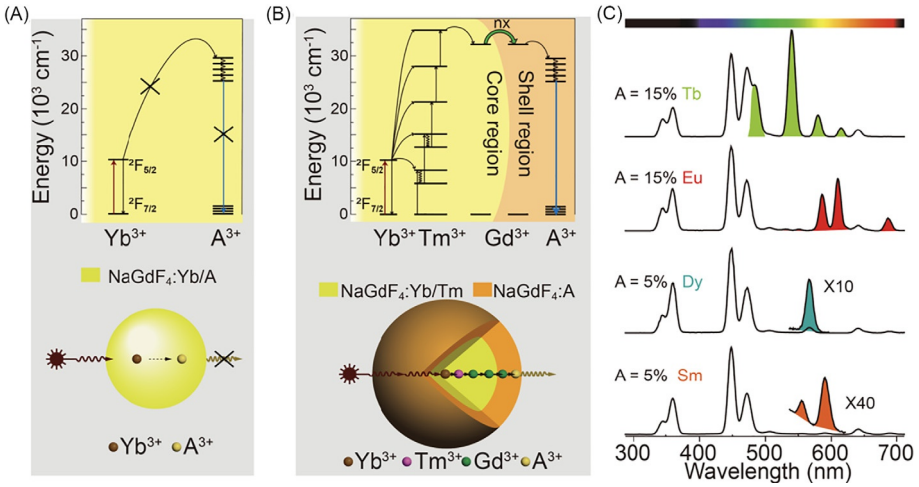

Fig. 6 Proposed energy transfer pathway and schematic design for (A) energy transfer upconversion with a large gap and (B) energy migration-mediated upconversion. (C) Energy migration upconversion emission spectra of nanocrystals with different activators (Tb^{3+}, Eu^{3+}, Dy^{3+}, Sm^{3+}). (B and C) Printed with permission from Ref. Wang, F. et al. *Nat. Mater.* **2011**, *10*, 968–973. Copyright © 2011, Nature Publishing Group.

intra-clusters. Excitation energy can be trapped in every cluster, increasing Yb^{3+}-Er^{3+} interaction. The much enhanced short-wavelength emission provides direct evidence of excitation energy confinement. However, the existing energy reservoir strategy is limited to a small set of lanthanides.

For efficient energy transfer, the spectral overlap between adjacent donors/acceptors must be considered. Unlike common upconversion activators (Er^{3+}, Ho^{3+}, and Tm^{3+}), other lanthanides cannot be directly sensitized using Yb^{3+}. As in Tb^{3+} and Eu^{3+} activators without long-lived intermediate energy levels, energy transfer from Yb^{3+} to Tb^{3+} and Eu^{3+} is inefficient because of large energy gaps. Upconversion from these activators is possible through cooperative sensitization, but it requires high input power (Fig. 6A). This problem has been addressed by introducing energy migration in core-shell nanocrystals with significantly augmented emission intensity.[53,54] To achieve energy migration upconversion, sensitizers and activators must be spatially separated in the core and shell, respectively (Fig. 6B). In the core, Yb^{3+}/Tm^{3+} are codoped to populate Tm^{3+} activators to high-lying excited states upon NIR excitation. The critical factor triggering energy migration through the core-shell interface is selecting gadolinium (Gd) ions as the host lattice for the core and shell. After a five-photon pumping process, the energy of Tm^{3+} activators can be efficiently extracted by the Gd sublattice. Subsequently, the energy diffuses and migrates from the core to the shell layer and eventually to activators

(e.g., Tb^{3+}, Eu^{3+}, Dy^{3+}, and Sm^{3+}) doped in the shell(Fig. 6C). As such, activators without intermediate states can be efficiently sensitized by Yb^{3+}. Energy migration-mediated upconversion luminescence of Tb^{3+} and Eu^{3+} is much brighter than that of Dy^{3+} and Sm^{3+}. For this reason, Tb^{3+} and Eu^{3+} activators have been more extensively studied than Dy^{3+} and Sm^{3+} activators.

3.3 Blocking energy leakage

Surface quenching occurs when excited-state emitters are deactivated by contact with quenchers, such as defects, solvent molecules or surface ligands.[76,77] Nanocrystals have a high probability of surface luminescence quenching because of their high surface-to-volume ratios. Yb^{3+}/Tm^{3+}-codoped nanocrystals show significant enhancement in upconversion emission when particle sizes are increased (Fig. 7A). After coating an inert protection layer, smaller particles exhibit more prominent luminescence enhancement (Fig. 7B).

Energy migration upconversion can be further optimized by adding an inert layer to prevent energy loss through the Gd sublattice. In the absence of inert-layer protection, suppression of energy migration by surface defects and ligands is highly possible, hindering energy transfer to lanthanide activators (Fig. 8A). To enhance emission, the activator doping concentration needs to be

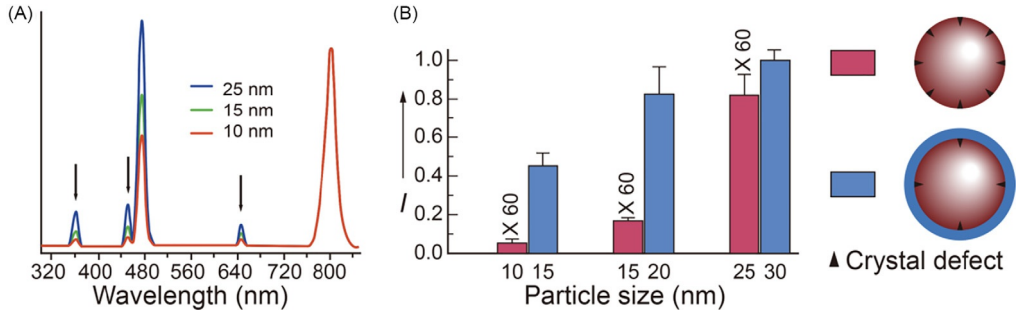

Fig. 7 (A) Upconversion emission spectra of $NaGdF_4$:Yb/Tm nanocrystals with different sizes upon 980 nm excitation. (B) Comparison of upconversion luminescence enhancement factors for nanocrystals with varied sizes after coating protecting layer. Printed with permission from Ref. Wang, F.; Wang, J.; Liu, X. *Angew. Chem. Int. Ed.* **2010**, *49*, 7456–7460. Copyright © 2010 WILEY-VCH Verlag GmbH & Co. KGaA, Weinheim.

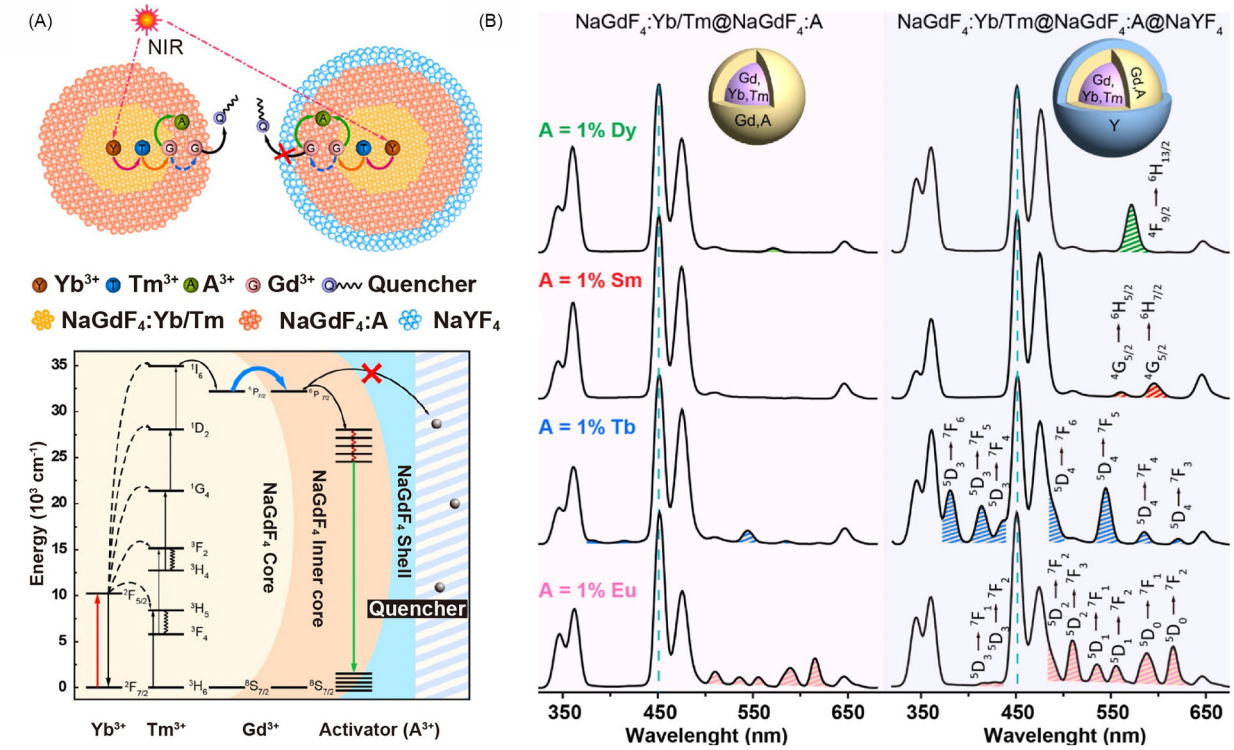

Fig. 8 (A) Schematic illustration of the protective effect of inert $NaYF_4$ layer for energy migration upconversion nanocrystals. (B) Spectra comparison between energy migration upconversion crystals with and without $NaYF_4$ inert layer protection. Printed with permission from xRef. Su, Q. et al. *J. Am. Chem. Soc.* **2012**, *134*, 20849–20857. Copyright © 2012 American Chemical Society.

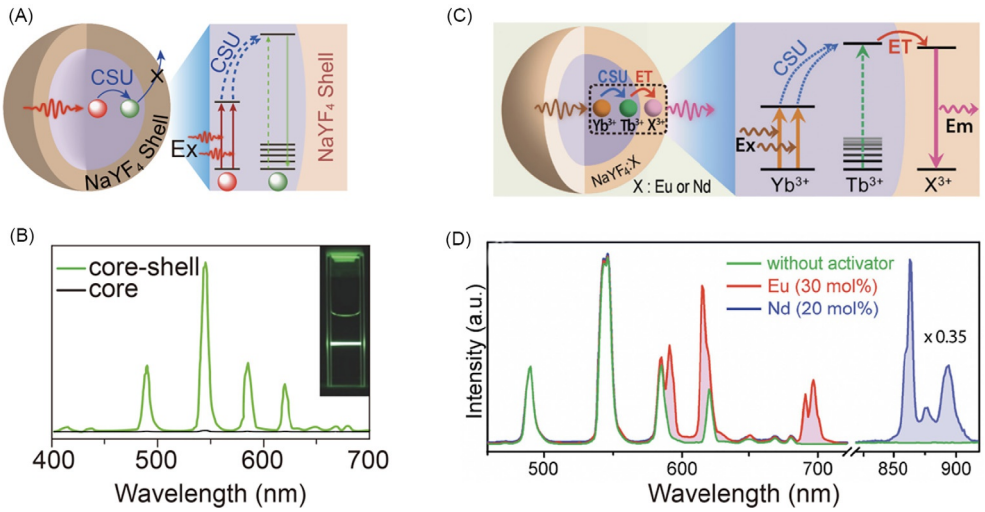

Fig. 9 (A) Schematic illustration of cooperative sensitization with inert shell protection. (B) Upconversion emission spectra of Yb/Tb-codoped upconversion nanocrystals with and without inert shell coating. (C) Cooperative sensitization upconversion-induced interfacial energy transfer mechanism. (D) Upconversion emission spectra of core-shell nanocrystals with different acceptors in the shell layer. Printed with permission from Ref. Zhou, B.; Yang, W.; Han, S.; Sun, Q.; Liu, X. *Adv. Mater.* **2015**, *27*, 6208–6212. Copyright © 2015 WILEY-VCH Verlag GmbH & Co. KGaA, Weinheim.

significantly increased. However, with a $NaYF_4$ inert layer, only 1 mol% of activators is required to achieve comparable luminescence intensity (Fig. 8B).

Further evidence that is underpinned by inert shell-dependent luminescence enhancement is cooperative sensitization upconversion. In the vein of multiphoton excited luminescence, cooperative sensitization upconversion requires an intense energy flux for excitation. Without inert shell protection, the excitation energy of Yb^{3+} sensitizers would severely dissipate through surface quenching.[52] With $NaYF_4$ layer protection, excitation energy can be confined in the core region, permitting intense emission through cooperative sensitization (Fig. 9A and B). As with energy migration upconversion, cooperative sensitization upconversion can also be linked to other activators doped in an adjacent layer (Fig. 9C and D). For instance, the emitting energy of Tb^{3+} activators can be transferred to Eu^{3+} and Nd^{3+} activators for additional emission spectral modification.

Inert shell protection prevents surface quenching of luminescence. A particular concentration of sensitizers in the inert layer may harvest more light and further enhance luminescence.[15,41] Upon activation with sensitizers, the inert layer works as an active layer for incident excitation harvesting (Fig. 10A). Although more sensitizer doping improves light-harvesting, an excessive concentration could exacerbate the situation of surface quenching. Thus, doping of sensitizers in the active shell must be carefully optimized.

It is important to note that the optimum doping concentration of sensitizers in the active shell can be quite different, especially when the activator/sensitizer in the core is slightly or highly doped (Fig. 10B). For slightly sensitized/activated core nanoparticles, once an active layer is coated, the protective effect from the coating remains dominant. Thus a certain concentration of activator ($\sim$20 mol%) can still be doped in the active shell for luminescence enhancement. On the contrary, the excitation energy in the highly doped core will be linked to surface quenchers by sensitizers doped in the active shell, resulting in luminescence attenuation. As proof in $NaErF_4$@$NaLuF_4$:Yb core-shell nanoparticles reported in the literature, the core section was activated with 100 mol% Er^{3+} ions that functioned as both sensitizers and activators (Fig. 10C and D). When Yb^{3+} sensitizers were added to the active shell, upconversion luminescence rapidly declined, although Yb^{3+} ions could harvest incident photons.[78]

4 Recent strategies for enhancing upconversion luminescence

Although lanthanide-doped upconversion nanocrystals have found broad applications in bioimaging, multiplexing sensing, anticounterfeiting, lasing, and optogenetics, their low conversion efficiency has remained a formidable challenge, especially at the single-particle level. In recent decades, innovative solutions have been developed to synthesize upconversion nanocrystals with much-improved upconversion brightness. By way of illustration, by exploiting the energy flux behavior in upconversion nanocrystals, factors such as light-harvesting capability, energy cross-talking, and surface quenching can be rationally balanced for developing efficient nanocrystals with targeted optical properties.

Surface passivation is the most frequently used approach for upconversion luminescence enhancement and can be applied to all types of lanthanide-doped phosphors at nanoscale.[79–81] As a result of high surface-to-volume ratios of luminescent nanocrystals, many dopant ions are trapped on the outermost layer of the nanocrystals, and their luminescence can be readily quenched by surface impurities, ligands, and solvent molecules through multiphonon relaxation. Since this topic has been exhaustively reviewed previously,[40,82] we only summarize two key points of this approach.

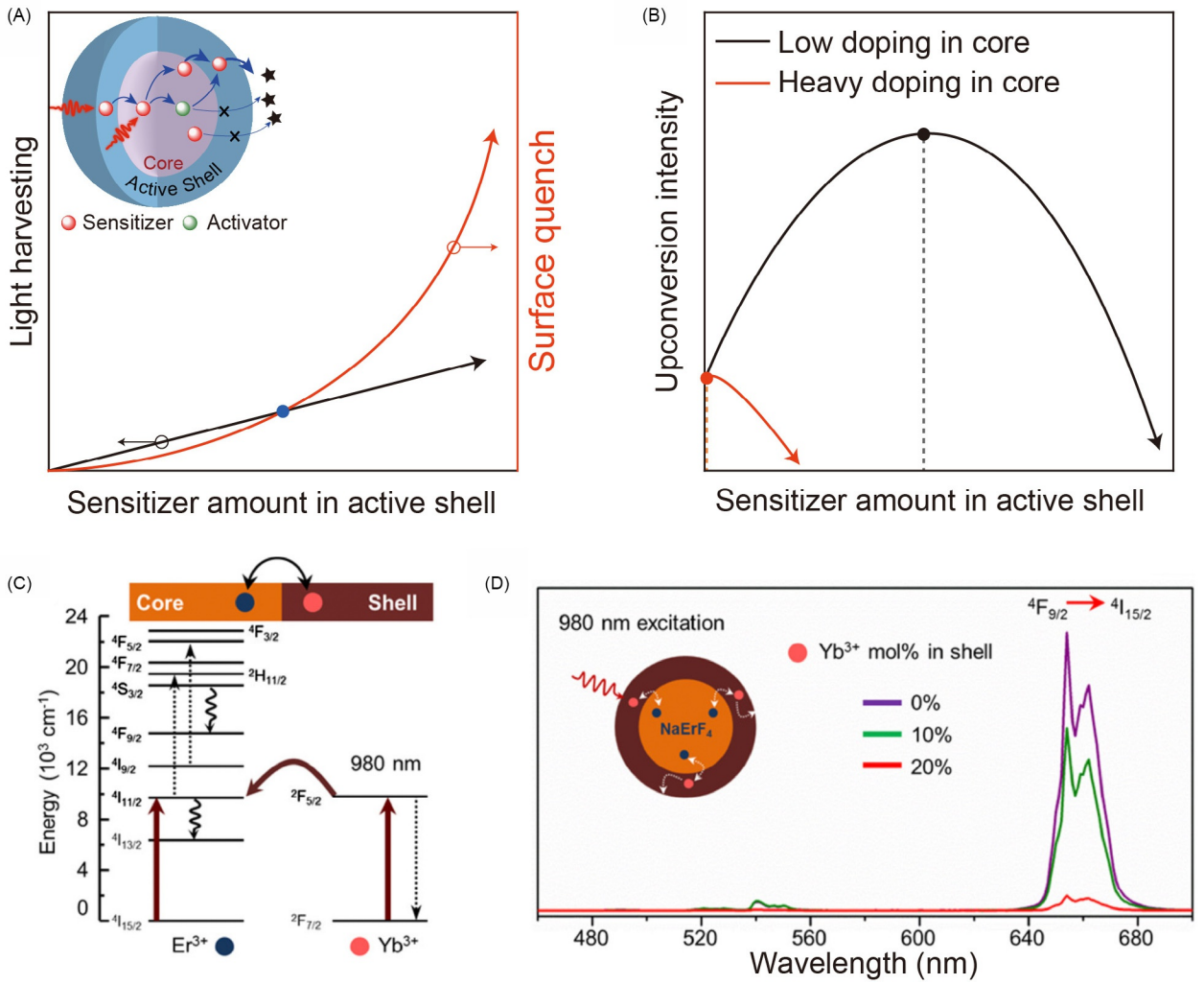

Fig. 10 (A) Balance between NIR-harvesting ability and surface quenching for sensitizers doped at different concentrations in the active shell. Inset shows the energy flow pathways in a core-active shell upconversion nanocrystal. (B) The optimum doping concentration of sensitizers in the active shell can be quite different for nanocrystals with low and high activator doping in the core. (C) Energy transfer mechanism of core-active shell nanocrystals sensitized by Yb^{3+}. (D) Upconversion luminescence spectra of $NaErF_4$@$NaLuF_4$:Yb nanocrystals with a different dopant concentration of Yb^{3+} in the active layer. (C, D) Printed with permission from Ref. Johnson, N. J. J. et al. *J. Am. Chem. Soc.* **2017,** *139*, 3275–3282.

i) Smaller upconversion nanocrystals benefit more from this approach. In particular, with a 2.5-nm $NaGdF_4$ shell, an emission enhancement factor of 450-fold has been reported for 10 nm $NaGdF_4$:YbTm nanocrystals. However, this value declines to 70-fold when the core size is around 25 nm. Therefore, for micrometer-sized upconversion crystals, the surface passivation approach will not work.

ii) Surface passivation is a prerequisite for bright upconversion emission with Yb^{3+} sensitization. This is because energy dissipation through the Yb^{3+} sensitizer sublattice to surface quenchers is responsible for surface quenching; For Nd^{3+}-sensitized upconversion nanocrystals, surface passivation would not lead to significant luminescence enhancement. This is because Nd^{3+} sensitizers do not form energy dissipation sublattices, which is quite different from Yb^{3+} sensitizers. However, it is important to note that surface passivation should still be applied when Yb^{3+} sensitizers coexist with Nd^{3+} sensitizers in the same spatial layer.

Besides optimization of upconversion nanocrystals, approaches involving external stimuli have been applied for luminescence enhancement. On account of intense light absorption and scattering of noble-metal nanoparticles, surface plasmon coupling has been widely used for optoelectronic controlling.[83–85] Upon illumination, free electrons of metal nanoparticles oscillate at frequencies similar to those of passing photons and subsequently enter localized surface plasmon resonance. Resonance peaks can be finely tuned from the visible to the NIR region by controlling morphology, chemical composition, and spatial design.[86,87] For upconversion luminescence enhancement, the surface plasmon can contribute in two ways (Fig. 11A): (i) Enhancing light absorption of lanthanide ions. In view of the nonlinear emission nature of lanthanide upconversion, a slight enhancement in excitation intensity can result in significant luminescence enhancement, especially for those emission transitions featuring 4- or even 5-photon processes. (ii) Improving radiative decay rates of activators. The small gap between adjacent energy levels of lanthanide activators

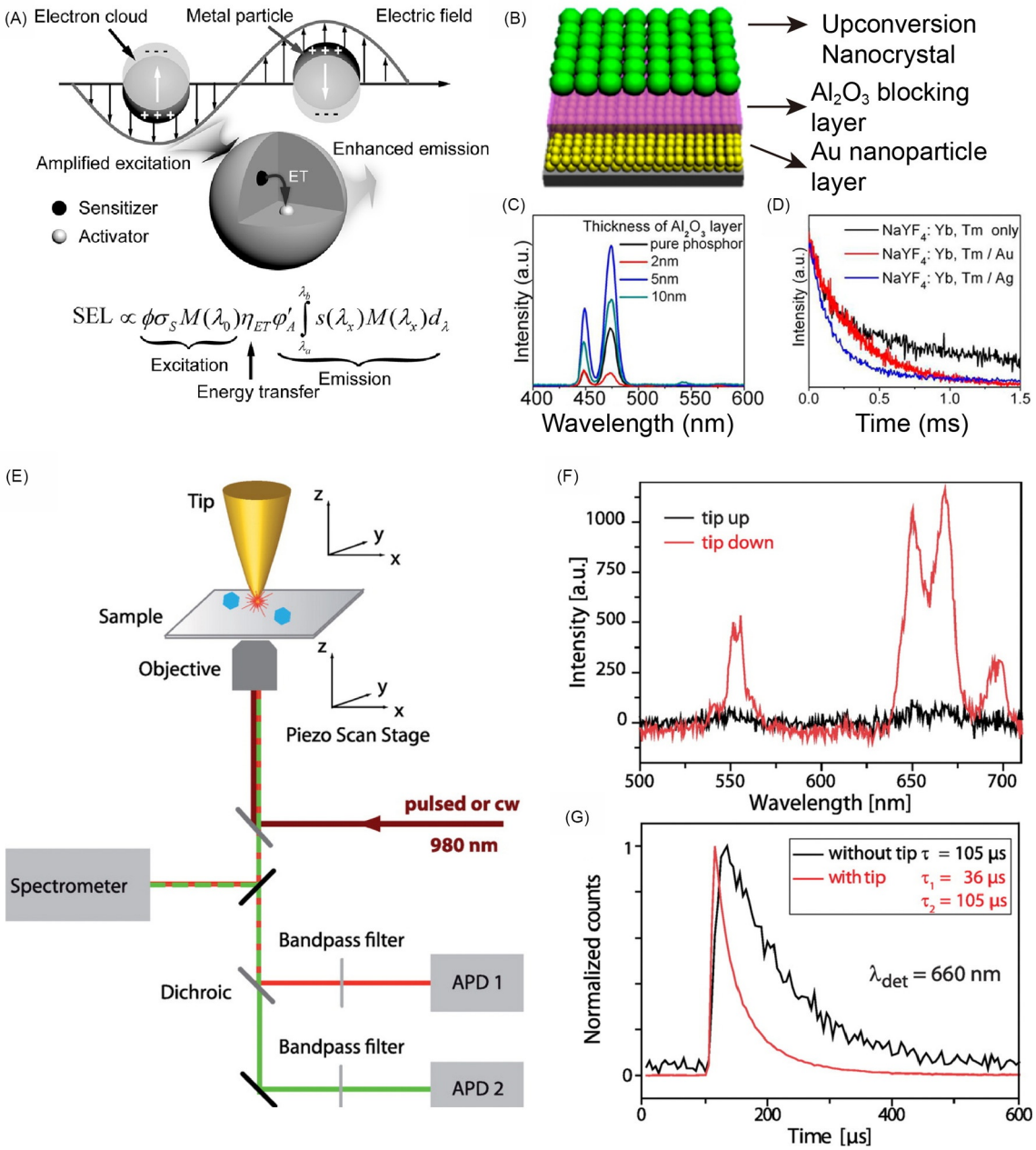

Fig. 11 (A) Schematic illustration of surface plasmon mediated upconversion luminescence enhancement. (B) Experimental design of Au nanoparticle surface plasmon assisted photon upconversion luminescence modulation. (C) Upconversion luminescence variation as a function of the thickness of the Al_2O_3 blocking layer. (D) Luminescence lifetime of $NaYF_4$: Yb/Tm nanocrystals with and without surface plasmon coupling. (E) Experimental design of noble metal tip-enhanced upconversion luminescence. (F) Upconversion luminescence of single Er^{3+} activated nanoparticle while tipping up and down. (G) Luminescence lifetime of Er^{3+} activators with and without tip attachment. (A) Printed with permission from Ref. Han, S.; Deng, R.; Xie, X.; Liu, X. *Angew. Chem. Int. Ed.* **2014**, *53*, 11702–11715. Copyright © 2014 WILEY-VCH Verlag GmbH & Co. KGaA, Weinheim. (B, C, D) Printed with permission from Ref. Saboktakin, M. et al. *ACS Nano* **2010**, *6*, 8758–8766. Copyright © 2012 American Chemical Society. (E, F, G) Printed with permission from Ref. Mauser, N. et al. *ACS Nano* **2015**, *9*, 3617–3626. Copyright © 2015 American Chemical Society.

induces nonradiative decay, which could significantly reduce the quantum yield of lanthanide luminescence. Improvement of radiative decay rates of activators can be a direct and effective way for lanthanide luminescence enhancement.

One important issue is that the distance between metal nanoparticles and upconversion nanocrystals should be carefully controlled for upconversion luminescence amplification.[88] For example, to study upconversion luminescence enhancement with surface plasmon coupling, an Al_2O_3 layer was used to block direct contact between the Au nanoparticle film and the upconversion nanocrystal monolayer (Fig. 11B). A threshold distance existed for luminescence enhancement. When the separation was inadequate, upconversion luminescence was quenched, and significant upconversion enhancement occurred once the separation

distance increased to 5 nm. The enhancement factor declined when reducing interactions between the Au nanoparticles and upconversion nanocrystals by increasing the separation distance (Fig. 11C). Lifetime variation was used to probe the occurrence of improved radiative decay rates. Results showed that the lifetime of upconversion luminescence from Tm^{3+} activators was shortened when coupled with plasmonic Au nanoparticles (Fig. 11D).

Single-particle level plasmon coupling-induced luminescence enhancement has also been achieved by researchers.[89] The distance between the gold nanotip and single upconversion nanoparticles can be finely controlled while collecting luminescence simultaneously (Fig. 11E). When the tip was proximal to the particle, emission was enhanced with a concomitant lifetime decline from 105 to 36 μs (Fig. 11F and G). Surface plasmon resonance of Au nanorods can be tuned to the NIR region by carefully adjusting their aspect ratios. With a considerable spectral overlap between Yb^{3+} sensitizer absorption and the resonance band of Au nanorods, excitation intensity can be indirectly enhanced (Fig. 12A). The distance between Au nanorods and lanthanide-doped nanocrystals can be controlled by the size of the silica sphere (Fig. 12B).[90] With spectral overlap, the pumped power density of 980-nm excitation near Au nanorod antennas was increased by local field enhancement (Fig. 12C), leading to a greater number of excited Yb^{3+} ions and thus enhanced upconversion luminescence (Fig. 12D).

Although surface plasmon coupling has long been applied to upconversion enhancement from less than one to over three orders of magnitude, practices such as nanoscale pattern/distance controlling are quite challenging.

Photonic-crystal engineering has also been employed for upconversion luminescence modulation.[91–96] Made from artificial periodic patterns of materials with different permittivities, light can be confined in photonic crystals with an enhanced density of states. The stop-band position of the photonic crystal structure can be rationally designed by tuning the size, structure, and refractive index of periodic units. Luminescence enhancement of lanthanide upconversion through photonic crystal engineering can be

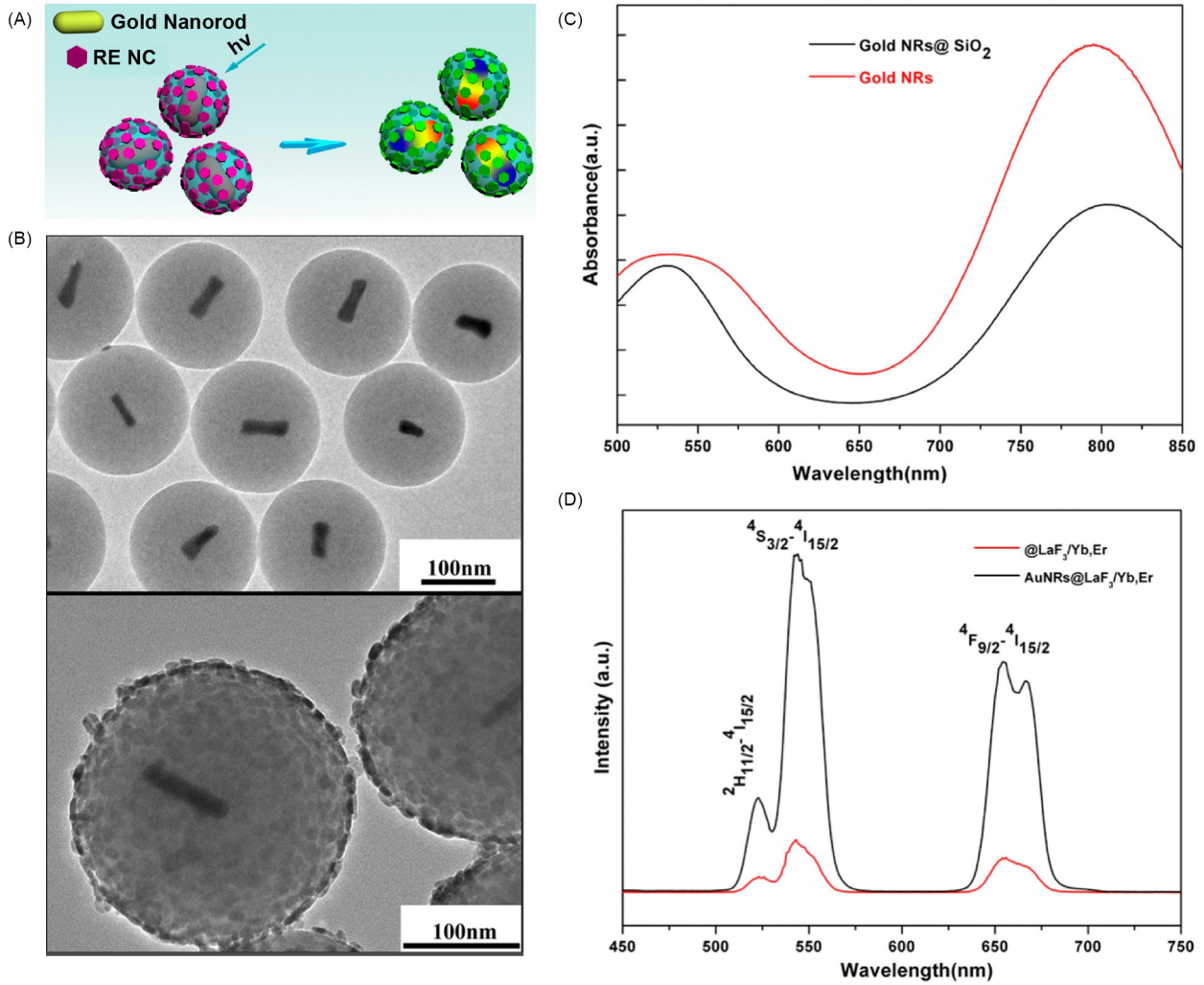

Fig. 12 (A) Schematic illustration gold nanorod induced lanthanide luminescence enhancement. (B) TEM image for Au nanorod@silica (top) and Au nanorod@silica@lanthanide emitter (bottom) nanostructures. (C) Surface plasmon resonance spectra of pure gold nanorods and nanorod@SiO_2 composite. (D) Upconversion emission spectra of Silica@LaF_3:Yb, Er nanocrystals with and without Au nanorod coupling. Printed with permission from Ref. Zhang, C.; Lee, J. Y. *J. Phys. Chem. C* **2013**, *117*, 15253–15259. Copyright © 2013 American Chemical Society.

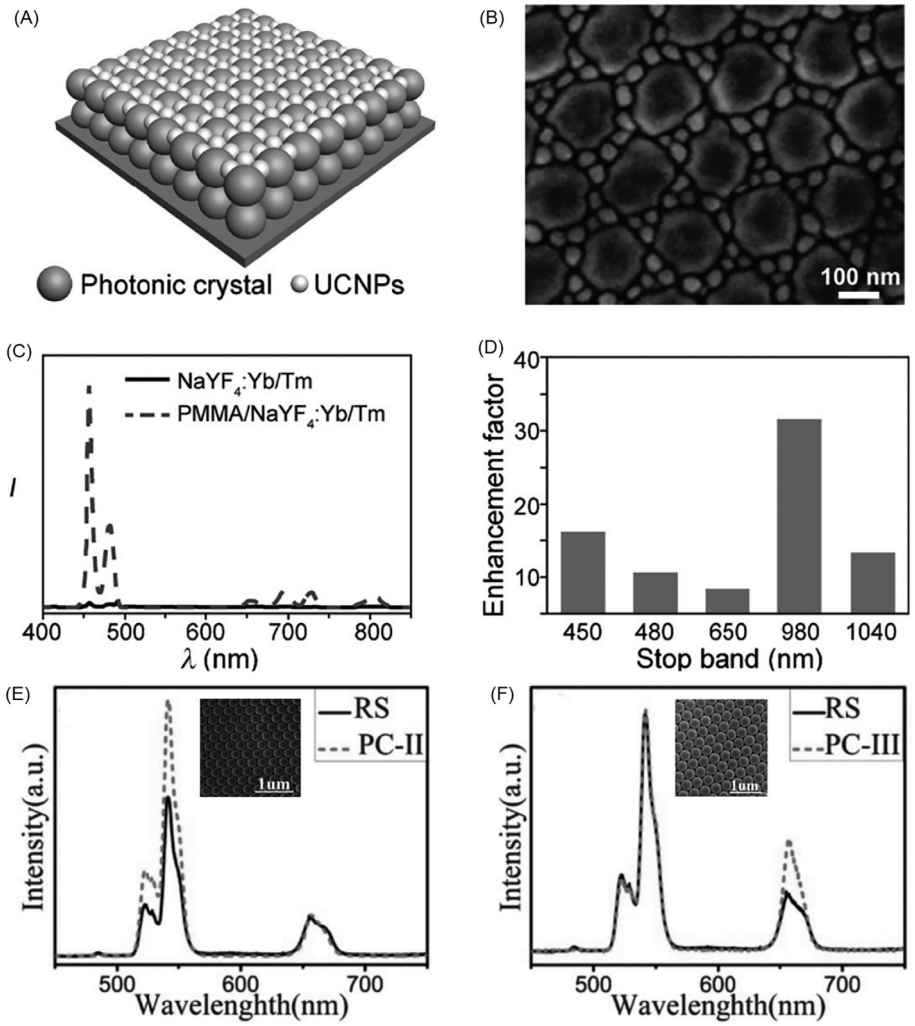

Fig. 13 (A) Experimental design for upconversion luminescence enhancement through photonic crystal coupling. (B) SEM image of the prepared sample with $NaYF_4$:Yb/Tm upconversion nanocrystals dispersed on the surface of PMMA structure. (C) Upconversion emission spectra with and without PMMA photonic crystal coupling. (D) Demonstration of the relationship between luminescence enhancement factors and the position of stopband of the prepared photonic crystal structure. (E, F) Upconversion luminescence of $NaYF_4$:Yb/Er with and without 275 nm (E) and 335 nm (F) polystyrene photonic crystal coupling. (B-D) Printed with permission from Ref. Yin, Z. et al. *Chem. Commun.* **2013**, *49*, 3781–3783. Copyright © 2013 Royal Society of Chemistry. (E, F) Printed with permission from Ref. Liao, J. et al. *J. Mater. Chem. C* **2013**, *1*, 6541–6546. Copyright © 2013 Royal Society of Chemistry.

attributed to two pathways: enhancing the electric field through resonance of excitation photons with photonic crystal modes and enhancing light collection by matching emission bands with stopbands.

As shown in Fig. 13, PMMA polymer beads can be used to fabricate 3D photonic crystals through self-assembly.[97] By depositing upconversion nanocrystals on the surface of PMMA photonic crystal structures, luminescence can be effectively augmented (~ 30-fold) once the stopband is tuned to overlap with the excitation (Fig. 13C). It should be noted that about 15-fold enhancement in blue emission can be achieved when the stopband is designed to 450 nm (Fig. 13D). This enhancement is attributed to photonic crystal reflection since blue emission largely overlaps with the stop band where photons are strongly reflected. For example, by coupling with photonic crystals fabricated using polystyrene (PS) beads,[98] upconversion emission bands (green and red) of $NaYF_4$:Yb/Er nanocrystals were selectively enhanced by changing the size of PS beads (Fig. 13E and F).

Besides the common enhancement strategies discussed above, several new techniques have emerged in the past 5 years. Here, we highlight recently developed strategies for boosting luminescence, including organic dye sensitization, plasmon nanocavity coupling, and dielectric superlens modulation.

4.1 Organic dye sensitization

Despite achievements in controlling the composition, size, shape and optical properties of upconversion nanocrystals, their weak and narrow-band NIR absorption remain a major challenge. This is because low-rate 4f-4f electronic transitions fundamentally

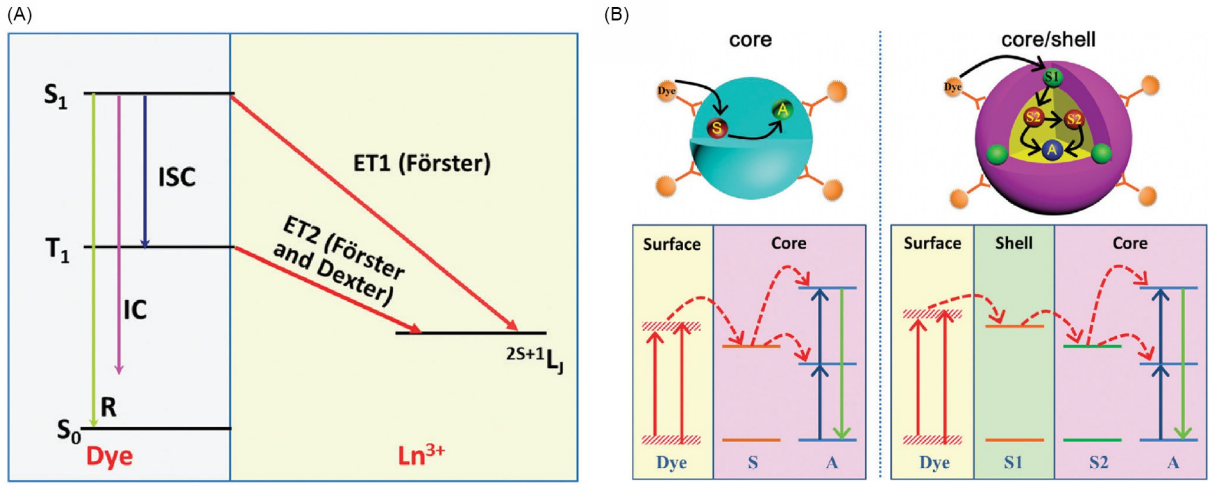

Fig. 14 (A) Schematic illustration of nonradiative energy transfer processes from organic dye to lanthanide ions. R, IC, and ISC represent the radiative emission, internal conversion, and intersystem crossing, respectively. (B) Commonly designed organic dye-sensitized upconversion. Printed with permission from Ref. Wang, X. et al. *Chem. Soc. Rev.* **2017**, *46*, 4150–4167. Copyright © 2017 Royal Society of Chemistry.

limited the absorption of doped lanthanide sensitizers. Recently, organic dyes have been utilized as antennas to enhance upconversion emission brightness. Because of the large absorption cross-sections ($\sim 10^{-16}$ cm^2) of organic dyes, which are several orders of magnitude larger than that of lanthanide ions (10^{-20}–10^{-19} cm^2), dye sensitization can significantly enhance the light-harvesting capacity of upconversion nanocrystals. Through efficient energy transfer from surface attached dye to lanthanide ions, upconversion luminescence can be remarkably promoted. The energy transfer mechanism from dye antenna to lanthanide ions is illustrated in Fig. 14A. Upon NIR excitation, the dye molecule can be excited from its ground singlet state (S_0) to excited singlet state (S_1). The excited dye can depopulate through two pathways to its ground state: (i) relaxation from S_1 to S_0 and (ii) S_1 relaxes to a triplet state (T_1) through fast inter-system crossing (ISC) and then depopulates to S_0. Both the S_1 and T_1 states can be depopulated through energy transfer to adjacent lanthanide ions.

Dye-sensitized upconversion is typically realized with two antenna-nanocrystal configurations (Fig. 14B): core-only or core-shell nanocrystals. For the first configuration, organic dye antennas work with Yb^{3+} sensitizers through direct energy transfer from the dye to Yb^{3+} ions. Then the excitation energy is delivered to upconversion activators (such as Er^{3+}, Tm^{3+}, and Ho^{3+}). Although this design is rather simple, both sensitizers and activators are exposed to surrounding luminescence quenchers. Although significant upconversion luminescence can be achieved, overall brightness remains low due to persistent surface quenching. Dye-sensitized core-shell structures are much more rational for upconversion enhancement. In this design, Nd^{3+} sensitizers are usually selected for co-sensitization with Yb^{3+} sensitizers.[59,99] Under NIR excitation, excited dye antennas transfer energy to Nd^{3+} sensitizers in the shell layer. Then the energy can be passed to Yb^{3+} sensitizers, and subsequently, energy transfer upconversion occurs. Unlike the core-only design, the core-shell design enables much brighter emission due to surface passivation of the Nd^{3+} sensitization layer.

In 2012, pioneering work in enhancing upconversion luminescence was published by coupling nanocrystals with organic dye molecules (Fig. 15A).[64] Through nucleophilic substitution, a carboxylic acid-functionalized derivative IR-806 dye was synthesized based on a commercial cyanine dye, IR-780. With the carboxylic group, the IR-806 dye can be attached to the surface of $NaYF_4$:Yb/Er nanocrystals. Due to the considerable overlap between the emission spectrum of IR-806 dye and the absorption spectrum of Yb^{3+} sensitizers, efficient energy transfer from IR-806 to Yb^{3+} ions occurs once dye antennas are stimulated (Fig. 15B). Experimental results showed that the extinction coefficient of IR-806 was about six orders of magnitude higher than that of prepared nanocrystals. As a result, upon 800-nm excitation, NIR-806 dye-sensitized nanocrystals are more than 1100 times brighter than nanocrystals without sensitization upon 980-nm excitation (Fig. 15C). More importantly, as shown in Fig. 15D, by virtue of the broadband absorption of organic dyes, IR-806-sensitized nanocrystals can be enlightened using excitation photons with wavelengths from 720 to 830 nm.

To eliminate surface quenching of dye-sensitized core-only nanocrystals, core-shell structures can be introduced for energy cascade upconversion.[100] To illustrate, the core particle codoped with Yb^{3+}/Tm^{3+} ions is protected by a shell with Nd^{3+} sensitization, and the core-shell structure is further sensitized by NIR dye antennas attached to nanoparticle surfaces (Fig. 16A). Under NIR excitation, energy from excited dye molecules is transferred to adjacent Nd^{3+} sensitizers in the shell layer. Afterward, efficient energy transfer from Nd^{3+} to Yb^{3+} sensitizers occurs, followed by energy transfer to Tm^{3+} activators. Unlike lanthanide ions, organic dyes feature broad absorption and emission bands, ensuring broadband excitation and sufficient spectral overlap. For Nd^{3+}/Yb^{3+} sensitized upconversion nanocrystals, multiple narrow excitation bands can be detected (740 nm, 800 nm, and 980 nm). However, once sensitized by the organic dye, the excitation band can be significantly broadened and enhanced (Fig. 16B). The strong enhancement in blue emission is clearly shown from inserted images. The excitation band can be further broadened since Nd^{3+} sensitization with multiple IR dyes is plausible. As shown in Fig. 16C, intense excitation bands were detected for core-shell

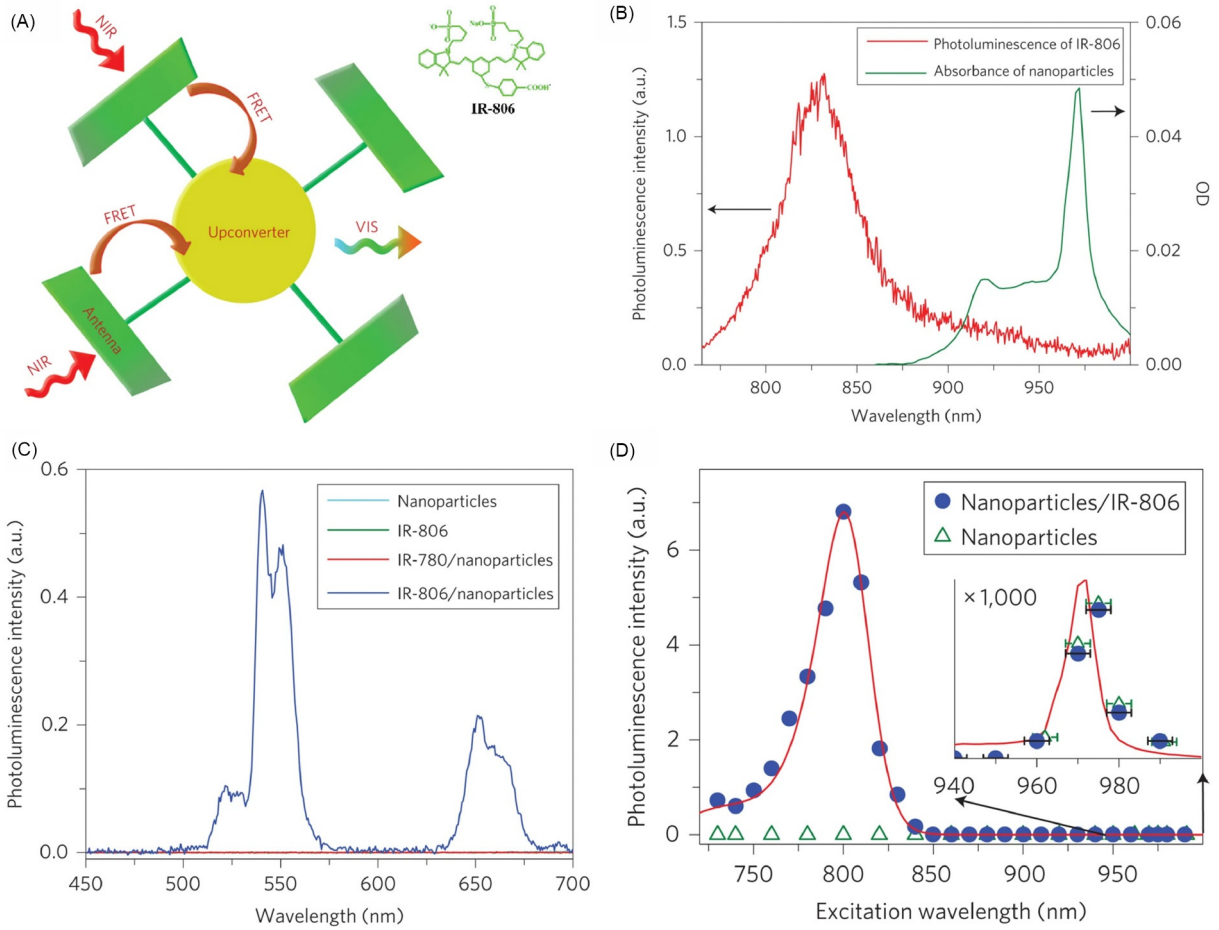

Fig. 15 (A) Principal concept of dye-sensitized upconversion. (B) The absorbance of Yb^{3+} sensitized upconversion nanocrystals and photoluminescence of IR-806 dye. (C) Upconversion luminescence spectra of $NaYF_4$:Yb/Er nanocrystals with different IR dye sensitization excited by a 2 mW continuous-wave laser. (D) Experimental upconversion excitation spectra of β-$NaYF_4$:Yb/Er nanoparticles/IR-806 (blue circles) and β-$NaYF_4$:Yb, Er nanoparticles (green triangles), both dissolved in $CHCl_3$. Printed with permission from Ref. Zou, W.; Visser, C.; Maduro, J. A.; Pshenichnikov, M. S.; Hummelen, J. C. *Nat. Photon.* **2012**, *6*, 560–564. Copyright © 2012, Nature Publishing Group.

nanocrystals sensitized with IR-806 and IR-808. However, for IR 820, sensitization efficiency is relatively low, which can be ascribed to the smaller spectral overlap between the emission band of the IR dye and the Nd^{3+} absorption spectrum. However, compared with dye-sensitized core-only nanocrystals, Nd^{3+}-sensitized core-shell nanocrystals allow more freedom in IR dye selection. As demonstrated in Fig. 16D, strong blue emission from Tm^{3+}-activated core/shell nanocrystals can be triggered by multiple excitation bands centered at 740 nm, 780 nm, 800 nm, 810 nm, 830 nm, and 850 nm. Thus, in contrast to pure nanocrystals that usually require laser excitation, dye-sensitization endows upconversion nanocrystals with the capacity to emit intense luminescence with incoherent broadband excitation. As demonstrated in the bottom panel of Fig. 16D, the pattern with blue upconversion luminescence can be distinguished upon incoherent light excitation.

The dye-sensitized core-shell configuration can be further optimized. Although exposure of Yb^{3+} sensitizers can lead to severe surface quenching, low-content co-doping of Yb^{3+} ions in the active shell eventually enhances the overall upconversion output. Despite efficient interfacial energy transfer from Nd^{3+} to Yb^{3+}, their spatial isolation in core and shell layers leads to inefficient excitation energy extraction. Furthermore, unlike Yb^{3+} sensitizers in which sublattice energy can migrate long distances, inter-sensitizer energy transfer for Nd^{3+} ions is extremely inefficient. Thus, introducing Yb^{3+} sensitizers with Nd^{3+} sensitizers in the same spatial layer facilitates energy extraction efficiency from the shell to the core, where activators exist.[101] As can be seen in Fig. 17A, multiple energy transfer pathways are simultaneously involved in relaying energy from IR dye antennas to activators in the core. Apart from direct energy transfer from IR dyes to Nd^{3+} activators, Yb^{3+} sensitizers can be activated by accepting energy from dye molecules without the help of Nd^{3+} sensitizers (Fig. 17B). As shown in Fig. 17C, compared to configurations based on dye-Nd and dye-Yb, the dye-Nd/Yb design shows much-improved excitation efficiency from 700 to 850 nm. Importantly, these IR dye-sensitized upconversion nanocrystals can be well dispersed in a polymer matrix for potential applications in display. As shown in Fig. 17D, dye-sensitized core/shell upconversion nanocrystals activated with different activators (Er^{3+}, Ho^{3+}, Tm^{3+}) can be integrated into PDMS film for multicolor emission demonstration.

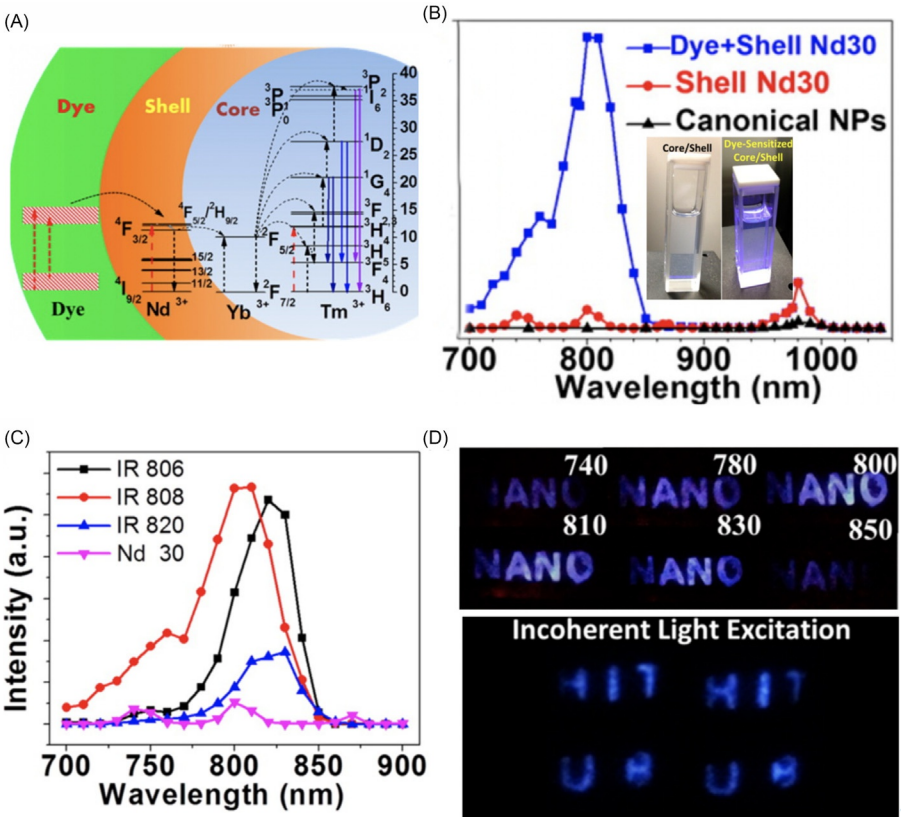

Fig. 16 (A) Scheme of the proposed nanostructure and energy transfer pathway for energy-cascaded upconversion in dye-sensitized fluoride core/shell nanocrystals. (B) Excitation spectra (for: IR-808 dye-sensitized ($NaYbF_4$:Tm^{3+} 0.5%)@$NaYF_4$:Nd^{3+} 30% (blue), ($NaYbF_4$:Tm^{3+} 0.5%)@$NaYF_4$:Nd^{3+} 30% (red), and canonical ($NaYF_4$:Yb^{3+} 30%, Tm^{3+} 0.5%)/$NaYF_4$ core/shell UCNPs (black). (C) Excitation spectra of upconversion nanocrystals sensitized with different NIR dyes. (D) Photographic image for dye-sensitized upconversion nanocrystals upon different wavelength excitation. Printed with permission from Ref. Chen, G. et al. *Nano Lett.* **2015**, *15*, 7400–7407. Copyright © 2015 American Chemical Society.

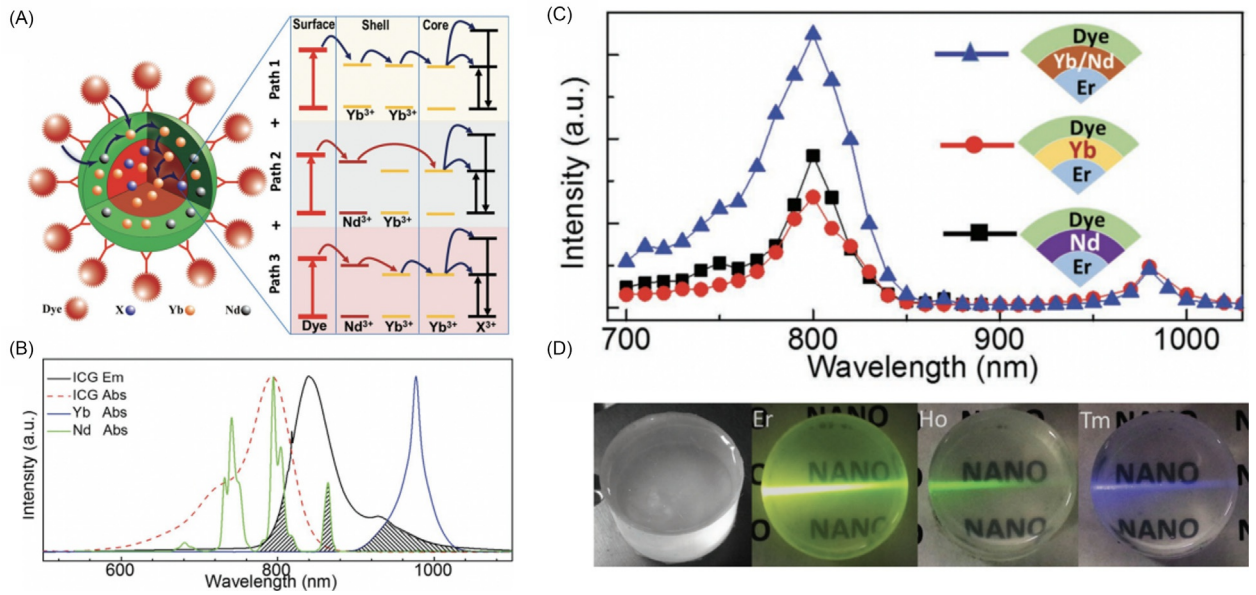

Fig. 17 (A) Schematic illustration of multidimensional energy transfer pathways from the dye molecules on the surface of the core/active shell nanocrystal of ($NaYF_4$:Yb/X)@$NaYF_4$:Nd/Yb to the lanthanide ions in the core. (B) Absorption and emission spectra of ICG dye versus the absorption spectra of Nd^{3+} ions and Yb^{3+} ions. (C) Excitation spectra of upconversion nanocrystals with different energy transfer pathways. (D) Photographic images of a transparent polydimethylsiloxane (PDMS) cylinder doped with ICG-sensitized core/active shell nanocrystals. Printed with permission from Ref. Chen, G. et al. *Adv. Opt. Mater.* **2016**, *4*, 1760–1766. Copyright © 2016 WILEY-VCH Verlag GmbH & Co. KGaA, Weinheim.

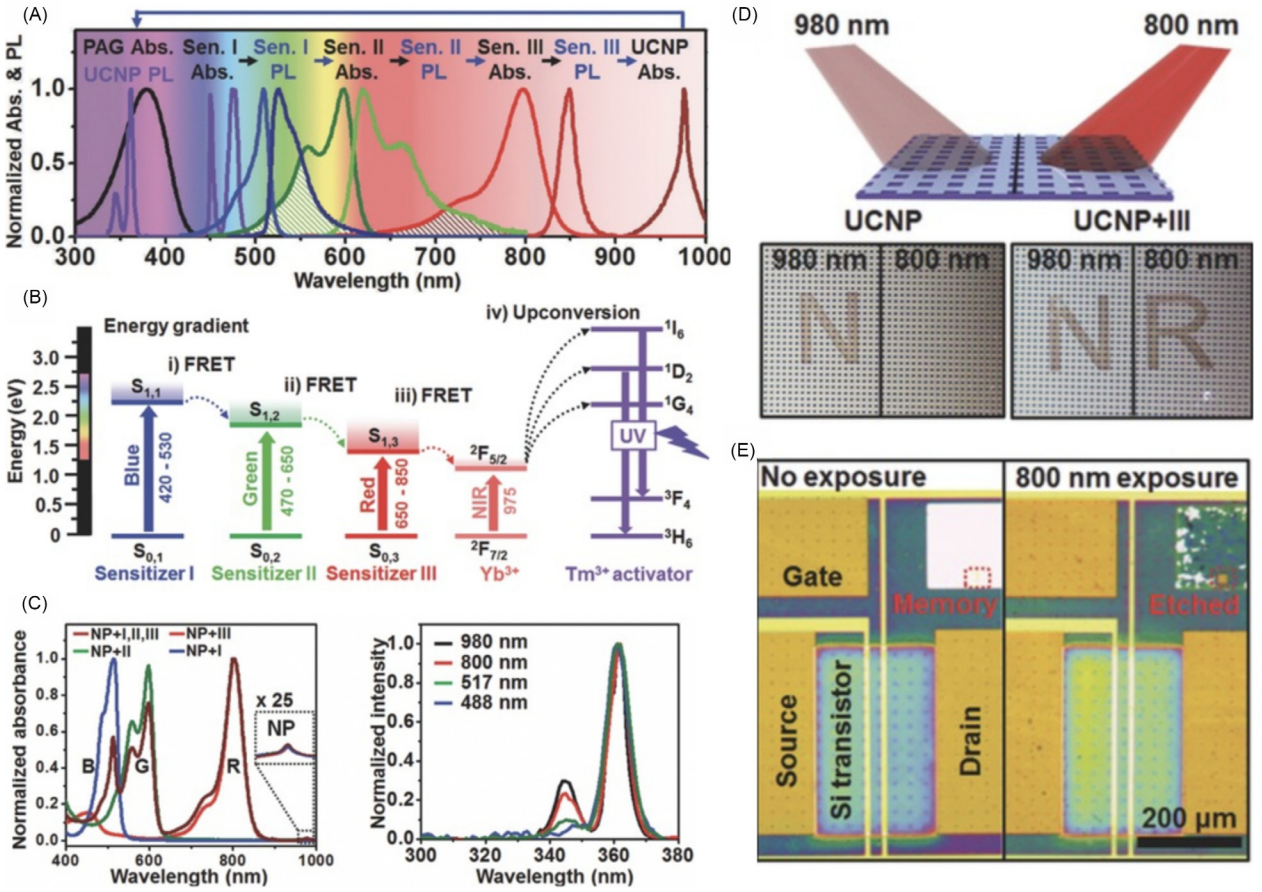

Fig. 18 (A) Normalized absorption/emission spectra of dye molecules used for upconversion sensitization. (B) Cascaded energy transfer between surface-modified dye molecules for upconversion sensitization. (C) Absorption spectra of upconversion nanoparticles with dye sensitization and emission spectra of nanocrystals upon different excitation sources. (D) Images of the etched Mg layer coated with upconversion nanocrystals (left) and nanoparticle/sensitizer III (right) by exposure to 980 and 800 nm laser with the same power density of 25 mW mm^{-2}. (E) Magnified view of the integrated device without (left) and with light exposure (right) for photo-induced chemical destruction. Printed with permission from Ref. Lee, J. et al. *Adv. Mater.* **2017**, *29*, 1603169. Copyright © 2016 WILEY-VCH Verlag GmbH & Co. KGaA, Weinheim.

In principle, upconversion nanocrystals are sensitized with one type of IR dye antenna to achieve broadband sensitization. In 2016, a UV emitting dye-sensitized upconversion nanostructure harvesting photons of a wide wavelength range from 450 to 975 nm was reported. To achieve this, multiple dye molecules were modified on the surface of Yb^{3+}/Tm^{3+} codoped upconversion nanocrystals.[102] As illustrated in Fig. 18A, three types of Vis/IR dye antennas were selected for sensitization. Sensitizer III (IR antenna) can directly transfer its energy to Yb^{3+} sensitizers for energy transfer upconversion. More importantly, the absorption spectra of sensitizers I and II covered the range from 450 to 650 nm, and their energy was eventually transferred to Yb^{3+} sensitizers because of a suitable energy gradient (Fig. 18B). Therefore, intense UV emission (340–370 nm) was obtained upon broadband excitation from 450 to 1000 nm (Fig. 18C). Multi-dye-sensitized UV emitting nanocrystals were integrated with resistive switching random access memory (RRAM) to develop a memory system featuring the novel function of unrecoverable data erasure. UV emission from upconversion nanocrystals triggered chemical destruction of the ultrathin RRAM. As demonstrated in Fig. 18D, for pure nanocrystals coated RRAM, 980 nm laser exposure induced chemical destruction patterns, however, the film showed no response to 800-nm excitation. In contrast, both 980 and 800 nm illumination resulted in RRAM destruction when sensitizer III-sensitized upconversion nanocrystals were used. Moreover, 800-nm exposure can store data in the memory array with a power density of 25 mW mm^{-2} (Fig. 18E).

We should note that all of the above-mentioned dye-sensitized nanocrystals are designed based on the spectral overlap between the dye singlet luminescence (S_1 to S_0 transition) and the sensitizer absorption. In 2018, it was shown that an increase in lanthanide doping content shifts the primary energy donor from the dye singlet to its triplet, and resultant triplet states then mediate energy transfer to nanocrystals, resulting in significant luminescence enhancement.[103] Fig. 19A shows an IR-806 dye antenna bound to a $NaYGdF_4$:Yb/Er nanocrystal. Photon upconversion occurs inside the nanoparticle where two Yb sensitizers excite an Er activator into a higher energetic state. Upon 808-nm excitation, the IR-806 antenna is excited to its first singlet state. By increasing the doping concentration of Gd^{3+} in the host lattice, singlet-to-triplet intersystem crossing can be significantly enhanced because of heavy atom effects induced by Gd^{3+}. Compared to luminescence from pure nanoparticles ($l_{ex} = 980$ nm), IR-806-sensitized $NaYF_4$:Yb/Er

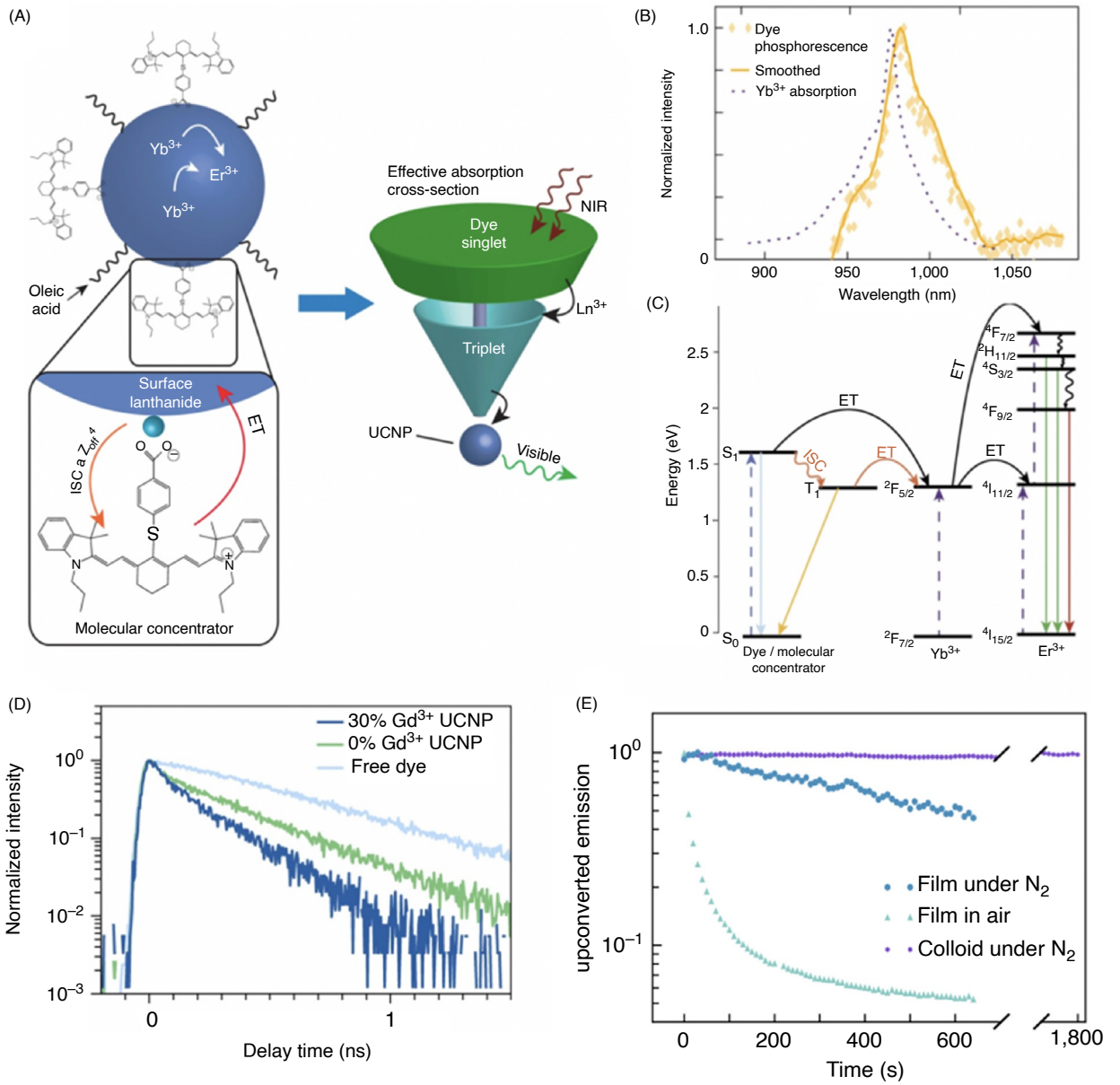

Fig. 19 (A) Cartoon schematic of the dye-sensitized upconversion nanocrystal system, showing IR-806 bound to the crystal surface, and an upconversion event inside the nanoparticle. (B) Phosphorescence of NIR-806 dye and absorption spectrum of Yb^{3+} sensitizers. (C) Energy transfer scheme for dye-sensitized photon upconversion. (D) Luminescence lifetime variation for NIR-dye before and after attached to nanocrystal surfaces with and without Gd^{3+} doping. (E) Upconversion luminescence intensity versus exposure time under different atmospheric conditions. Printed with permission from Ref. Garfield, D. J. et al. *Nat. Photon.* **2018**, *12*, 402–407. Copyright © 2018, Nature publication group.

nanocrystals showed approximately 500-fold enhancement in upconversion emission under 808-nm excitation. This enhancement factor was further increased to 15,000-fold with 30% Gd^{3+} dopants. The red-shift of phosphorescence relative to fluorescence from the IR-806 antenna was considered the main reason for enhanced emission. With the Gd^{3+} co-doping, the excited IR-806 antenna quickly populates to the triplet state to generate phosphorescence, which has a much larger spectral overlap compared to that between the singlet stemmed fluorescence and the Yb^{3+} absorption spectrum, thus significantly enhancing energy transfer from Yb^{3+} sensitizers to dye antennas (Fig. 19B and C). The efficient energy transfer from the dye to lanthanide sensitizers is signified by the fluorescence lifetime variation of IR-806 antennas. As can be seen in Fig. 19D, attaching a dye antenna to nanocrystal surfaces shortens their fluorescence lifetimes to some extent; however, adding Gd^{3+} ions to the host lattice can amplify this phenomenon, indicating that more efficient energy transfer can be triggered once Gd^{3+} ions are introduced. Although heavy-atom-induced triplet enhancement improves emission brightness, this strategy is only appliable under inert gas conditions. Because dissolved singlet oxygen molecules severely depopulate triplet states of dye antennas and block energy transfer to lanthanide sensitizers, elimination

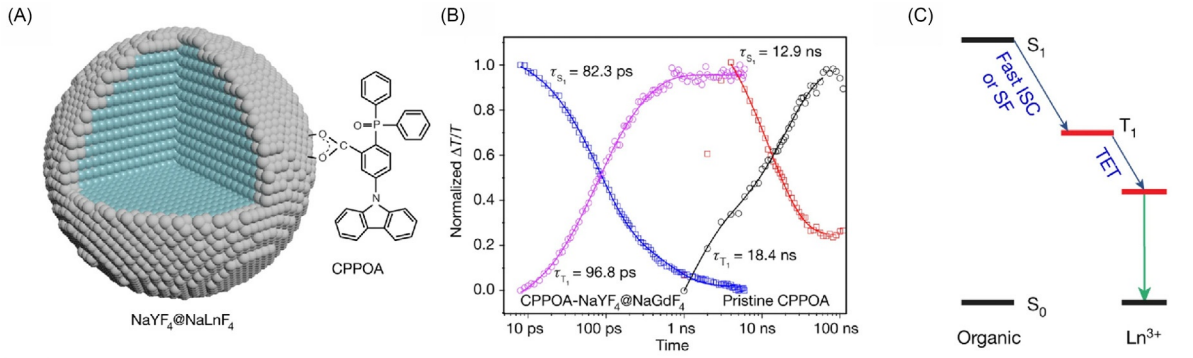

(D)

Elements	Y	Eu	Gd	Tb	Yb	Lu	CPPOA
Atomic number	39	63	64	65	70	71	
Number of 4f electrons	0	6	7	8	13	14	
Number of unpaired electrons	0	6	7	6	1	0	
Triplet generation time of CPPOA (ps)	17400	9.3	96.8	92.4	2200	12300	18400

Fig. 20 (A) Schematic illustration of a $NaYF_4$@$NaLnF_4$ core-shell nanoparticle modified with CPPOA. (B) Extracted kinetics showing the singlet (S_1) decay and triplet (T_1) growth of a solution containing pristine CPPOA molecules and of a solution of CPPOA-modified $NaYF_4$@$NaGdF_4$ nanoparticles. (C) The interaction between the lanthanides and the molecules accelerates the ISC from the singlet to triplet exciton states of the molecule. (D) Triplet state generation speed of CPPOA molecules attached on nanocrystals with different lanthanide ion doping. Printed with permission from Ref. Han, S. et al. *Nature* **2020**, *587*, 594–599. Copyright © 2020, Nature publication group.

of moisture and oxygen is a prerequisite for applying this approach for upconversion enhancement. As shown in Fig. 19E, upconversion luminescence of dye-sensitized nanocrystals decays rapidly in air, but their stability can be significantly improved with nitrogen protection.

A recent study published in Nature suggested that the above-mentioned heavy-atom effect is not the exact reason for enhanced upconversion luminescence (Fig. 20).[66] To prove the heavy atom effect for triplet-state accumulation, other lanthanide ions with comparable atomic numbers, such as Lu^{3+} and La^{3+}, should be employed to investigate luminescence enhancement. However, previous research concluded, using only Gd^{3+} as an example, that the heavy atom effect is the main factor governing luminescence enhancement. Systematically, in the Nature study, researchers found that only lanthanide ions with unpaired electrons can facilitate intersystem crossing from the excited singlet state to a triplet state. For example, compared to pristine 9-[3-carboxyl-4-(diphenylphosphinoyl)phenyl]-9H-carbazole (CPPOA) molecules, the triplet state rise rate of those molecules attached to $NaYF_4$@$NaGdF_4$ nanocrystal surfaces is almost three orders of magnitude faster (Fig. 20B and C). As with Gd^{3+}-doped nanocrystals, those doped with lanthanide ions containing unpaired electrons (e.g., Eu^{3+}, Tb^{3+}, and Yb^{3+}) could remarkably shorten the triplet state generation of attached dye antennae (Fig. 20D). In contrast, for Lu^{3+} doping, the triplet state generation rate could not be facilitated, although the atomic number of Lu^{3+} is much larger than that of Gd^{3+}. Thus, with fast intersystem crossing, dye sensitizers could be quickly populated to their triplet states, which may promote efficient energy transfer from dyes to lanthanide sensitizers, which should explain the significant upconversion enhancement, instead of the heavy-atom effect.

Dye-sensitization has proven effective for luminescence enhancement; however, this strategy has not found many practical applications. One reason is that even though upconversion nanocrystals have high photostability, the stability of attached organic dyes is extremely low. Moreover, with dye sensitization, further surface modifications for specific bio-applications are rather challenging. In addition, for triplet exciton-mediated sensitization, inert gas protection is required, which makes practical applications difficult.

4.2 Nanocavity-assisted surface plasmon coupling

There have been many reports on plasmon-enhanced upconversion luminescence in solution and on lithographically prepared substrates. However, precise control of orientation and distance of the plasmonic nanoparticles with respect to the upconversion nanocrystals is quite difficult. Lithographic fabrication of nanostructures allows better control of the morphology of plasmonic structures and the distance between the plasmonic structures and upconversion nanocrystals. In 2018, a paper reported over a 1000-fold emission enhancement of $NaYF_4$:Yb/Er nanocrystals by incorporating them in a metal-insulator-metal (MIM) structure (Fig. 21).[104] The fabrication procedure of the MIM structure is illustrated in Fig. 21A. Through a few relatively simple steps without complicated wet-chemistry techniques, the lithographic fabrication method is readily scalable to large areas for higher yield while maintaining excellent uniformity. For the fabricated MIM structure, gold is used as top and bottom metal layers and a monolayer of $NaYF_4$:Yb/Er nanocrystals works as the insulator layer (Fig. 21B–D). Electric field simulation of the MIM structure upon incident plane wave excitation shows that the plasmon mode exhibits strong field enhancement in the insulator layer, significantly enhancing the excitation intensity (Fig. 21B). With the finite-difference time-domain (FDTD) method, the resonance peak of prepared MIM can be tuned to around 980 nm, corresponding to the absorption transition energy of Yb^{3+} sensitizers. Fig. 21E shows the simulated diameter (D) dependence of plasmonic resonance. As the diameter is increased from 160 to 280 nm, the resonance peak shifts from 800 to 1200 nm. Importantly, for plasmonic structures with 220-nm D, the insulator layer shows the strongest absorption enhancement at 980 nm (Fig. 21F). For practical testing, MIM structures with diameters from 220 to 300 nm were fabricated and their luminescence spectra were measured (Fig. 21G). The green upconversion luminescence of all MIM samples showed significant enhancement compared to the control sample. Besides, the maximum enhancement occurs at a diameter of around 240 nm, which matches the simulation results well. More importantly, the MIM structure performs quite differently upon varied excitation power density (Fig. 21H). Upon low-power excitation ($<0.02\ kW\ cm^{-2}$), an enhancement factor of $\sim$1200-fold can be achieved, which declines with increased excitation power. Only a 200-fold enhancement was obtained at $100\ kW\ cm^{-2}$ power density. This is because upconversion luminescence saturates under high power excitation. Thus, with increased external excitation power, upconversion luminescence from a MIM structure and the reference finally approach each other.

For this work, the MIM-induced enhancement in upconversion luminescence can be attributed to the spectral overlap between the MIM plasmonic resonance and the Yb^{3+} absorption. In other words, the excitation power density surrounding upconversion nanocrystals is significantly enhanced.

Besides increasing the excitation power density by tuning the resonance peak to match sensitizer absorption, the spectral overlap between upconversion emission and resonance bands can be another practical approach for enhancing luminescence. For upconversion luminescence, quantum yield is usually ultra-low because it is limited by intense nonradiative relaxation of excited lanthanide activators. Thus, strategies that reduce nonradiative or increase radiative processes can directly enhance the quantum yield and ultimately the upconversion output.

By harnessing the Purcell effect, the radiative decay of lanthanide activators in the resonance cavity can be remarkably accelerated, resulting in a large increase in luminescence. This approach has been successfully applied to augment the fluorescence of organic dyes, quantum dots, and 2D materials. In 2019, with plasmonic nanocavities constructed with gold film and silver nanocubes, significant luminescence enhancement for upconversion nanocrystals was observed.[105]

According to the SEM image and schematic illustration in Fig. 22A, the fabricated nanocavity consists of a large-area gold film, silver cubes, and a sandwiched monolayer of upconversion nanocrystals. The size of the silver cube can directly determine the resonance band of the nanocavity structure. As simulated in Fig. 22B, a substantial electric field enhancement between the substrate and the silver cube can be observed. Substantial resonance band overlap with red upconversion emission can be achieved by selecting silver cubes of $\sim$90 nm in edge length (Fig. 22C). Based on simulations through coupling in the gold film-silver cube nanocavity, upconversion luminescence can be guided to a small corner and almost totally collected by an objective lens (Fig. 22D). The significant enhancement of upconversion luminescence induced by plasmonic nanocavity is demonstrated in Fig. 22E. Upon 980-nm excitation, some random red-emitting regions can be observed. Referenced by the SEM image (Fig. 22F and G), only fluorescence from areas with silver cubes on top of the upconversion nanocrystal monolayer can be distinguished. Fig. 22H shows green and red upconversion luminescence enhancement factors as a function of excitation power density. It is clear that upconversion emission can be significantly enhanced by the plasmonic resonance nanocavity, but the red emission (660 nm) features much higher luminescence enhancement. This can be ascribed to the reduced spectral overlap between the green emission (554 nm) and the plasmonic resonance. In addition, power-dependent investigations of the emission enhancement factor revealed that the effect of pump fluence on emission intensity is more predominant under low-power than under high-power excitation. To confirm the radiative rate acceleration, the luminescence lifetimes of samples with and without nanocavity coupling were compared (Fig. 22I and J). Interestingly, through coupling in the nanocavity, the lifetime of 660 nm luminescence can be shortened from 232 to 1.4 μs (Fig. 22J). For the lifetime of green emission, a change from 143 to 6 μs can also be achieved (Fig. 22I). Since the nonradiative decay

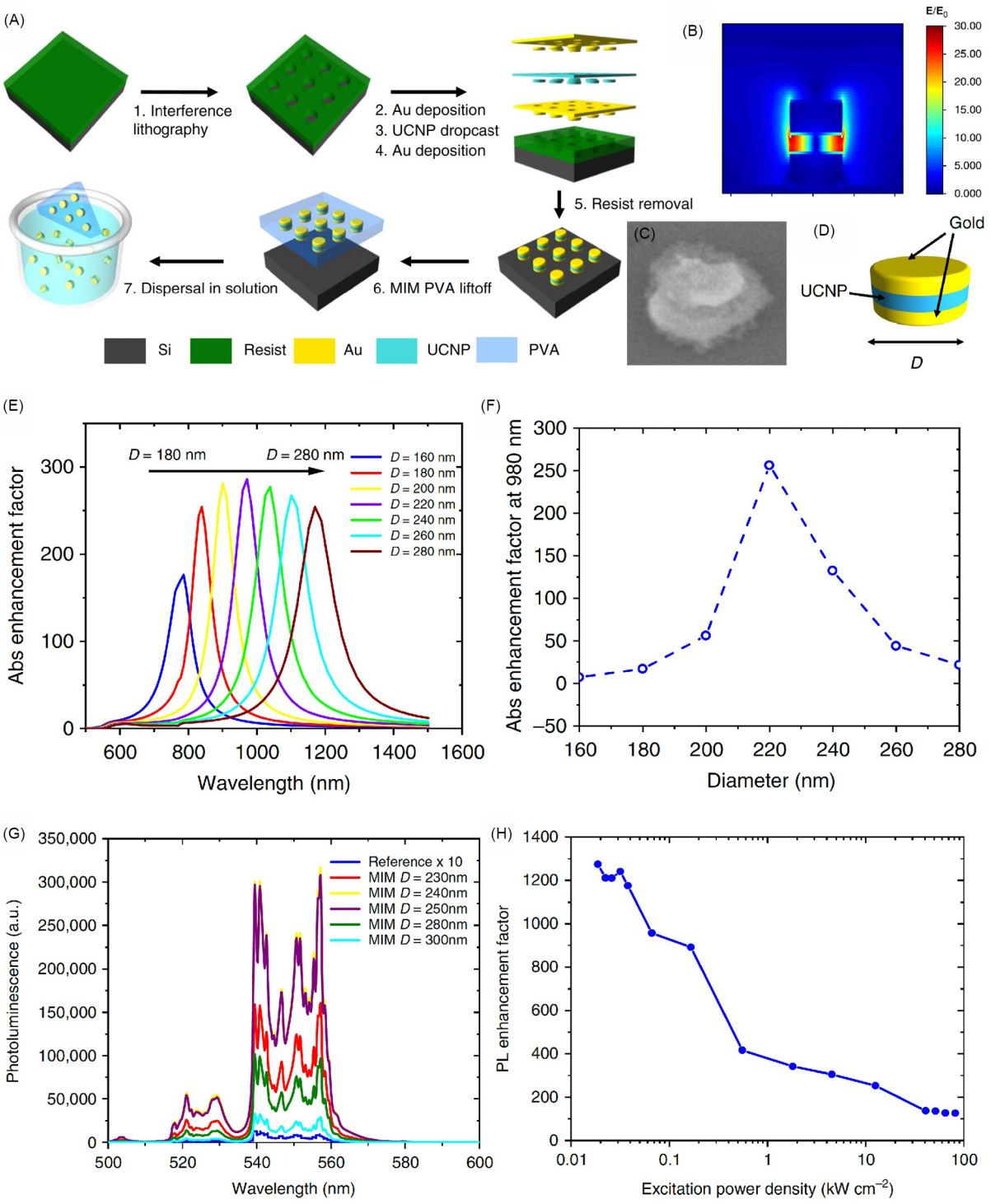

Fig. 21 (A) Metal-insulator-metal (MIM) fabrication process. (B) Simulated field profile under 980 nm normal incidence plane wave excitation. E field is normalized by incident plane wave amplitude E_0. (C) SEM image and (D) cartoon illustration of fabricated MIM nanocavity structure. (E) Simulated diameter dependence of plasmonic resonance and (F) absorption enhancement factor at 980 nm for various diameters. (G) Green upconversion emission spectra of the reference sample and metal-insulator-metal (MIM) structure of varying diameter under 980 nm excitation. (H) Upconversion luminescence enhancement factors for 250-nm-diameter MIM structure as a function of excitation power density. Printed with permission from Ref. Das, A.; Mao, C.; Cho, S.; Kim, K.; Park, W. *Nat. Commun.* **2018**, *9*, 4828.

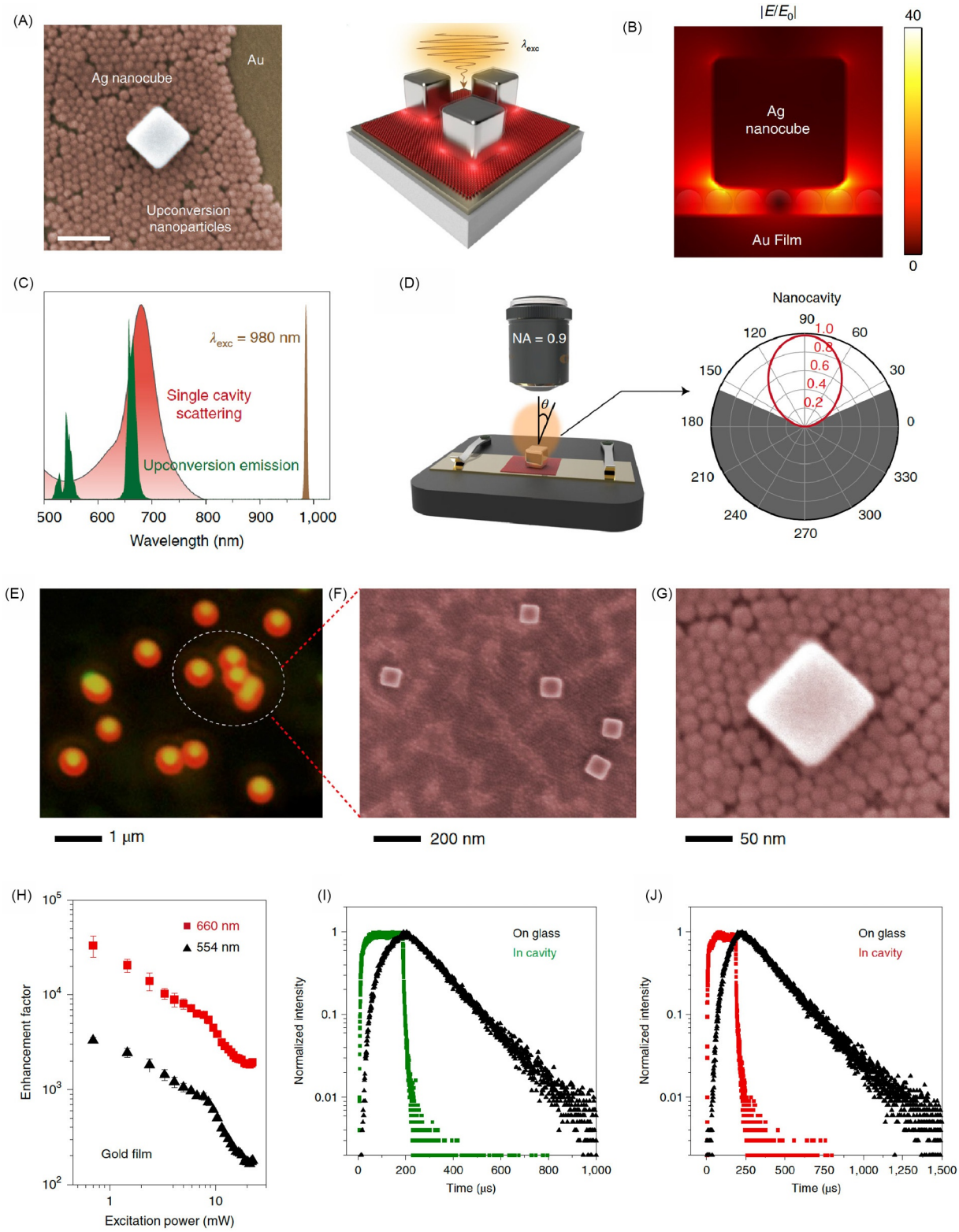

Fig. 22 (A) Schematic illustration and SEM image of plasmon nanocavity constructed by Au film-Upconversion nanocrystal-Ag nanocube. (B) Filed profile simulation for fabricated nanocavity. (C) Upconversion luminescence of Yb/Er codoped nanocrystals upon 980 nm excitation and simulated scattering spectrum of a single nanocavity. (D) Schematic of the experimental set-up designed for upconversion luminescence investigation (left). The simulated far-field radiation pattern of upconversion emission in nanocavity. (E) Upconversion photoluminescence imaging of the enhancement effect induced by plasmonic nanocavity coupling. (F) Enlarged SEM image of the circled region marked in (E). (G) High-resolution SEM imaging of the nanocavity. (H) Upconversion luminescence enhancement factor for nanoparticles located in the plasmonic nanocavity as a function of excitation power. (I, J) Luminescence lifetime for green (I) and red (J) upconversion emission of samples on the glass substrate and in nanocavity. Printed with permission from Ref. Wu, Y. et al. *Nat. Nanotechnol.* **2019**, *14*, 1110–1115. Copyright © 2019, Nature publication group.

cannot be significantly changed under current conditions, the drastic decline in lifetime can be ascribed to accelerated radiative decay, which eventually contributes to the upconversion output. Therefore, we predict that further enhancement of upconversion luminescence will be achieved by coupling upconversion nanocrystals in plasmonic resonance nanocavities with large, simultaneous resonance spectral overlap with the absorption and emission band of nanocrystals.

Besides silver and gold, aluminum has been used to construct plasmonic resonance cavities for luminescence enhancement. By coupling $NaGdF_4$:Yb/Er nanocrystals in the Al disk-Al film nanocavity, the position of the cavity resonance can be tuned to selectively enhance red or green emission.[106] As illustrated in Fig. 23A and B, upconversion nanocrystal-coupled Al nanocavities were fabricated by placing $NaGdF_4$:Yb/Er nanocrystals between a substrate and an Al disk. By increasing the diameter of the Al disk from 90 to 220 nm (Fig. 23C–E), reflection spectra and resonance bands were shifted from 400 to 1100 nm. Importantly, the red-to-green ratio of overall color output can be customized by changing the disk size that affects resonance band position. For instance, with a disk diameter of 160 nm, the constructed nanocavity shows a strong resonance band around 660 nm, which overlaps considerably with red emission band. Correspondingly, the resulting upconversion luminescence exhibited the highest red-to-green ratio and an orange color disk was observed in Fig. 23C. Since the size of each cavity can be controlled minutely, large-area color images exhibiting different luminescent color schemes of the same image can be printed (Fig. 23F). The left panel of Fig. 23F is a bright-field optical micrograph of "The Starry Night" (Vincent van Gogh, 1889), observed under white light illumination. However, upon 980 nm laser excitation, the same image shows a totally different color scheme consisting of green, yellow, and orange. This technique is up-and-coming for data encryption applications.

4.3 Electric hotspot generation through dielectric superlensing modulation

Unlike conventional luminescent probes, such as organic dyes and quantum dots, lanthanide upconversion materials feature distinct nonlinear optical properties. By absorbing multiple NIR photons sequentially, one photon with an appreciable anti-Stokes shift is emitted. Thus, upconversion luminescence power dependence follows an interesting rule of $I = P^{\hat{}}n$, where I, P, and n represent upconversion luminescence intensity, excitation power density, and the number of NIR photons absorbed in order to generate a single short-wavelength photon in a given upconversion process, respectively.[45] For instance, for a 4-photon upconversion process, its luminescence intensity can be amplified up to 16-fold, once the excitation power density is doubled, and this enhancement factor can be further amplified to a value of 81 with a corresponding power density increased three-fold. Therefore, increasing the excitation power density can be an effective approach for significant upconversion luminescence enhancement, especially for those cases governed by a larger number of photons.

With strong light confinement capability, dielectric microlenses can converge incident NIR light into a sub-micron-sized hotspot with ultra-high-power density.[107–109] Thus, by coupling dielectric microlenses with upconversion nanocrystals, remarkable enhancement in upconversion luminescence can be anticipated. Liang et al. have demonstrated five orders of magnitude enhancement in upconversion luminescence using polymeric microbeads for efficient excitation confinement (Fig. 24).[45] Polymeric microlenses were fabricated using the microfluidic method. By controlling the injection rate of the oil phase, poly (ethylene glycol) diacrylate (PEGDA) microbeads were customized from 5 to 100 μm in size. Fig. 24A shows the microscopy image of prepared PEGDA microbeads with a diameter of 20 μm. These polymeric microbeads are quite uniform and transparent. The incident light beam can be effectively focused on the rear side of the microbeads (inset image). To study the enhancement effect of prepared dielectric microlenses, PEGDA microbeads were self-assembled to form a large-area monolayer on a PDMS layer consisting of upconversion nanocrystals (Fig. 24B). Here, $NaYF_4$:Yb/Er@$NaYF_4$ and $NaGdF_4$:Yb/Tm@$NaGdF_4$:Eu nanocrystals are prepared and embedded in the PDMS layer for luminescence enhancement investigation. As simulated in Fig. 24C, prepared PEGDA microbeads can confine the incident NIR light (980 nm) into an ultra-small hotspot with full-width at the half-maximum (FWHM) of about 680 nm, which is over two orders of magnitude smaller than the size of microlens selected. Importantly, according to the electric field profile, the incident light intensity can be amplified over 300-fold. With the assistance of microbeads, upconversion luminescence from nanocrystals embedded in the PDMS film can be efficiently collected in the far-field (Fig. 24D). For the upconverting PDMS film as the control, only 0.77% of the emitted photons can be collected by a 10X objective lens with a NA of 0.3. However, once the microbead is placed on the film, the collection efficiency was increased to about 6.14%, an 8-fold enhancement in luminescence collection efficiency. Therefore, the dielectric microlens monolayer can contribute to the enhancement in both excitation power density and luminescence collection efficiency. Fig. 24E shows the microscopic fluorescence imaging of PDMS films doped with $NaYF_4$:Yb/Er@$NaYF_4$ and $NaGdF_4$:Yb/Tm@$NaGdF_4$:Eu upconversion nanocrystals with and without the coverage of a microlens monolayer. Upon 980 nm excitation, Er^{3+}-activated nanocrystals showed yellow-green emission with two characteristic bands centered around 540 and 654 nm. For crystals co-activated with Tm^{3+}/Eu^{3+} dopants, characteristic bands centered around 450 and 614 nm were observed, arising from $^1D_2$ -> $^3F_4$ transition of Tm^{3+} and $^5D_0$-> $^7F_2$ transition of Eu^{3+}. Without coupling of the PEGDA microbead monolayer, no upconversion emission from PDMS films can be observed. However, bright luminescence from both Er^{3+} and Tm^{3+}/Eu^{3+} coactivated PDMS films can be clearly seen, signifying that significant upconversion luminescence enhancement can be achieved through microlens monolayer coupling. For systematic investigation of the enhancement contributed by the dielectric microlens monolayer, upconversion luminescence spectra of both $NaYF_4$:Yb/Er@$NaYF_4$ and $NaGdF_4$:Yb/Tm@$NaGdF_4$:Eu embedded PDMS films are recorded at varied excitation power densities. As shown in Fig. 24F, utilization of a dielectric microbead monolayer can induce an immense luminescence enhancement in all-optical transitions of activators under investigation. It is important to note that in all cases, luminescence enhancement is more significant under low-power excitation. Luminescence enhancement with dielectric superlenses depends strongly on the upconversion population of different activators. For example, under 1.5 W cm^{-2} power excitation, the upconversion luminescence of Eu^{3+} was

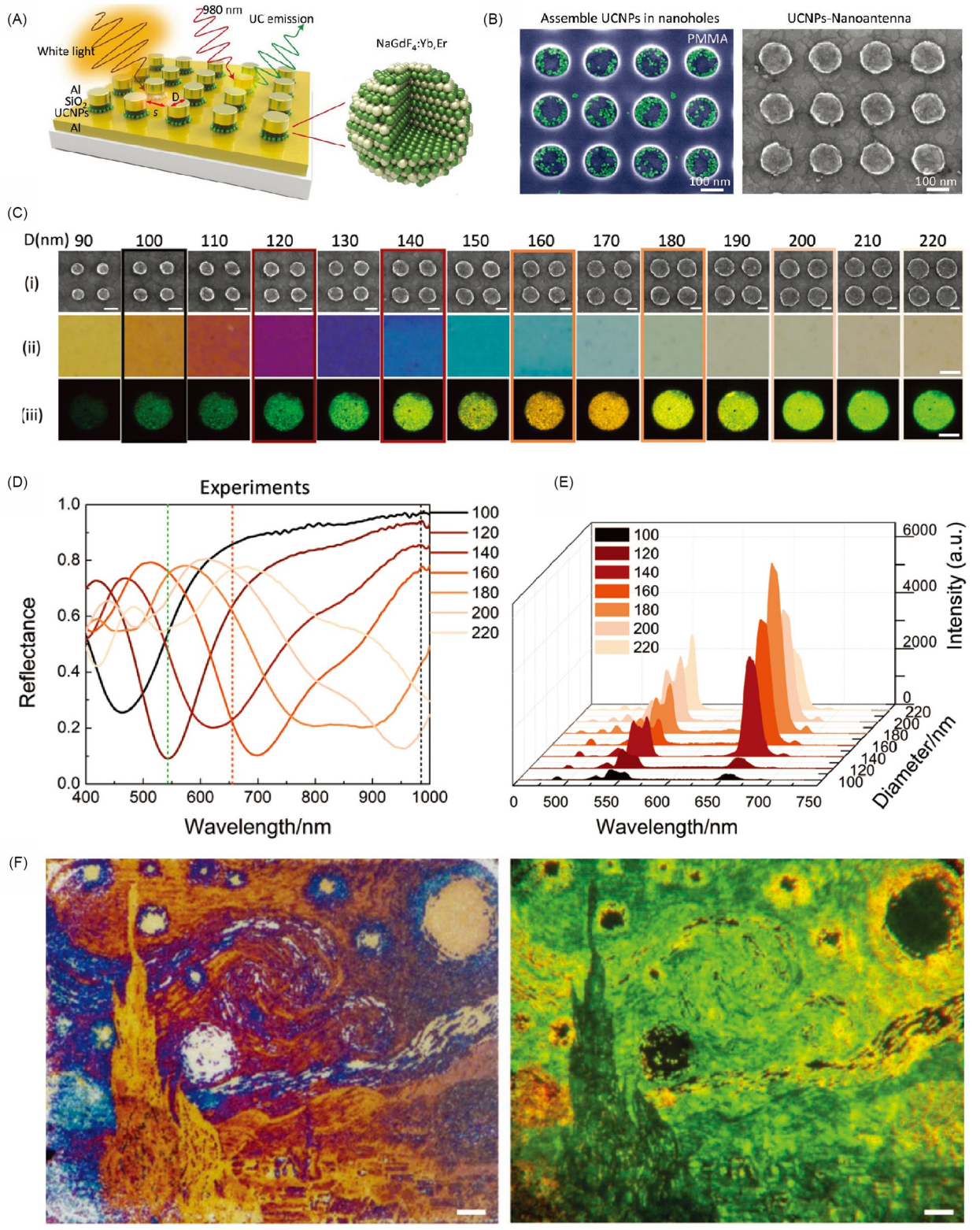

Fig. 23 (A) Schematic showing tunable resonator-upconverted emission (TRUE) color pixel arrays. (B) SEM image of the assembled upconversion nanocrystals in PMMA nanoholes (left) and image of fabricated pixel arrays. (C) SEM i), reflected bright field ii), and upconversion luminescence iii) color patches of pixel arrays. (D) Measured reflectance spectra of TRUE color pixels. (E) Upconversion luminescence of pixel arrays with different diameters. (F) Optical micrograph and its corresponding luminescence image of "The Starry Night" using $NaYF_4$:Yb/Er as upconversion nanocrystals. Scale bar is 10 μm. Printed with permission from Ref. Liu, H. et al. *Adv. Mater.* **2019**, *31*, 1807900. Copyright © 2019 WILEY-VCH Verlag GmbH & Co. KGaA, Weinheim.

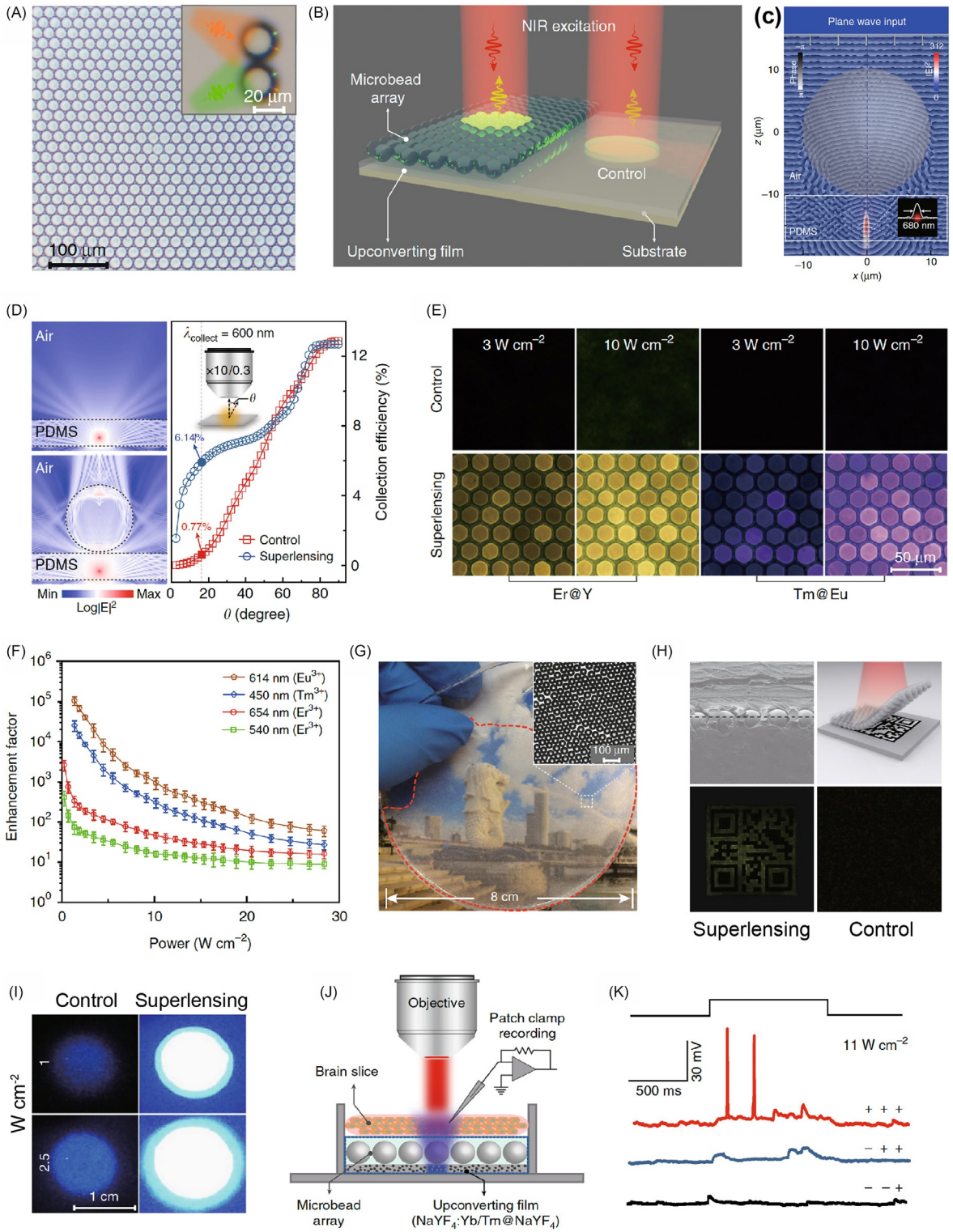

Fig. 24 (A) Photographic image of the as-prepared PEGDA polymeric microbeads. (Inset) Photographic image showing the convergence of two intersected orange and green LED beams into two small focal spots after passing through the microbeads. (B) Schematic illustration of the experimental setup designed for luminescence amplification investigation. (C) FDTD simulation of the electric field distribution and phase variation of NIR excitation light after passing through the dielectric microbead. (D) Comparative simulations of the far-field emission collection efficiency for upconversion enhancement, obtained in the presence or absence of a dielectric microbead. (E) Upconversion luminescence images of the upconversion nanocrystal-embedded PDMS upconverting films recorded with and without the microbead coverage upon 980-nm excitation at different intensities. (F) Power-dependent investigations of microbead monolayer induced-luminescence enhancement for PDMS films comprising $NaYF_4$:Yb/Er@$NaYF_4$ and $NaGdF_4$:Yb/Tm@$NaGdF_4$:Eu nanoparticles. (G) Photographic image of a PDMS composite sheet comprising 50 μm $BaTiO_3$ microbeads. Inset shows the ensemble of the microbeads used for making the planar sheet. (H) Demonstration of document security application using the composite sheet. Printed with permission from Ref. Liang, L. et al. *Nat. Commun.* **2019**, *10*, 1391. Copyright © 2019, the authors.

enhanced by over five orders of magnitude. However, only ~100-fold enhancement for emission at 540 nm (Er^{3+}) was recorded. The diminished enhancement factor at higher excitation power can be attributed to luminescence saturation at high power. Importantly, the huge difference in the enhancement factor for emission originating from different optical transitions can be ascribed to the difference in the number of photons involved in each upconversion process. For example, by accepting migrated energy from Gd^{3+} sublattices, Eu^{3+} emission features a five-photon upconversion process. In contrast, the green emission of Er^{3+} comprises only two-photon energy transfer. As mentioned above, luminescence governed by more steps of NIR pumping shows much larger luminescence enhancement under increased excitation power. For convenience and improved mechanical strength, a transparent, planar composite PDMS sheet was produced by incorporating a close-packed $BaTiO_3$ microbead monolayer into a PDMS precursor (Fig. 24G). Due to the high relative refractive index between $BaTiO_3$ (2.1) and PDMS (1.4), the composite film worked well for light confinement. The composite film was applied to improve document security applications involving upconversion-based encoding techniques. As shown in Fig. 24H, with the help of the as-fabricated PDMS sheet, an encrypted quick-response code, printed on a piece of paper using green-emitting $NaYF_4$:Yb/Er@$NaYF_4$ nanoparticle inks, was readily decoded with a tungsten lamp at sub-solar irradiance (~12 mW cm^{-2}). In addition to PEGDA and $BaTiO_3$ materials, other dielectric microlenses (e.g., SiO_2 and PMMA microbeads) have proven efficacious for upconversion luminescence enhancement.

Interestingly, yeast cells or human cells with spherical or disk-like shapes can also act as natural bio-microlenses for luminescence enhancement (Fig. 25).[110] Due to the photonic nano-jet effect of the bio-microlens, NIR excitation can be confined in a

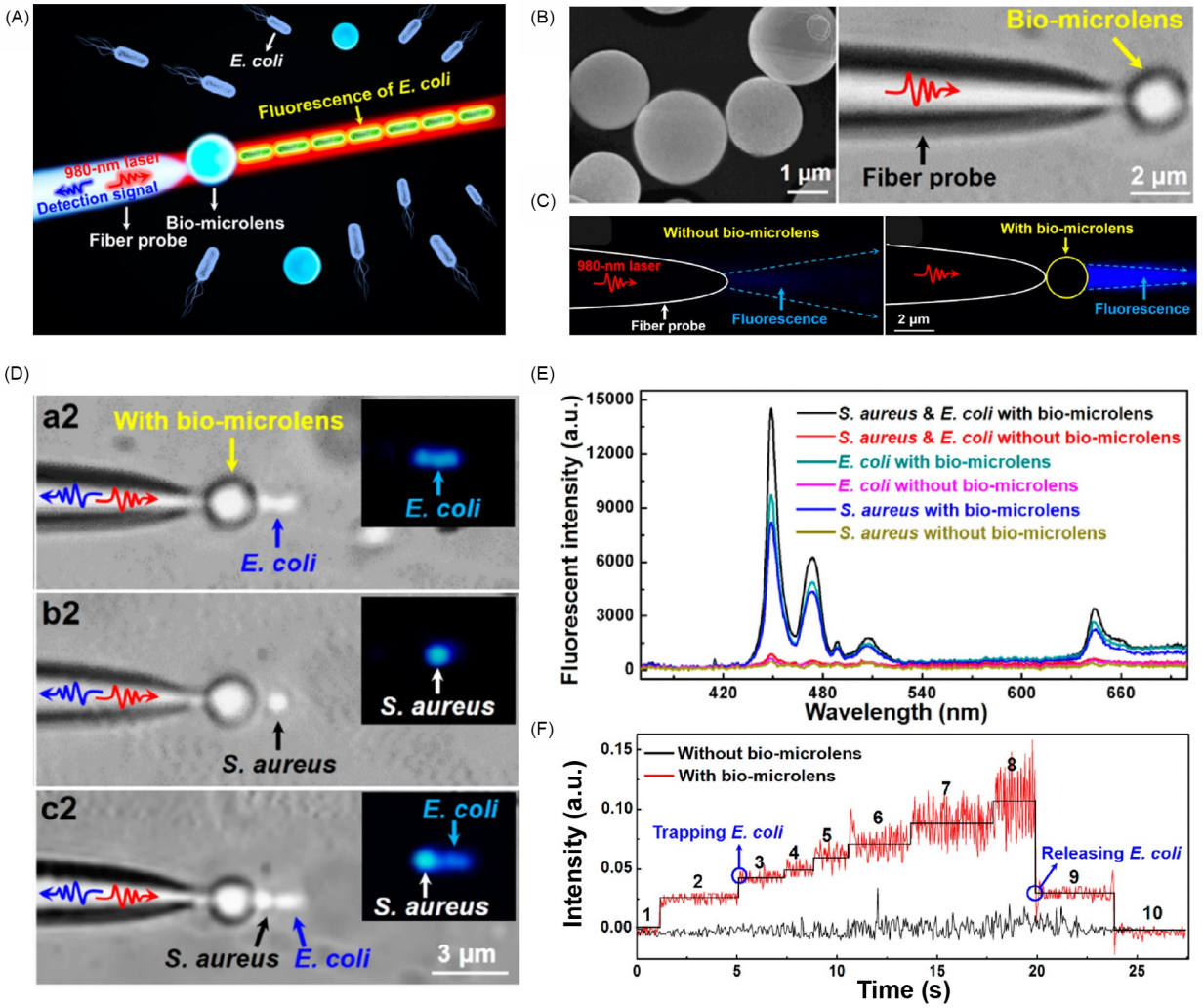

Fig. 25 (A) Schematic showing the upconversion luminescence enhancement and optical trapping features of the microlens. (B) SEM image of the yeast cell bio-microlenses with an average diameter of 2.0 μm (left). An optical image showing a bio-microlens was trapped at the tip of an optical fiber probe (right). (C) Fluorescent images of outputted light from a fiber probe without and with a bio-microlens. (D) Optical microscope images showing a single *E. coli* (a2)/a single *S. aureus* (b2)/and an *S. aureus* and *E. coli* (c2) were optically trapped by a fiber probe with a 2 μm yeast cell bio-microlens. Insets of (a2) – (c2) show the corresponding fluorescent images of the trapped *E. coli* or *S. aureus*. (E) The upconversion fluorescent intensity of single *S. aureus* and *E. coli* was detected by a fiber probe with or without a bio-microlens. (F) Real-time detection of B_s in the trapping and releasing process of the *E. coli* chain by the fiber probe with and without a bio-microlens. Printed with permission from Ref. Li, Y. et al. *ACS Nano* **2017**, *11*, 10672–10680. Copyright © 2017 American Chemical Society.

subwavelength region, enhancing upconversion luminescence by two orders of magnitude. As a result of enhanced luminescence, single-cell imaging and real-time detection of pathogenic bacteria can be achieved. Fig. 25A illustrates the schematic of luminescence enhancement and signal collection of an *E. coli* chain with a bio-microlens at the end of an optical fiber. With an average diameter of 2 μm, yeast cells have smooth surfaces and can work as dielectric micro-lenses for light confinement. To conduct measurements, a single yeast cell was first trapped at the end of a fiber probe by the incident NIR laser beam (Fig. 25B). Then the probe was inserted into a solution containing blue-emitting $NaYF_4$:Yb/Tm nanocrystals for luminescence collection. Upon launching a 980-nm laser with an optical power of 3 mW, strong blue-emitting luminescence can be imaged with a bio-microlens trapped on the fiber tip. In contrast, the emission is difficult to detect when only the fiber was used (Fig. 25C), indicating bio-microlens-mediated luminescence amplification. Moreover, using the bio-microlens, optical trapping of single or even chained nanocrystals can be achieved with significantly boosted luminescence. As demonstrated in Fig. 25D, upconversion nanocrystal-modified *E. coli* and *S. aureus* cells can be trapped on the rear side of the bio-microlens for luminescence investigation. With bio-microlens coupling, upconversion luminescence from trapped single or chained cells can be amplified over 110 times (Fig. 25E). More interestingly, using this bio-microlens optical trapping system, trapping and releasing of fluorescent *E. coli* cells can be distinguished through tracing of collected luminescence intensity with high signal-to-noise ratios (Fig. 25F). This real-time detection strategy using a bio-microlens can be used for monitoring the trapping process of the bacteria, especially in very limited spaces where direct observation by an optical microscope cannot be performed.

Apart from the above-mentioned single bio-microlens and dielectric microlens monolayer obtained through self-assembly, polymeric microlens arrays (MLAs) consisting of abundant hemisphere-like microlens units are commercially available and have been applied to improve photodetector sensitivity in the NIR region (Fig. 26).[36] Fig. 26A illustrates a configuration employing MLAs for upconversion luminescence enhancement. By attaching the MLA layer (see the SEM image in Fig. 26B) on top of a film consisting of gold nanorods and upconverting nanocrystals, localized excitation power density in the film can be remarkably enhanced. Moreover, gold nanorods mixed with core-shell-shell (CSS) upconversion nanocrystals can also enhance luminescence intensity due to the large overlap between the plasmonic resonance band with the absorption spectra of lanthanide sensitizers and activators (Nd^{3+}, Yb^{3+}, and Er^{3+}) (Fig. 26C and D). Thus, by simultaneous coupling with dielectric superlensing and surface plasmons, the excitation field surrounding upconversion nanocrystals can be remarkably improved, drastically enhancing luminescence. Selection of MLA of suitable height for nanocrystal coupling can enhance emission up to 6000-fold (Fig. 26E). However, MLAs with longer focusing distances perform worse since the optical hot spot is beyond the upconverting film (see Fig. 26F). For upconverting film co-coupled with the MLA film and Au nanorods, the enhancement factor can reach over 22,000-fold. Considering the large upconversion luminescence enhancement, a multiband responsive NIR photodetector (MLA/Au NR/CSS/$MAPbI_3$) was fabricated using $MAPbI_3$ film as the photon-to-current converting material. By virtue of the spectral overlap between the blue/green upconversion emission and the absorption spectrum of $MAPbI_3$ film, efficient upconverted photon-to-current conversion can be achieved using the MLA/Au NR/CSS/$MAPbI_3$ photodetector (Fig. 26G). Fig. 26H presents the performance of the prepared photodetector. Since the upconversion nanocrystal can be stimulated by multiple excitation bands around 808, 980 and 1540 nm, the fabricated photodetector responds strongly to these excitation bands. Additionally, the device with simultaneous coupling of superlensing and plasmonic resonance features the best NIR photon-to-current performance, especially upon 808-nm excitation. Taken together, dielectric superlensing coupling provides an efficient approach for upconversion luminescence enhancement, holding promise for many emerging applications.

5 Emerging applications

The study of upconversion nanomaterials has made considerable progress in terms of optical control and luminous efficiency enhancement, especially at single-particle levels. Thus, upconversion nanocrystals have enabled applications in various fields, including super-resolution imaging, lasing, and optogenetics.

5.1 Super-resolution imaging

Compared to commonly used luminescent probes, such as organic dyes and quantum dots, lanthanide-doped upconversion nanocrystals offer many distinct features, including ultrahigh photostability, a nonlinear optical emitting process, a tunable emission band from the deep-UV to the NIR region and ultralong luminescent lifetime, as well as low background noise. Recently, upconversion nanocrystals have been developed as super-resolution imaging nanoprobes based on their unique optical properties.[28,29,111–116]

In 2017, upconversion nanocrystals highly doped with Tm^{3+} activators were applied to stimulated emission depletion (STED) microscopy.[29] For conventional STED microscopy employing organic dye molecules, a gaussian excitation beam and a donut-shaped depletion beam were applied simultaneously to a sample through the objective lens (Fig. 27A).[117–120] The luminescent sample was pumped to an excited state and then generated spontaneous emission at nanosecond scale. Upon addition of the depletion beam, stimulated emission was triggered, and the fluorescence was suppressed in which the excitation and depletion beams overlapped. In such a way, the effective point spread function can be effectively reduced compared to the original gaussian excitation beam (Fig. 27B). Upon further increasing the depletion power, the emitting area was remarkably reduced to sub-20-nm scale. Although organic dye-mediated STED microscopy has been successfully applied to studies of subcellular structures and bio-events, this technique suffers many limitations. To achieve effective fluorescence suppression, an ultra-high power pulsed

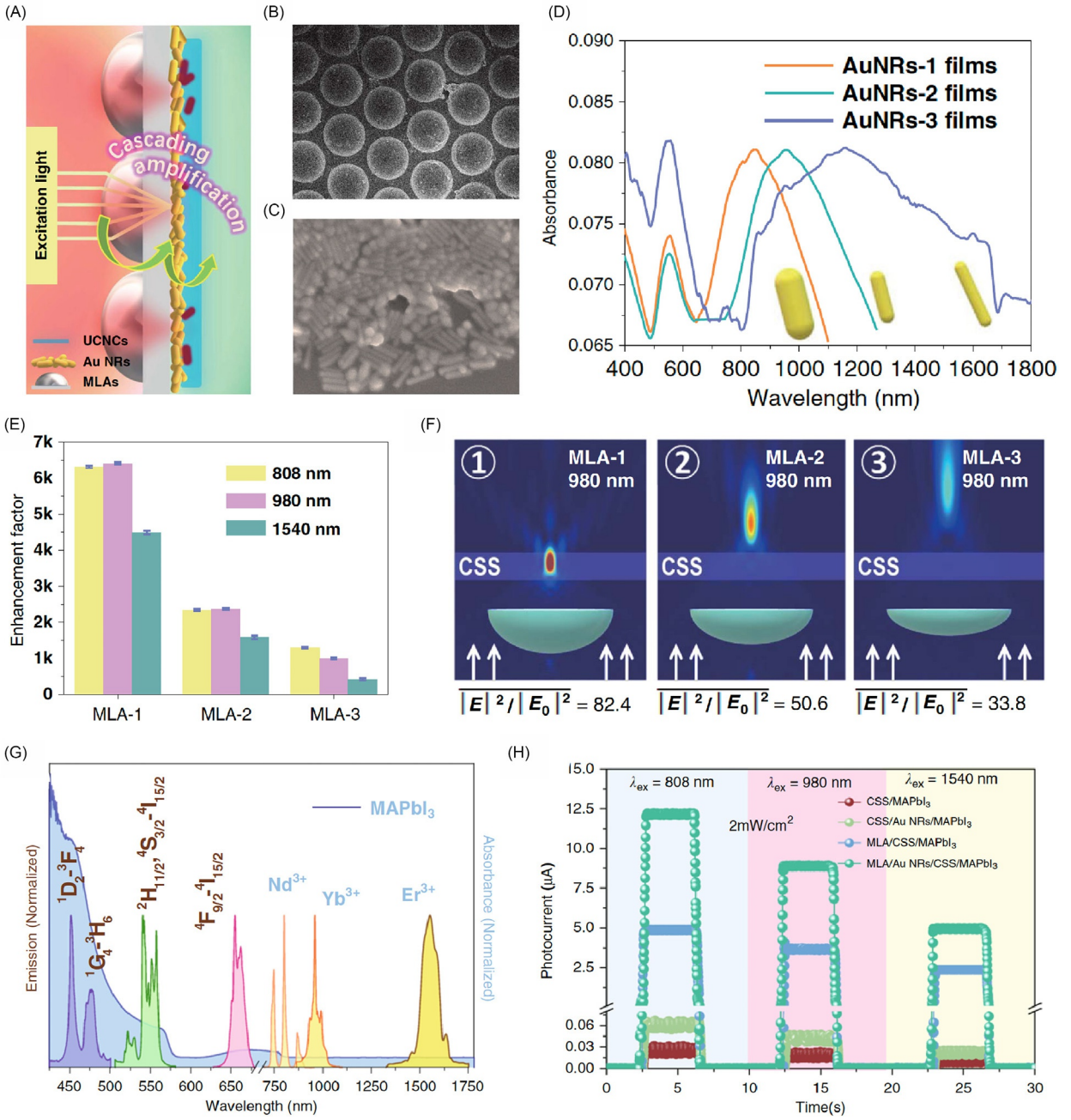

Fig. 26 (A) Experimental design for upconversion luminescence enhancement using dielectric superlensing and surface plasmon coupling. (B) SEM image of the microlens. (C) SEM image for prepared Au nanorods. (D) Absorption spectra of gold nanorods with different aspect ratios. (E) Upconversion luminescence enhancement factors based on different microlenses upon 808 nm, 980 nm, and 1540 nm excitation. (F) Simulation results for light confinement effect of different microlenses. (G) Spectra overlap between upconversion luminescence and perovskite film absorption. (H) Photoresponse of different photodetector samples upon 808 nm, 980 nm, and 1540 nm excitation. Printed with permission from Ref. Ji, Y. et al. *Light: Sci. Appl. 9, 184 (2020).* Copyright © 2020, Nature publication group.

depletion beam is usually required to compete with the fast spontaneous decay process. Thus, the whole system can be very complicated due to the synchronization of excitation and detection. More importantly, because the organic dye molecules suffer severe photobleaching, especially upon high-power depletion, image brightness quickly declines after several frames. Thus, super-resolution imaging of long-term bio-events is not plausible by traditional STED microscopy. However, these challenges can be overcome using upconversion nanocrystal-based STED microscopy.

As illustrated in Fig. 28A, high (8%) and low (1%) Tm-activated $NaYF_4$:Yb/Tm upconversion nanocrystals with intense blue emission were selected for a STED imaging demonstration. Upon 980-nm excitation, both high and low Tm-doped nanocrystals showed strong blue emission. However, when an 808-nm depletion beam was applied, emission from highly Tm-doped nanocrystals was turned off, whereas nanocrystals with low Tm doping remained unaltered. Therefore, blue-emitting upconversion nanocrystals with highly doped Tm activators can be engineered for STED imaging. The mechanism for upconversion luminescence

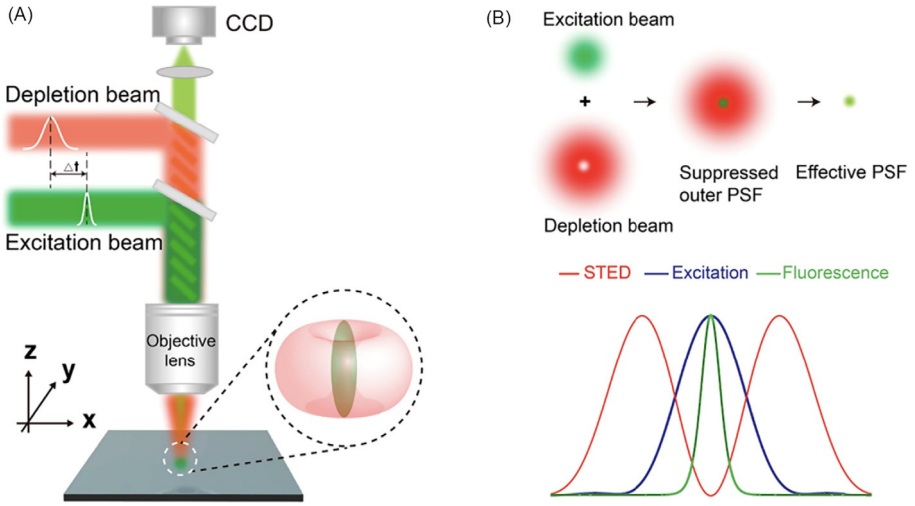

Fig. 27 (A) Experimental setup for conventional STED microscopy. (B) Illustration of point-spread function for the excitation, depletion beam, and the effective point-spread function (PSF) upon excitation and depletion beam overlapping. Printed with permission from Ref. Qin, X.; Xu, J.; Wu, Y.; Liu, X. *ACS Cent. Sci.* **2019**, *5*, 29–42. Copyright © 2019 American Chemical Society.

depletion is illustrated in Fig. 28B. Upon 980-nm pumping, multiple band emission from Yb/Tm-codoped $NaYF_4$ nanocrystals was produced through conventional energy transfer upconversion. Importantly, with increased Tm^{3+} dopants in the host lattice, the distance among adjacent activators can be greatly reduced; strong cross-relaxation would dominate the Tm^{3+} activator sublattice. As such, activated Tm^{3+} emitters would be redistributed to an energy level close to $^3H_4$, from which effective stimulated emission could be triggered by 808-nm depletion. Once the $^3H_4$ level is depopulated by the depletion beam, energy transfer upconversion for 455-nm emission could be suppressed. In contrast, for a sample with low Tm^{3+} activation, cross-relaxation is subsidiary and the depletion beam contributes to upconversion to a less extent. Upconversion nanocrystals with different Tm^{3+} dopant contents showed large differences in luminescence quenching upon 808-nm depletion (Fig. 28C). Nanocrystals with high-Tm doping exhibited more efficient luminescence suppression, and their saturation power density (0.19 MW cm^{-2}) was significantly reduced to a value two orders of magnitude lower than that of organic dye-mediated STED microscopy. The high performance was attributed to high-quality population inversion induced by cross-relaxation and long luminescence lifetime. STED imaging with 13-nm and 40-nm upconversion nanocrystals was also conducted (Fig. 28D). Resolution was considerably enhanced by increasing the power of the 808-nm depletion beam. Furthermore, selection of smaller upconversion nanocrystals improves imaging resolution slightly. Single-particle imaging results are profiled in Fig. 28E–G. Upon 980-nm excitation, the measured FWHM for a single particle is higher than 400 nm. However, this value can be reduced to around 30 nm once a depletion beam is applied.

Similar work was published by Zhan's group with 10% Tm^{3+}-activated $NaYF_4$:Yb/Tm upconversion nanocrystals.[28] Their investigations show that the optimum doping with Tm^{3+} activators is 10 mol%, which results in the highest depletion efficiency of 96% (Fig. 29A). For nanocrystals with Tm^{3+} doping lower than 3 mol%, luminescence enhancement instead of suppression occurs. Further increasing the doping amount of Tm^{3+} ions reduces depletion efficiency slightly, but no less than 80%. Therefore, the high doping of Tm^{3+} activators is a prerequisite for efficient luminescence suppression. Importantly, Zhan's group also found that the most efficient wavelength for the depletion beam is 810 nm (Fig. 29B). Importantly, this study proposed a different mechanism for efficient luminescence depletion of highly Tm^{3+}-activated upconversion nanocrystals. As illustrated in Fig. 29C, the depletion transition is from $^1D_2$ to $^1G_4$, instead of the $^3H_4$-to-$^3H_6$ transition proposed by Jin's group.[29] By coupling Tb^{3+} emitters in core-shell upconversion nanocrystals ($NaGdF_4$:Yb/Tm@$NaGdF_4$:Tb), dual-color STED imaging was achieved. As demonstrated in Fig. 29D, upon 975-nm excitation, multiple nanoparticles can be imaged. By adding suitable filters, blue and green upconversion luminescence from Tm^{3+} and Eu^{3+} activated nanocrystals could be directly extracted or achieved through image substruction. After adding the depletion beam (Fig. 29E), dual-color STED imaging can be achieved. For practical application, desmin on the cytoskeletons of fixed HeLa cancer cells was labeled with antibody-conjugated upconversion nanocrystals (Fig. 29F and G). With only 975-nm excitation, subcellular structures labeled with $NaYF_4$:Yb/Tm nanocrystals can be clearly imaged. When the 810-nm depletion beam was added, resolution can be effectively enhanced to about 80 nm. This is the first demonstration of successful immunolabeling of fine subcellular structures, as well as the first demonstration of super-resolution cell imaging using upconversion nanocrystals. However, labeling quality using upconversion nanocrystals larger than 10 nm still has ample room for improvement.

Not all upconversion nanocrystals meet the critical criteria for STED imaging application. However, all of them can be used for sub-diffraction imaging due to their intrinsic nonlinear optical nature. At the end of the last century, a conceptually different super-resolution approach was developed to conveniently achieve 3D sub-diffraction imaging on a standard confocal microscope without the need for setup modifications and image post-processing. By using super-linear emitters, imaging resolution can be effectively improved since the central part of the scanning beam yields the most significant emission, which results in a region smaller than the size of the beam. Thus, the stronger the super-linearity, the smaller the region of significant emission, and the better the resolution.

Since lanthanide photon upconversion is usually governed by two–/three–/four- and even five-photon processes, its super-linearity is much higher than that of organic dyes that are conventionally used for two-photon imaging. More importantly,

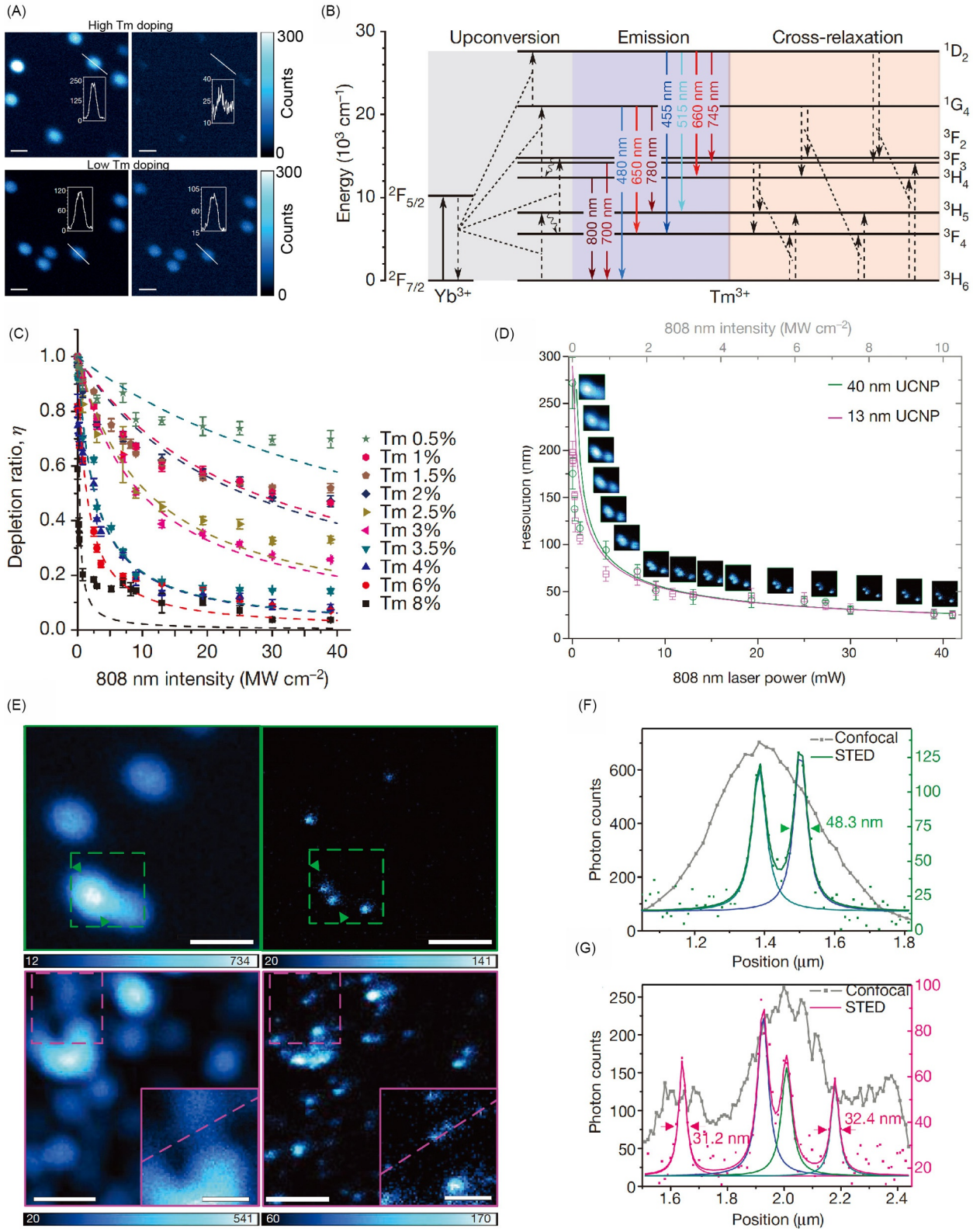

Fig. 28 (A) Upconversion luminescence imaging of 8% and 1% Tm activated-$NaYF_4$:Yb/Tm nanocrystals upon 980-nm excitation and 808-nm depletion. (B) Schematic showing the blue upconversion depletion mechanism of highly Tm doped upconversion nanocrystals. (C) Depletion efficiency versus depletion power of nanocrystals doped with different Tm concentrations. (D) Super-resolution curve of highly doped upconversion nanocrystals at different depletion powers. (E) Comparison of confocal and STED imaging of highly doped upconversion nanocrystals with diameters of 40 nm (top panel) and 13 nm (bottom panel), respectively. (F, G) Corresponding line profiles of upconversion imaging with and without depletion beam. Printed with permission from Ref. Liu, Y. et al. *Nature* **2017**, *543*, 229–233. Copyright © 2017, Macmillan Publishers Limited, part of Springer Nature.

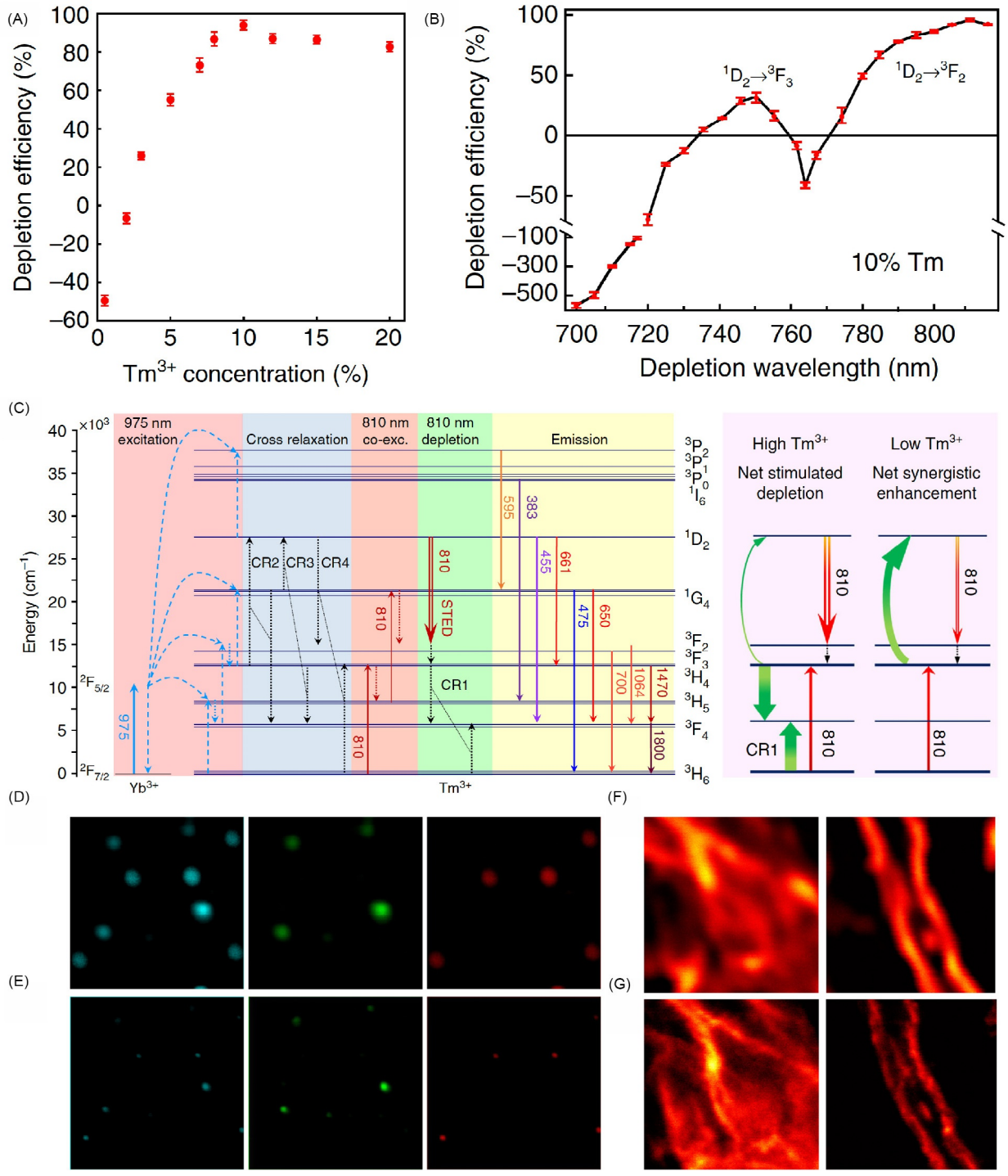

Fig. 29 (A) Depletion efficiency of $NaYF_4$:Yb/Tm upconversion nanocrystals with different Tm dopant amounts. (B) Depletion efficiency of upconversion luminescence at 455 nm versus depletion beam wavelength. (C) Proposed cross-relaxation-mediated luminescence depletion upon 975-nm excitation and 810-nm depletion. (D, E) Dual-color upconversion confocal and STED imaging using $NaYF_4$:Yb/Tm and $NaGdF_4$:Yb/Tm@$NaGdF_4$:Tb nanoparticles upon 975-nm excitation and 810-nm depletion. (F, G) Immunofluorescence labeling and super-resolution imaging of cellular cytoskeleton protein desmin with antibody-conjugated upconversion nanocrystals upon 975-nm excitation and 810-nm depletion. Printed with permission from Ref. Zhan, Q. et al. *Nat. Commun.* **2017**, *8*, 1058. Copyright © 2017, the authors.

the multiphoton absorption process of lanthanide upconversion offers an excitation threshold orders of magnitude lower.[121] Thus, lanthanide upconversion nanocrystals present a highly promising class of luminescent materials for sub-diffraction imaging applications.

The design of upconversion super-linear excitation-emission (uSEE) microscopy is illustrated in Fig. 30A.[116] Upon NIR excitation, the blue emission of $NaYF_4$:Yb/Tm nanoparticles can be collected through the same objective lens and the

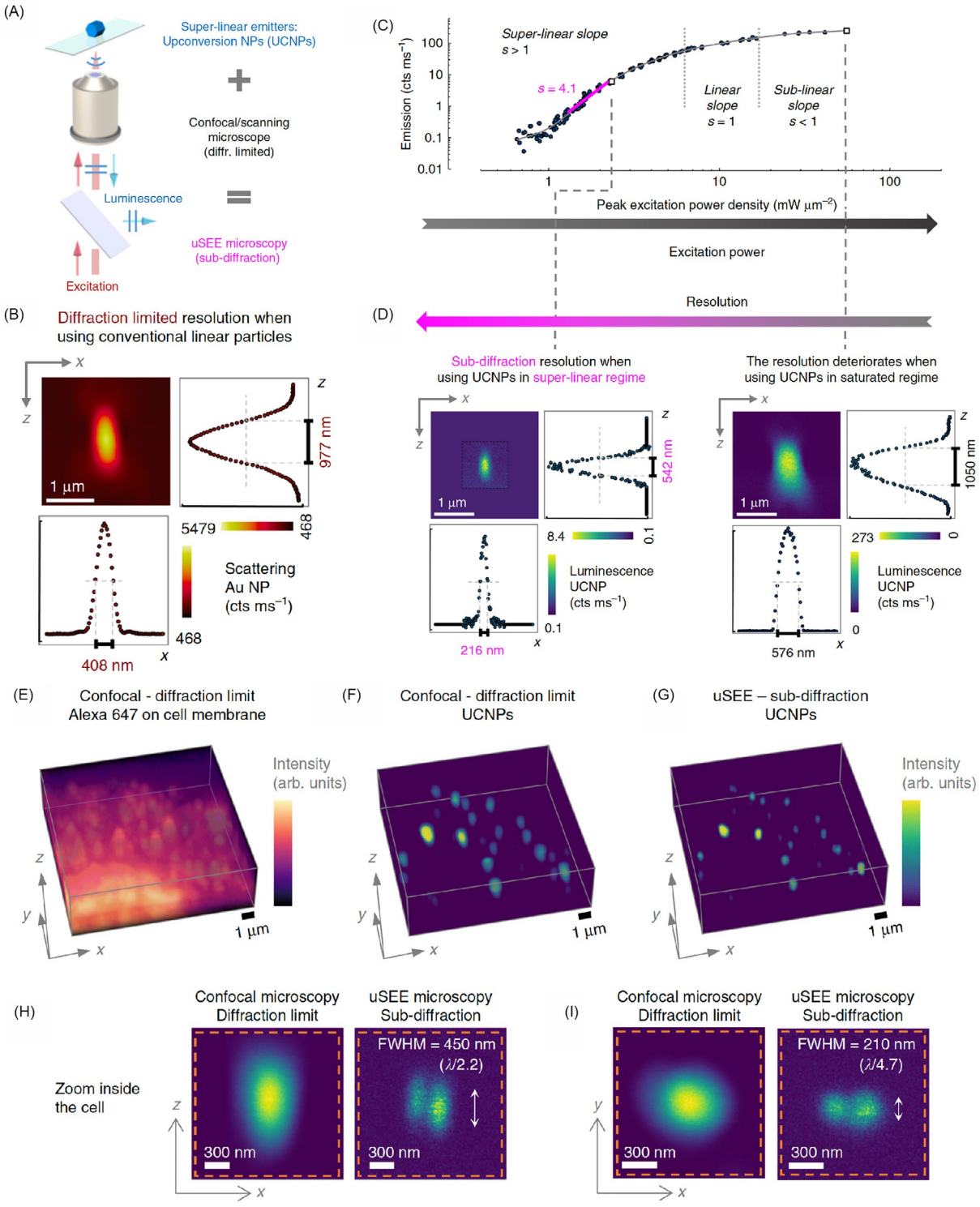

Fig. 30 (A) Setup for achieving sub-diffraction resolution imaging using a conventional confocal microscope. (B) Experimentally obtained point spread function of the 977-nm excitation beam by scanning a gold particle. (C) Upconversion luminescence (455 nm) power dependence of $NaYF_4$:Yb/Tm nanocrystals. (D) Measured point spread function of the 977-nm beam by scanning a single upconversion nanocrystal under low and high power excitation. (E) Confocally imaged 3D z-stack of a cell incubated with Alexa 647 dye. (F, G) Confocal images of upconversion nanocrystals inside the cell were taken at power densities of 11.8 (F) and 1.7 mW μm^{-2} (G). (H, I) Measured axial (H) and lateral (I) resolution of upconversion nanocrystals inside the cell. Printed with permission from Ref. Denkova, D. et al. *Nat. Commun.* **2019**, *10*, 3695. Copyright © 2019, the authors.

sub-diffraction image can be directly obtained after one scanning. The point spread function of the excitation beam (976 nm) was obtained by scanning around a gold nanoparticle. The measured FWHM for the axial and lateral directions is 977 nm and 408 nm, respectively (Fig. 30B). For linear emitter imaging using a 977-nm beam, resolution would be extremely low in both x-y and z directions. This situation is quite different when upconversion nanocrystals are selected as emitters. For $NaYF_4$:Yb/Tm nanocrystals chosen in this work, their super-linear optical properties were characterized by measuring their luminescence intensity at 455 nm as a function of the excitation power density (Fig. 30C). In a log-log plot, the value of *s* represents the slope of the curve at a certain excitation power. At low excitation intensity (<1 mW μm^{-2}), the nanocrystals are barely luminescent. Further increasing the excitation power results in steep luminescence intensity increase where the particle is in the super-linear regime with *s* larger than 1. In a power region from around 1 to 2.5 mW μm^{-2}, the slope achieves a constant of $\sim$4.1. However, the slope drops quickly to $\sim$1 upon further increases in excitation power density. These data suggest that upconversion nanocrystals can work as superior super-linear emitters for uSEE microscopy imaging only in a certain power range. As evidenced in Fig. 30D, the axial and lateral FWHM of excitation PSFs can be reduced to 542 and 216 nm when the excitation power is tuned into the super-linear region. However, when working far away from this region, corresponded values can be extended to 1050 and 576 nm, even larger than those of the original PSF. Considering the large improvement in resolution at 3D, sub-diffraction uSEE 3D microscopy imaging of cells labeled with upconversion nanocrystals is possible (Fig. 30E–I). For a sample labeled with the commonly used Alexa 647 dye, the contrast of the obtained 3D image is poor due to strong autofluorescence (Fig. 30E). The noisy background can be totally eliminated when upconversion nanocrystals are used for labeling (Fig. 30F). Furthermore, when operating in the super-linear region, the imaging resolution of *Z*-stack imaging is clearly improved (Fig. 30G). Figs. 30H and I show the measured PSFs in 3D upon excitation at different power regimes. Working in the super-linear regime, a 450-nm resolution along the z-axis and a 210-nm resolution in the x-y plane can be achieved.

Although the current work succeeds in achieving sub-diffraction imaging, resolution is still quite poor and sub-100 nm lateral resolution imaging is anticipated. Besides designing upconversion nanocrystals that can be excited by short-wavelength lasers, nanocrystals featuring much higher super-linear emission slopes should be developed to further improve uSEE microscopy performance.

Similarly, donut beam scanning of upconversion nanocrystals can be applied for deep-tissue imaging with much-improved resolution (Fig. 31).[113,122] To achieve this, Yb^{3+}/Tm^{3+}-doped $NaYF_4$ nanocrystals were selected. As illustrated in Fig. 31A, upon 980-nm excitation efficient energy transfer upconversion was obtained from Tm^{3+} activators. Beyond blue emissions at 455 and 470 nm, intense NIR emission at 800 nm through two-photon upconversion was detected. These nanocrystals are highly promising for deep-tissue imaging. The emission saturation curve shows an early onset of 800-nm upconversion emissions at low power density and a sharply increasing slope, reflecting its non-linear energy transfer upconversion process (Fig. 31B). The decrease in the saturation curve under high-power excitation is due to energy being further pumped from $^3H_4$ to higher energy states. To achieve super-resolution imaging of a single nanocrystal by NIR-emission saturation (NIRES) microscopy, a donut excitation beam was selected to scan the nanocrystal sample (Fig. 31C). Upon increasing the pumping power from 0.1 to 3 MW cm^{-2}, the single-particle PSF (negative) was efficiently reduced (Fig. 31D). The penetration depth and resolution of NIRES imaging through deep tissues were further examined in a mouse liver slice (Fig. 31E). Due to the strong attenuation of visible emission, only 11% of the blue emission remains after passing through a 93-μm slice. In contrast, still nearly 40% of the 800-nm emission can be detected in confocal and NIRES microscopy imaging (Fig. 31F and G). Encouragingly, unlike STED imaging employing two laser beams, aberration distortion can be eliminated with single-beam excitation. Through 980-nm donut beam excitation, a consistent resolution of $\sim$50 nm can be maintained throughout the 93-μm liver slice (Fig. 31F and H).

In addition to the abovementioned lanthanide upconversion techniques for super-resolution imaging, upconversion nanocrystals have found applications in structured illumination microscopy with a resolution below 131 nm in the optical window.[112] However, the current challenge of upconversion nanocrystal-mediated super-resolution imaging in biological studies lies in the poor capacity for cell structure labeling using nanocrystals over 10-nm. Thus, developing bright upconversion nanocrystals with much smaller sizes (e.g., $<$ 4 nm) and a new protocol for uniform cell labeling are two urgent tasks.

5.2 Lanthanide upconversion lasing

Compared to organic dyes, quantum dots and transition metals, lanthanide ions feature complex excited states and luminescence lifetimes orders of magnitude longer. Population inversion, which is the usual prerequisite for lasing, can be easily achieved from lanthanide-activated gain materials with a much lower pumping threshold, and by tuning the doped activators, lasing output can be easily programmed from the deep UV to the NIR region. More importantly, multicolor lasing can also be realized by placing multiple or even single types of lanthanide activators in the gain medium. Miniaturized lasers are an emerging platform for generating coherent light for quantum photonics, in vivo cellular imaging, solid-state lighting, and fast 3D sensing in smartphones. Recently, lanthanide-doped upconversion nanocrystals have been utilized to achieve UV-to-NIR lasing action in stand-alone microcavities.[33,34,123] Remarkably, the pumping threshold can be reduced to the sub-100 W cm^{-2} level using a continuous wave (CW) pumping laser source at room temperature.

Lanthanide-doped upconversion materials can be easily prepared using several synthesis approaches, such as co-precipitation, thermal decomposition and hydrothermal/solvothermal methods.[124–128] Meanwhile, their size can be tuned from sub-5 nm to several micrometers. Microrods with smooth surfaces can usually be obtained using the hydrothermal method. With a refractive index of $\sim$1.45, these micro rods are suitable for working as a whispering gallery mode (WGM) lasing cavity for upconversion lasing generation in a stand-alone microcavity.

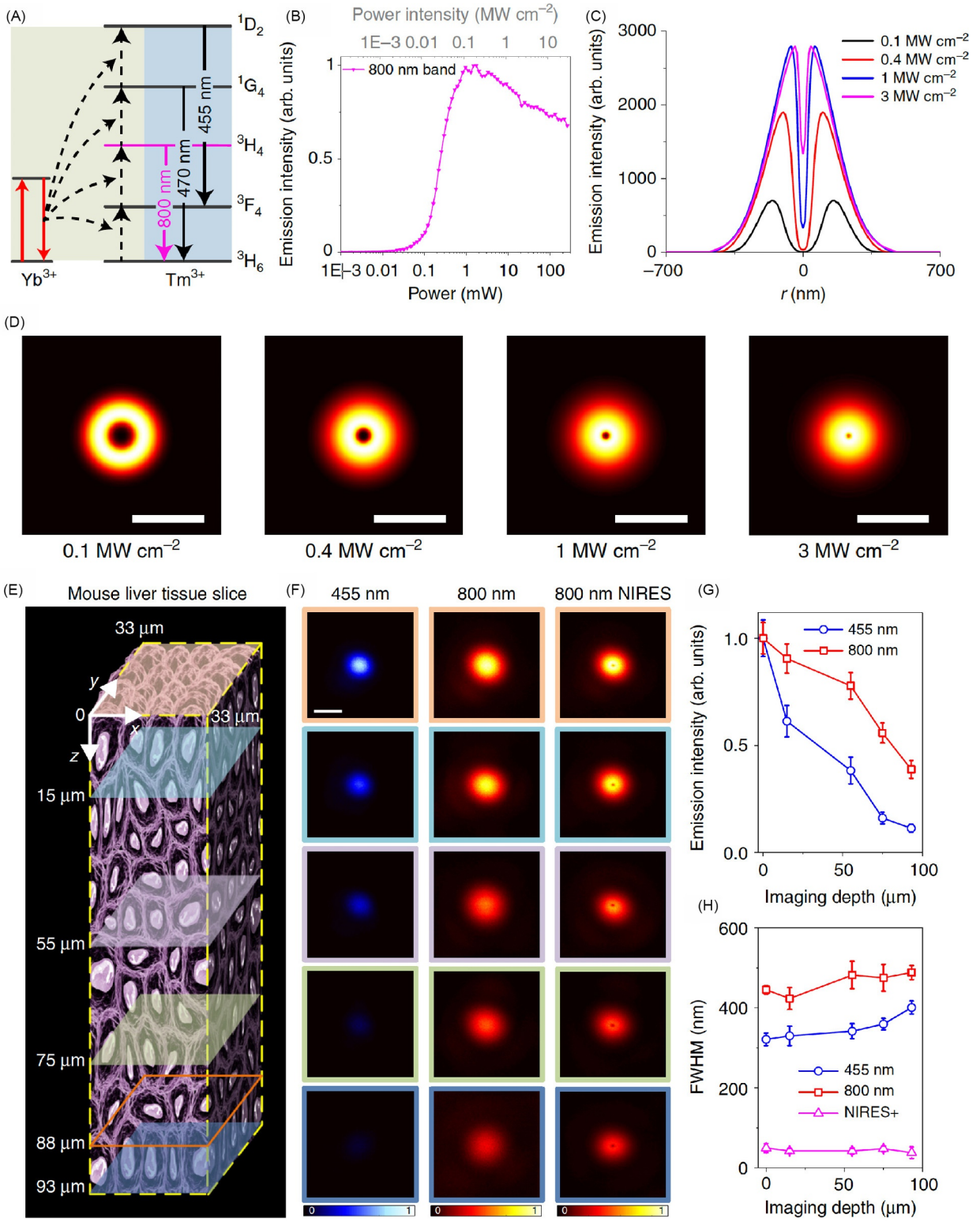

Fig. 31 (A) Energy transfer upconversion scheme of Yb/Tm-doped upconversion nanocrystals. (B) Power-dependent feature of prepared upconversion nanocrystals. (C) Point spread function of upconversion nanocrystals upon scanning with a donut beam at different power densities. (D) Corresponding PSF images from (C). (E) Illustration of the mouse liver tissue with 93-μm thickness. (F) Single-particle imaging at different depths in liver tissue. Confocal images from 455-nm emission (left); Confocal images from 800-nm emission (middle); Corresponding NIRES images (right). (G) Normalized attenuation for 455 and 800 nm emissions at different tissue depths. (H) Corresponding FWHM in (F). Printed with permission from Ref. Chen, C. et al. *Nat. Commun.* **2018**, *9*, 3290. Copyright © 2018, the authors.

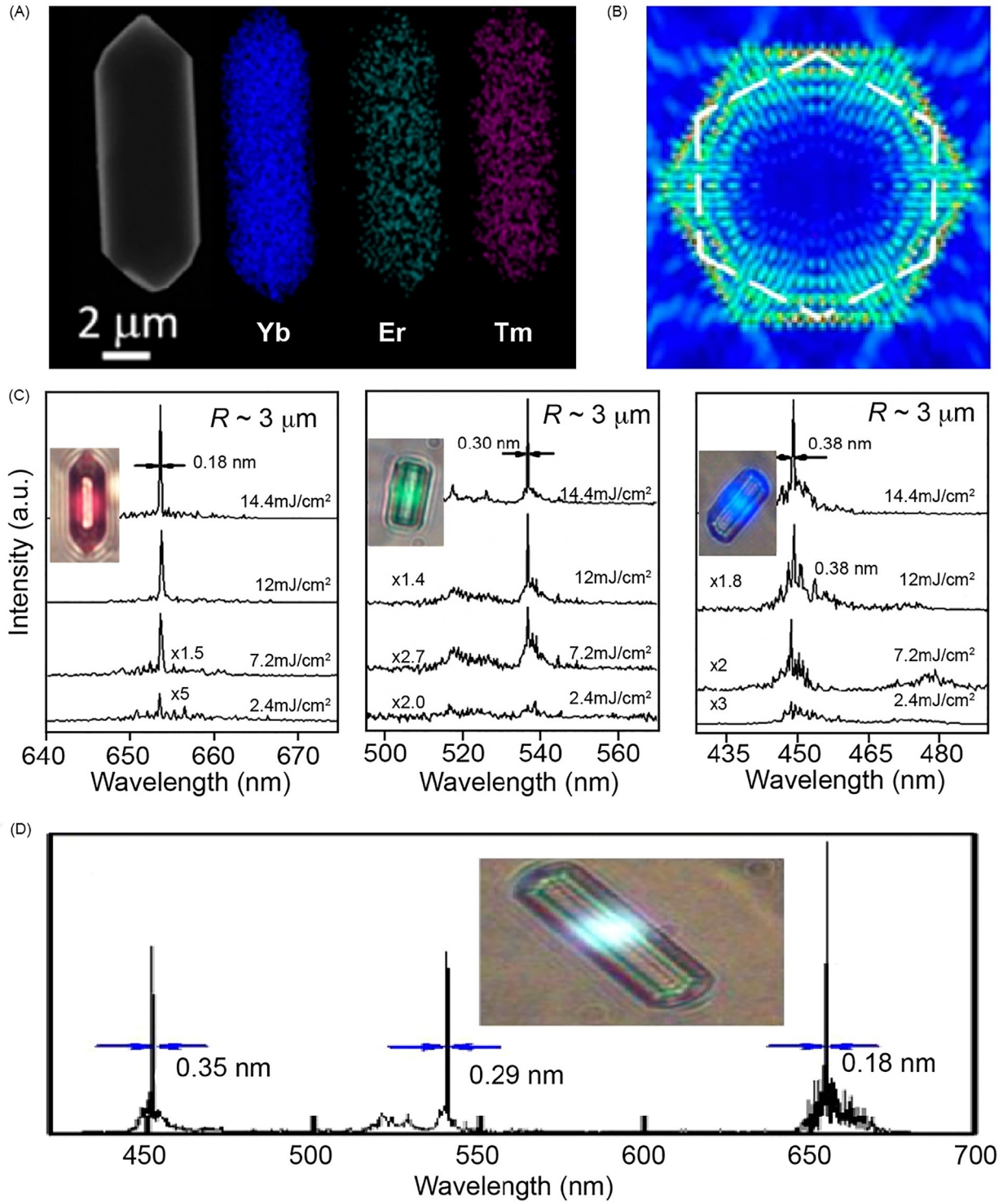

Fig. 32 (A) SEM imaging and corresponding elemental mapping of a Yb/Er/Tm-coactivated upconversion microrod. (B) Numerical simulation of the optical field distribution inside the $NaYF_4$:Yb/Er microrod. Here, the emitting wavelength of 654 nm is selected for simulation. (C) Room-temperature emission spectra of three individual 3-μm $NaYF_4$ microrods with (left) 100%Yb-1%Er, (middle) 20%Yb-1%Er, and (right) 40%–2%Tm doping concentrations upon 980-nm pulsed pumping. (D) White upconversion lasing from a single microrod codoped with 40%Yb-2%Tm-0.5%Er. Printed with permission from Ref. Wang, T. et al. *ACS Photon.* **2017**, *4*, 1539–1543. Copyright © 2017 American Chemical Society.

As shown in Fig. 32, by codoping $Yb^{3+}/Er^{3+}/Tm^{3+}$ in a $NaYF_4$ microrod that supports WGM resonance, NIR-pumped white lasing (RGB) output was realized at room temperature.[123] The SEM image of prepared $NaYF_4$ micro rods are shown in Fig. 32A. With a radius of ~3 μm, these micro rods have six flat surfaces and the ends have a hexagonal pyramid structure. Meanwhile, homogeneous doping of lanthanide sensitizers (Yb^{3+}) and activators (Er^{3+}, Tm^{3+}) can be confirmed by elemental mapping. Fig. 32B shows

the numerical investigation of the optical field profile (cross-section) of a $NaYF_4$:Yb/Er/Tm microrod at 654 nm (Er^{3+} emission). A whispering gallery mode via total internal reflection can be supported by the six flat surfaces of the microrod; thus, single microrod upconversion lasing can be expected. For $NaYF_4$ microrods codoped with Yb^{3+}/Er^{3+}(100%/1%), Yb^{3+}/Er^{3+}(20%/1%) and Yb^{3+}/Tm^{3+}(40%/2%), red (R), green (G) and blue (B) lasing can be detected under 980-nm ns-pulsed excitation, respectively (Fig. 32C). This verifies that the microrod cavity supports lasing at all these wavelengths. By codoping $Yb^{3+}/Er^{3+}/Tm^{3+}$ (40%/0.5%/2%) in a single 4-μm microrod, white lasing was achieved upon 980-nm ns-pulsed excitation at room temperature (Fig. 32D inset). The threshold of RGB microrod lasing was effectively reduced by increasing the radius of microrods. However, to maintain stable single-mode lasing, 4 μm was chosen in this work.

For lanthanide upconversion, visible light output is the most frequently studied and it is relatively easy to achieve upconversion lasing in this spectral region. As deep ultraviolet lasers are useful for environmental, health and industrial applications, fabrication of cost-effective, compact diode-pumped, solid-state deep-UV lasers using upconversion nanomaterials may revolutionize this field. In 2016, deep-UV upconversion lasing at 311 nm upon 980-nm pumping at room temperature was reported by Chen et al. (Fig. 33).[129] The energy migration upconversion mechanism is illustrated in Fig. 33A. To achieve intense deep-UV emission, Gd^{3+} ions are selected as the activators for 311-nm emission through energy migration upconversion. Upon 980-nm pumping, the incident energy is accepted by Yb^{3+} sensitizers and then transferred to Tm^{3+} activators. Subsequently, the accumulated energy on Tm^{3+} activators can be accepted by the Gd^{3+} sublattice. With a $NaYF_4$ inert shell, excitation energy can be confined in the Gd^{3+}

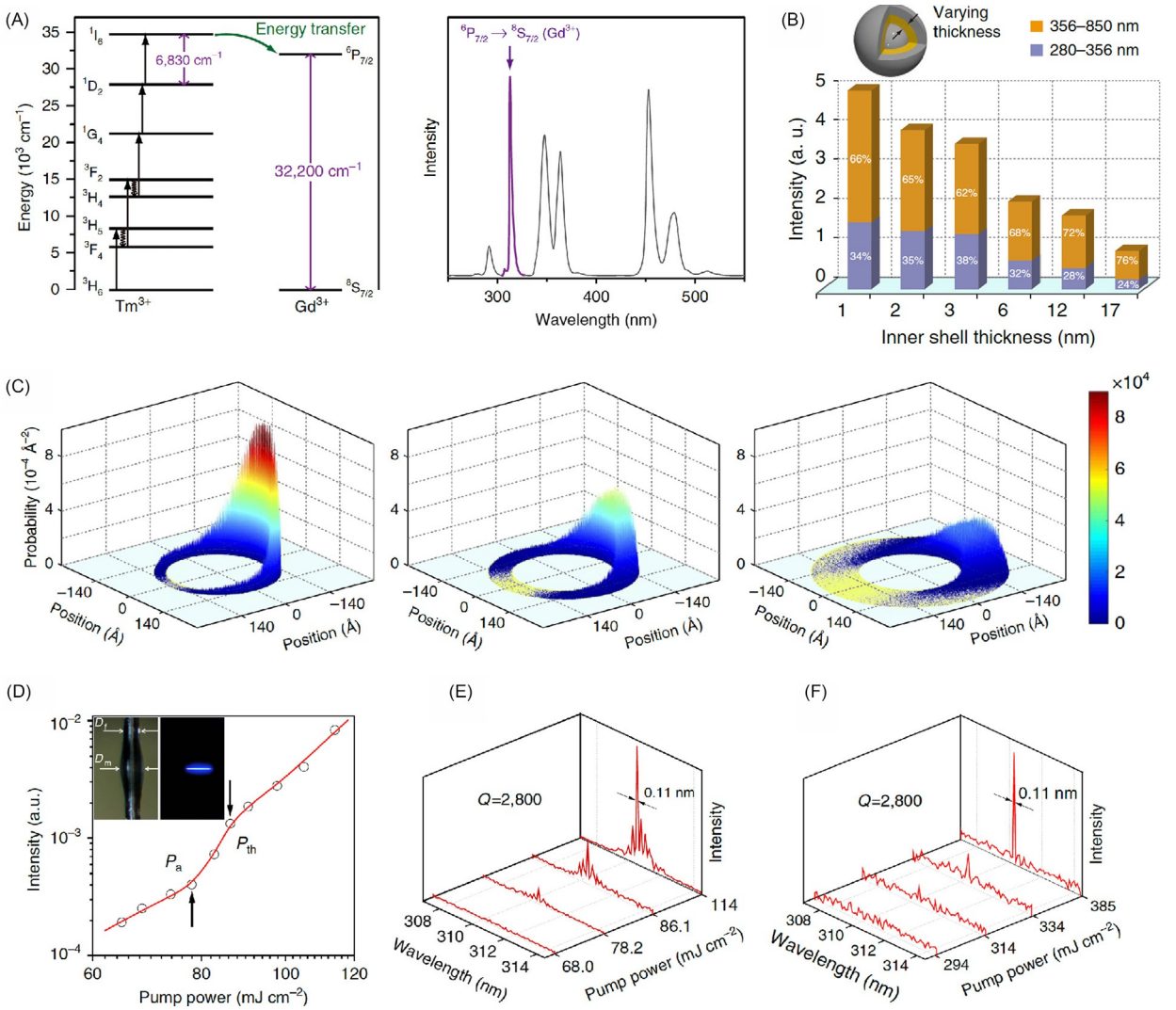

Fig. 33 (A) Energy transfer deep-UV upconversion process from Gd^{3+} and corresponded emission spectra. (B) Upconversion emission intensity versus inner shell thickness (1–17 nm). (C) The probability of finding the excitation energy on the equatorial section of core-shell-shell nanoparticles of varying inner shell thickness. With increasing inner shell thickness (from left to right panels), energy migrates to a larger area, and the probability of finding the excitation energy in the vicinity of the starting point drops significantly. (D) Logarithmic plot of output intensity versus excitation power of a microresonator with Dm = 75 μm. Inset shows the photographic image of the microresonator. (E) The corresponding lasing spectra at different excitation power. (F) Single-mode lasing spectra measured from a microresonator with Dm = 20 μm. Printed with permission from Ref. Chen, X. et al. *Nat. Commun.* **2016**, *7*, 10304. Copyright © 2016, the authors.

sublattice to support intense deep-UV emission at 311 nm. Although deep-UV upconversion emission around 290 nm can be obtained from Tm^{3+}-activated $NaYF_4$ nanocrystals, its intensity is much lower than that through Gd^{3+} migration. Moreover, the luminescence lifetime of the excited energy levels for Tm^{3+} (290 nm, 0.3 ms) is much shorter than that from Gd^{3+} (310 nm, 4.07 ms). Considering the requirement of high-quality population inversion for lasing, Gd^{3+} instead of Tm^{3+} was selected for deep-UV upconversion lasing. $NaYF_4$@$NaYbF_4$:Tm/Gd(1/30%)@$NaYF_4$ nanocrystals were prepared for lasing (Fig. 33B). With a thinner inner shell, energy loss to the host lattice can be effectively suppressed, as evidenced by the significantly prolonged luminescence lifetime of Yb^{3+} sensitizers and the gradually increased ratio of five-photon upconversion emission to whole emission spectra. The probability distribution function of the excitation energy as a function of space within the Yb shell has also been simulated, assuming that the excitation energy hops randomly in the inner shell layer (Fig. 33C). The simulation results show that the probability of finding the excitation energy in a thin Yb shell can be much higher than that in a thicker one, validating favorable energy transfer from Yb^{3+} to adjacent Tm^{3+} activators.

A drop of silica resin containing upconversion nanocrystals was coated onto a standard optical fiber to fabricate a bottle-like micro resonator laser cavity (Fig. 33D inset). Upon pulsed 980-nm excitation, upconversion emission exhibits a well-defined, S-like nonlinear power dependence, suggesting the occurrence of amplified spontaneous emission and lasing (Fig. 33D). Fig. 33E shows the corresponding emission spectra upon different pumping powers. At low pump power, a broad spontaneous emission band is observed. As the excitation power increases slightly above P_a, a sharp peak can be detected. By further increasing the excitation power above P_{th}, well-defined sharp peaks with a linewidth <0.11 nm emerge. Using a smaller resonator ($D = 20$ μm), single-mode lasing can be realized, but with a higher pumping threshold (Fig. 33F).

Although an upconversion micro resonator laser can be achieved at room temperature, the above-mentioned approaches are based on a pulsed pumping laser. To realize lasing upon continuous-wave excitation, working at low-temperature is usually required to combat the heat-induced increases in lasing thresholds. Moreover, CW laser-pumped upconversion lasing can be obtained by selecting a microresonator that weakly absorbs the pumping laser and has a high gain-to-loss ratio. More importantly, upconversion nanocrystals with long excited-state lifetimes and high-quality population inversion can also contribute to CW lasing.

In 2018, a room-temperature CW microlaser, based on a combination of polystyrene microspheres as the WGM microresonators and Tm^{3+}-doped energy-looping nanoparticles (ELNPs) as the gain media, was reported (Fig. 34).[33] For preparation of WGM microresonators, ELNPs were coated to the surfaces of polystyrene microspheres with a 5-μm diameter. SEM and cross-sectional TEM images of prepared microresonators reveal that a 100-nm thick shell of ELNPs is uniformly coated to resonator surfaces (Fig. 34A). Fig. 34B illustrates energy transfer and emission mechanisms of ELNPs used for upconversion lasing. Upon 1064-nm laser pumping (step 1), Tm^{3+} activators can be populated to the $^3F_4$ state and subsequently the $^3F_{2,3}$ state. Energy looping could be triggered by cross-relaxation, enabling a fraction of excitation energy from a highly excited Tm^{3+} ion to be transferred to a neighboring Tm^{3+} ion in its ground state. This process results in two Tm^{3+} ions in the same intermediate excited state (step 3). In such a way, the looping process doubles the population of an excited state, thereby populating excited states nonlinearly. Ultimately, a population inversion in the $^3H_4$ state triggers the 800-nm emission (step 4). With a strong population inversion, low-threshold CW lasing at room temperature can be expected. Fig. 34C and D show the experimentally obtained and simulated WGM spatial distribution in a 5 μm polystyrene bead, respectively. The good match between the experimental lasing spectra and simulated optical modes are shown in Fig. 34E, and high Q-factors about 10^3–10^4 for these ELNP-coated microresonators can be calculated.

Upon CW 1064-nm laser pumping, lasing was observed from these ELNP microresonators (Fig. 34F). When the pumping power was below the lasing threshold (17 kW cm^{-2}), a broad upconversion emission band was detected. With increased pumping above the threshold, a primary lasing mode at around 807 nm emerged with narrowed bandwidth and increased intensity. The low lasing threshold obtained can be attributed to the high Q-value of the microresonator and the strong population inversion of the $NaYF_4$:Tm^{3+} gain medium.

Interestingly, an application for these stand-alone microlasers in biological media has been demonstrated. After immersing these microresonators in fetal bovine serum (FBS), NIR microcavity emission spectra exhibit an in situ CW lasing threshold of about 250 kW cm^{-2} (Fig. 34G). The lasing threshold can be further reduced by selecting microresonators with a higher refractive index. The spectral shift of lasing modes can be an effective signature for sensing the changes, such as local index, temperature, and pressure in the environment. More importantly, these microlasers are stable over several hours of continuous excitation at high power (300 kW cm^{-2}) and show promising applications for subcellular imaging, tracing, and probing.

In 2019, room-temperature CW upconversion microlasers with a greatly reduced threshold (70 W cm^{-2}) were achieved using plasmon nanocavities (Fig. 35).[34] A plasmonic array consisting of Ag nanopillars (80-nm diameter, 50-nm height) arranged in a square lattice with a 450-nm periodicity was fabricated as the resonator (Fig. 35A). A solution of $NaYF_4$:Yb/Er nanoparticles was drop-cast onto the Ag array to form a 150-nm thick film. After nanoparticle coating, a resonance band of the fabricated nanocavity was measured around 660 nm, which overlapped the upconversion emission band of Er^{3+} activators. Fig. 35B shows the simulated electric field intensity profile at 664 nm. The simulation result indicates that the near-field enhancement ($|E|^2/|E_0|^2$) around the nanopillars can be higher than 1000-fold. With strong plasmonic coupling, upconversion lasing around 660 nm can be successfully observed with a record low threshold of 70 W cm^{-2}. Fig. 35C shows the upconversion emission spectra as a function of pumping power at 980 nm. Upon increasing the pumping power above the threshold, a significant increase in the rising slope of the input-output curve and simultaneous linewidth narrowing of the lasing mode to <1 nm can be measured. Apart from low thresholds, Ag plasmonic array nanocavities offer directional coupling, in contrast to the aforementioned spherical WGMs, in which input coupling is nontrivial and emission is less directional. According to Fig. 35D, upon 980 nm laser excitation, beam-like

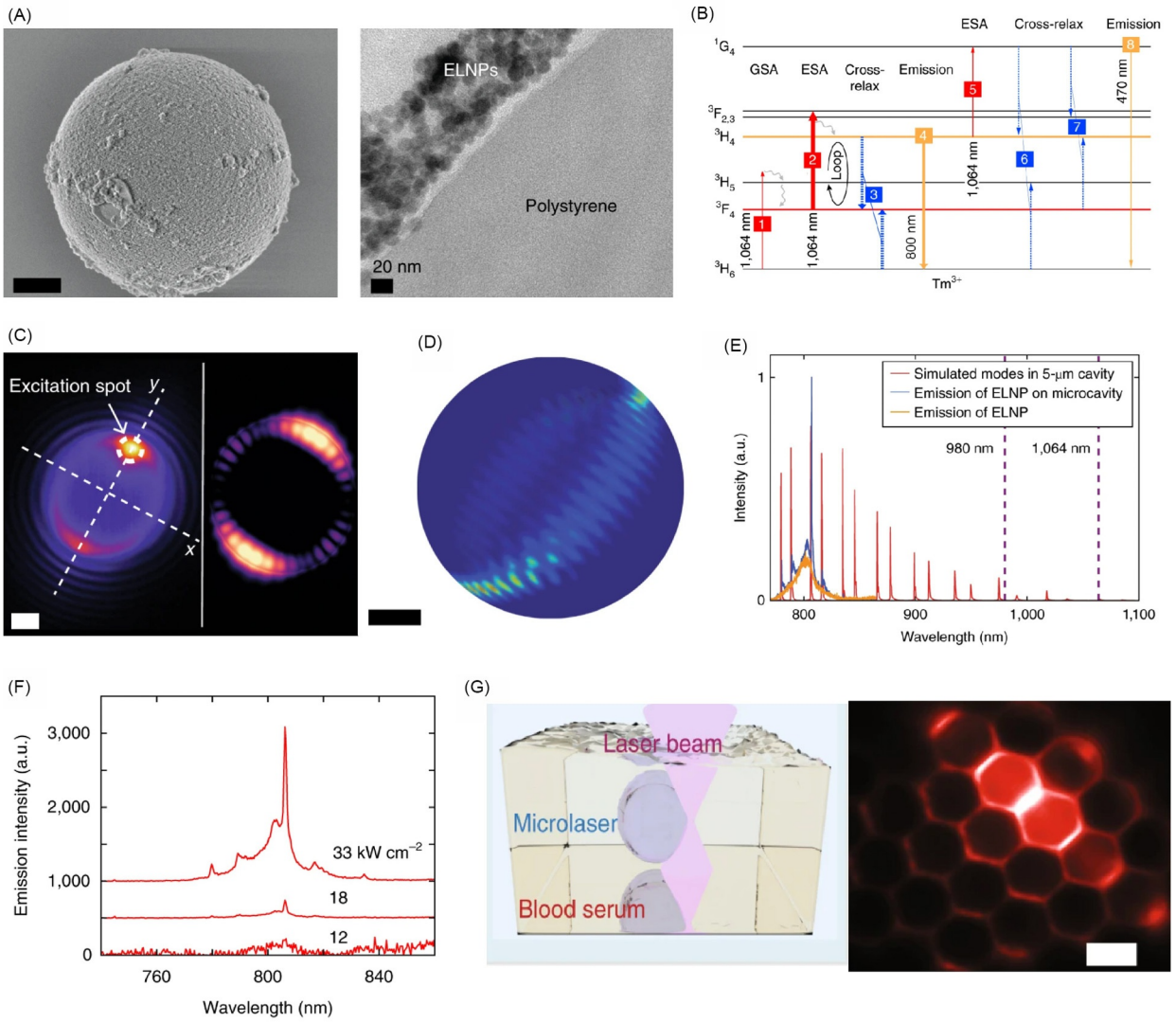

Fig. 34 (A) SEM and cross-section TEM images of a polystyrene bead coated with upconversion nanocrystals. (B) Upconversion looping mechanism in Tm^{3+}-doped $NaYF_4$. (C) Wide-field image of a lasing microsphere. (D) Numerical simulation of electric field intensity for the transverse magnetic WGM at 807 nm around a dielectric sphere. (E) Experimental emission spectra of upconversion nanocrystals and simulated NIR spectra of WGM supported by a 5-μm polystyrene microsphere. (F) NIR emission spectra of Tm^{3+}-doped $NaYF_4$ nanocrystals with pump intensity below, near, and above the lasing threshold. (G) Schematic and wide-field image of the microlaser operation in blood serum. Printed with permission from Ref. Fernandez-Bravo, A. et al. *Nat. Nanotechnol.* **2018**, *13*, 572–577.

upconversion lasing with a low divergence angle of 0.5° was obtained. Moreover, the output lasing beam was polarized in the same direction as the incident pump and the all-solid-state system can work at room temperature for more than 6 h under continuous pumping. Therefore, this plasmonic upconversion nanolaser platform offers prospects to realize lab-on-a-chip quantum-optical technologies.

To date, lanthanide upconversion micro-nanolasers working at room temperature with an ultra-low threshold have been realized. This technology will find applications in nanophotonics, biophotonics, and even quantum optics.

5.3 Upconversion optogenetics

Membrane ion channels are responsible for propagation and integration of electrical signals in the muscular, nervous, and many other systems. Recently, one technology termed "optogenetics," has been utilized for manipulation of neural activities optically with high specificity and millisecond-timescale resolution. Despite remarkable achievements, currently established optogenetic tools are mainly confined to the visible window (Fig. 36A), which significantly limits in vivo applications due to the high attenuation of visible light in biological tissues.[40,130–134]

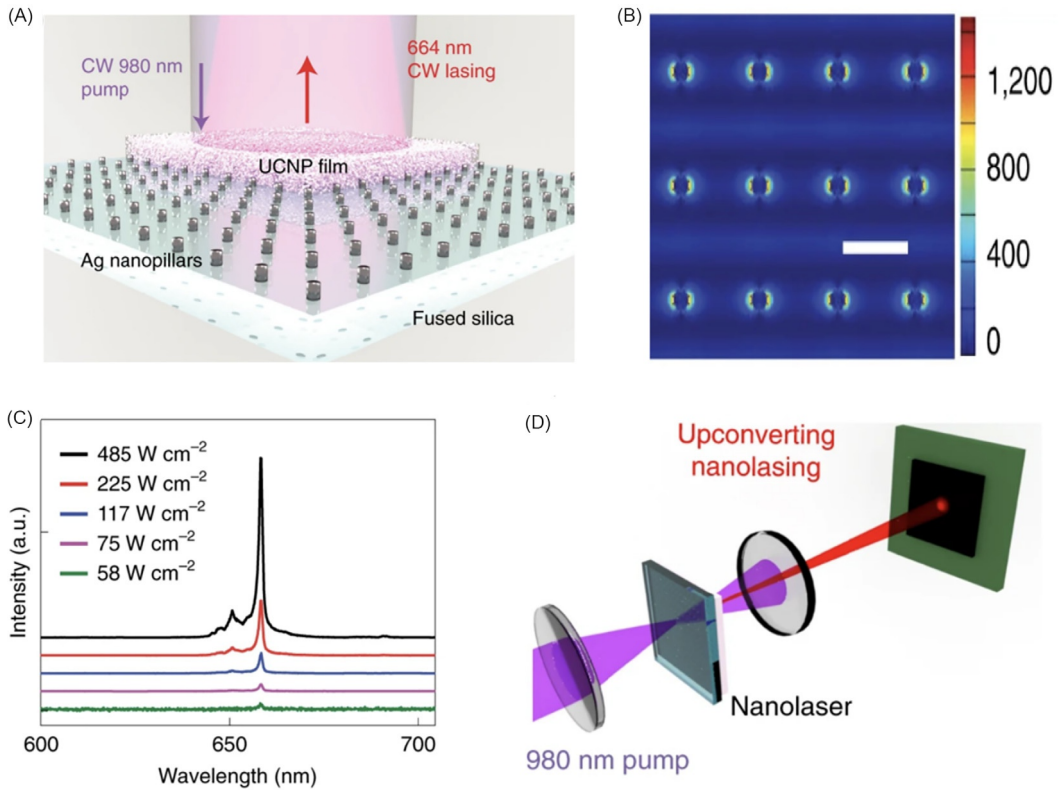

Fig. 35 (A) Schematic showing upconversion nanocrystal coating onto an array of Ag nanopillars. (B) FDTD simulation of the $|E|^2$ plot for the Ag nanopillar array at resonance. (C) Power-dependent lasing spectra of Yb/Er-doped $NaYF_4$ nanocrystals placed on top of Ag nanopillars that resonate at 664 nm. (D) Schematic of the experimental setup used to measure the far-field beam profile of the upconversion laser. Printed with permission from Ref. Fernandez-Bravo, A. et al. *Nat. Mater.* **2019**, *18*, 1172–1176. Copyright © 2019, Nature publication group.

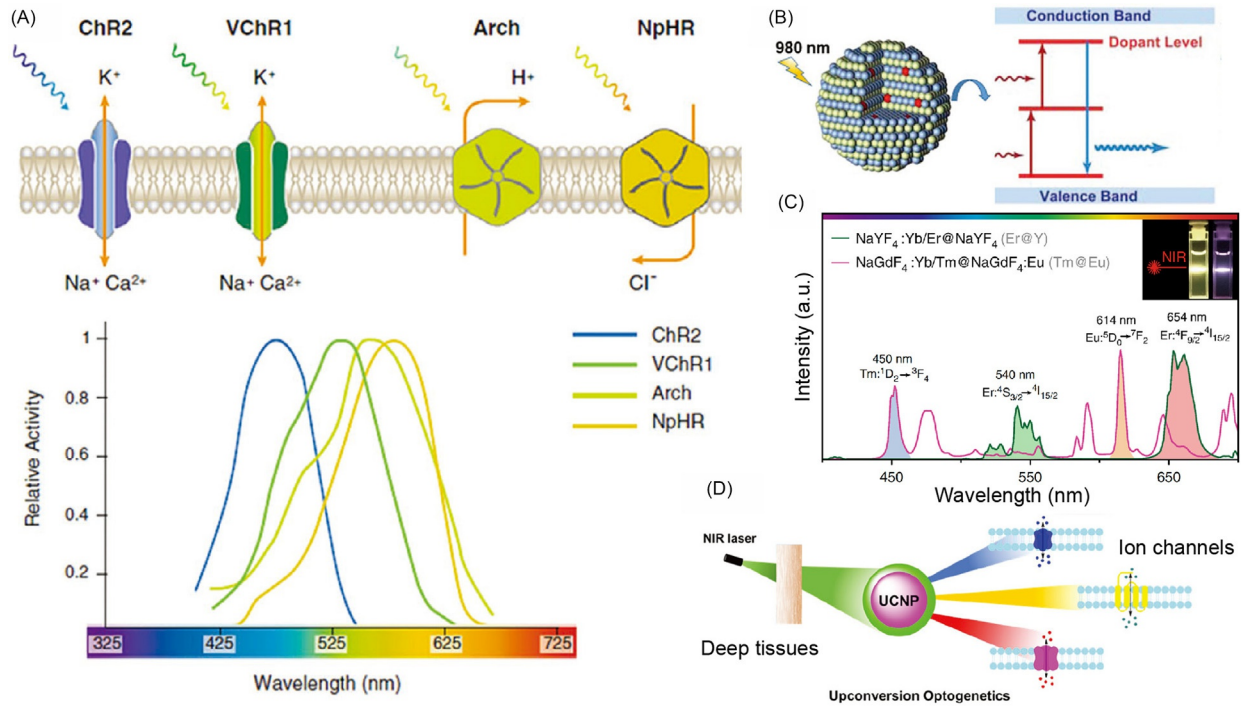

Fig. 36 (A) Optogenetic tools for membrane ion channel manipulation and working spectra of commonly selected light-sensitive channelrhodopsins and proteins. (B) Schematic illustration of the structure and working mechanism of lanthanide-doped upconversion nanocrystals. (C) Photographic images and upconversion luminescence from different lanthanide-activated upconversion nanocrystals dispersed in cyclohexane upon 980-nm NIR excitation. (D) Illustration of selective activation of channelrhodopsins and light-sensitive proteins by designing upconversion nanocrystals with strong emission in a certain spectral range. (A, B, D) Printed with permission from Ref. Wang, Z.; Hu, M.; Ai, X.; Zhang, Z.; Xing, B. *Adv. Biosyst.* **2019**, *3*, 1800233. Copyright © 2018 WILEY-VCH Verlag GmbH & Co. KGaA, Weinheim. (C) Printed with permission from Ref. Liang, L. et al. *Nat. Commun.* **2019**, *10*, 1391. Copyright © 2019, the authors.

Upconversion nanocrystals have long been applied to deep-tissue imaging due to their high brightness in the UV-Vis-NIR region upon excitation with NIR light, which features reduced tissue attenuation (Fig. 36B).[135–140] Furthermore, upconversion emission bands can be designed to overlap with targeted channelrhodopsins (ChRs) or other light-sensitive proteins (Fig. 36C).[45] Therefore, in recent years, upconversion nanocrystals have also been developed as emerging nano-illuminators to selectively control the activity of specific membrane ion channels in order to study physiological and pathophysiological processes[39,41,44,141–143] (Fig. 36D).

Upconversion nanocrystal-mediated optogenetics at the single-cell level has been demonstrated by many research groups. For example, by embedding upconversion nanocrystals with strong blue emission into polymeric scaffolds, optogenetic control of activities of neuron cells located on the scaffold surface has been successfully realized upon 980-nm NIR excitation (Fig. 37).[43] First, a polymeric upconversion nanocrystal hybrid scaffold was fabricated by spin-coating a solution containing upconversion nanocrystals onto a substrate (Fig. 37A). Channelrhodopsin-2 (CHR2) is one microbial ion channel that conducts cation influx upon blue light illumination (450–475 nm). Thus, $NaYF_4$:Yb/Tm@$NaYF_4$ core-shell nanocrystals were selected to trigger the ChR2. As shown in Fig. 37B, upon 980-nm excitation, strong blue upconversion luminescence around 475 nm was observed from the hybrid scaffold. To study NIR-triggered optogenetics, hippocampal neurons were cultured on the surface of the prepared hybrid scaffold and their activities were investigated upon 980-nm photoexcitation (Fig. 37C). The SEM image in Fig. 37D clearly shows the success of culturing neurons on the polymer scaffold and the high loading of upconversion nanocrystals in the scaffold. In current-clamp recording mode, nerve impulse generation was checked by applying brief pulses of light to neurons (Fig. 37E). It can be seen that both blue and NIR excitation can elicit nerve impulses. Importantly, impulses elicited by NIR light are comparable to those elicited with 470-nm blue light, implying that blue upconversion emission is strong enough to activate ChR2 and drive neuronal depolarization beyond the nerve impulse firing threshold. Moreover, time-locked and sustained trains of impulses can also be generated upon 980-nm illumination of ChR2-expressing neurons on the polymeric scaffold (Fig. 37F). Therefore, this work provides an excellent demonstration of rationally designed upconversion-mediated optogenetics for advanced neural applications.

Beyond working at the single-cell level, in 2016, in vivo control of the movement of ChR2- expressing nematodes with NIR optogenetics was also demonstrated (Fig. 38).[44] In that study, to activate ChR2 expression in worms, silica-coated $NaYF_4$:Yb/Tm nanocrystals with strong blue emission were prepared and consumed by worms. With ChR2 expression in neurons, illumination with blue light to activate ChR2 was interpreted as "touch," resulting in an aversive response. Thus, a forward worm movement should be observed upon NIR excitation, once upconversion optogenetics is at work.

As shown in Fig. 38A, without nanocrystal uptake, the movement of worms is not disturbed by 980-nm stimulation. But the opposite behavior could be observed when UCNPs are introduced (Fig. 38B). With a greater consumption of upconversion nanocrystals, a higher probability of triggering opposite behavior of worms expressing ChR2 can be observed (Fig. 38C). Control experiments confirm that blue upconversion emission induced by NIR excitation is required for ChR2 activation (Fig. 38D). The opposite response of a worm that consumed upconversion nanocrystals was immediately observed once NIR stimulation was applied (Fig. 38E), indicating the effectiveness of upconversion-mediated in vivo optogenetics.

Similarly, in vivo upconversion optogenetics in zebrafish have also been demonstrated upon 808-nm NIR stimulation (Fig. 39).[46] Upconversion nanocrystals sensitized with Yb^{3+} ions are usually stimulated using a 980-nm laser. However, the 980-nm excitation beam can be severely attenuated by biological tissues through scattering and absorption. To achieve deeper penetration and less overheating, Nd^{3+}-sensitized upconversion nanocrystals can be selected with greatly mitigated attenuation at 800 nm. In that work, $NaYF_4$:Yb/Tm/Nd@$NaYF_4$:Nd nanocrystals were prepared to generate blue (Tm^{3+}) upconversion luminescence upon 808-nm excitation. Fig. 39A shows the protocol of metabolic labeling for site-specific covalent localization of NIR-responsive nanocrystals on cell membranes to achieve precise regulation of ion channel function. By simply feeding the Ac_4ManNaz precursor, N_3-tagged glycans were introduced to human embryonic kidney 293 (HEK293) cells. A DBCO-conjugated fluorophore, working as a biorthogonal linkage, triggered a copper-free click reaction in Ac_4ManNAz-treated HEK293 cells (Fig. 39B). After surface modification of Nd-sensitized nanocrystals with polyacrylic acid (PAA), these nanocrystals were covalently anchored on the membrane through DBCO coupling. To accept blue upconversion emission, ChR2 was engineered on cell surfaces to mediate the influx of essential signaling ions in the cytoplasm (Fig. 39B).

To regulate membrane channel activities in vivo in zebrafish using 808-nm light, a Ca^{2+} indicator (Rhod-3 AM) was used to monitor the cation influx in zebrafish. As shown in Fig. 39C, upon 808-nm illumination for 2 h, strong fluorescence can be recorded from zebrafish treated with DBCO/Cy5.5-upconversion nanocrystals. However, no distinguishable change in fluorescence can be found from zebrafish without NIR illumination. Notably, this long-term experiment cannot be performed under 980-nm irradiation due to the limitation of severe overheating.

In another step forward in 2018, deep-brain neuron stimulation using upconversion nanocrystal-mediated optogenetics in mouse brain was reported (Fig. 40).[39] Upconversion nanocrystal-mediated NIR optogenetics evoked dopamine release from genetically tagged neurons and induced brain oscillations through activation of inhibitory neurons. Such upconversion optogenetics also silenced seizure by inhibition of hippocampal excitatory cells and triggered memory recall.

In a typical experiment, an adeno-associated virus (AAV) encoding ChR2-EYFP (enhanced yellow fluorescent protein) was injected into ventral tegmental area (VTA) of tyrosine hydroxylase-driven Cre recombinase transgenic mice to achieve Cre-dependent expression of ChR2 in dopamine neurons Subsequently, blue-emitting $NaYF_4$:Yb/Tm@$NaYF_4$@SiO_2 nanocrystals were injected into the VTA (Fig. 40A and B). Upon 980-nm excitation, photocurrents and evoked spikes in VTA DA neurons were

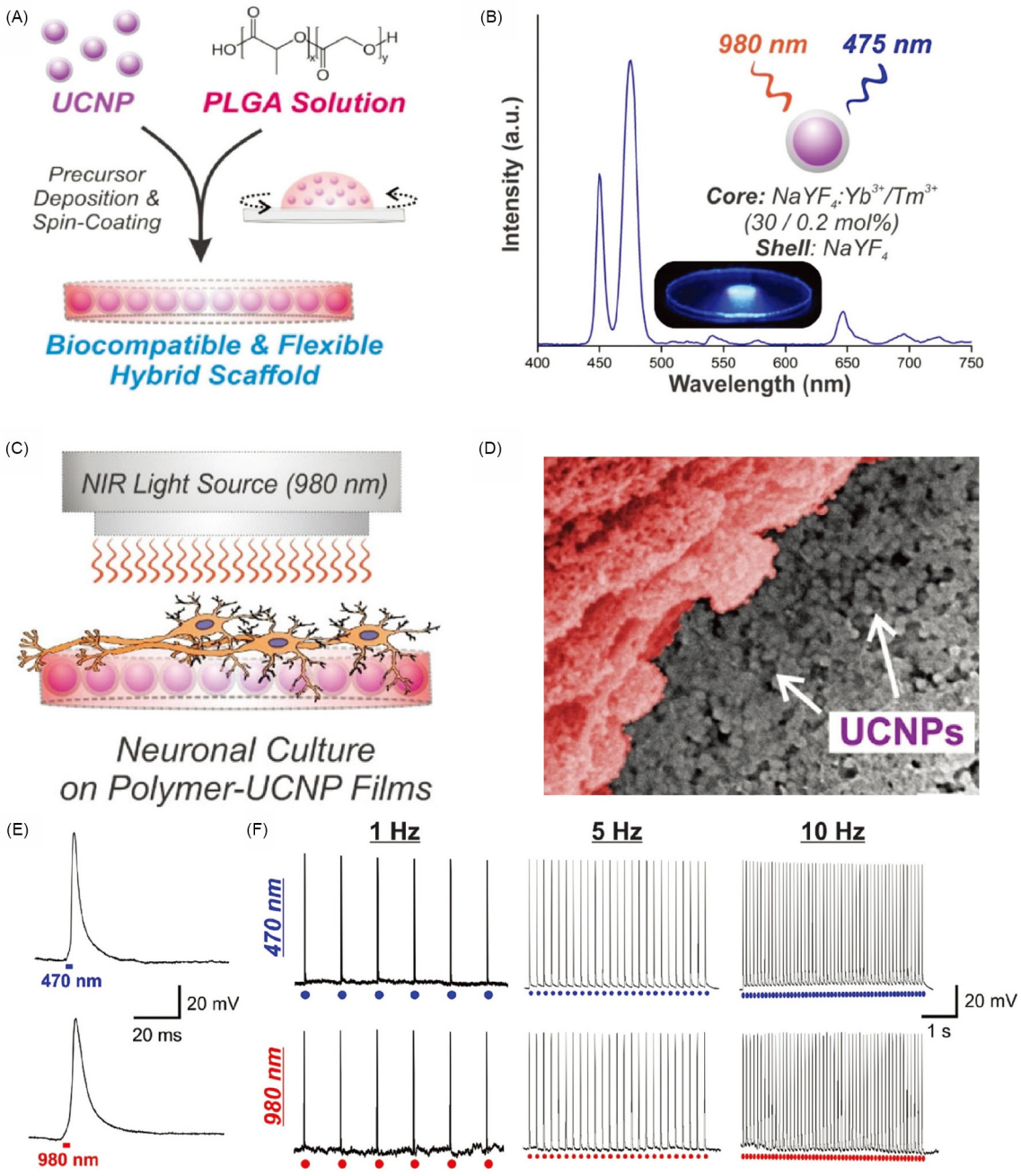

Fig. 37 (A) Experimental processes of embedding blue-emitting upconversion nanocrystals into a cell-supporting polymeric scaffold. (B) Photoluminescence spectrum of Yb^{3+}/Tm^{3+}-doped $NaYF_4$ nanocrystals upon 980-nm excitation. Inset is a photographic image of the hybrid scaffold upon 980-nm excitation. (C) Schematic application of the upconversion nanocrystal-embedded polymeric scaffold for optogenetic neuronal activation. (D) SEM imaging of the distribution of a hippocampal neuron cell cultured on the surface of the hybrid scaffold. (E) Membrane action potentials induced by blue (470 nm, top panel) and NIR light (980 nm, bottom panel), respectively. (F) Traces showing repetitive action potentials in a current-clamped hippocampal neuron evoked by 1-, 5-, and 10-Hz train of light pulses from blue (top row) and NIR light (bottom row). Printed with permission from Ref. Shah, S. et al. *Nanoscale* **2015**, *7*, 16571–16577. Copyright © 2015 Royal Society of Chemistry.

detected, indicating successful triggering of membrane depolarization (Fig. 40C and D). Notably, multiple spikes were elicited by trains of NIR illumination at 10 to 50 Hz, showing no significant dependence on excitation frequency (Fig. 40E).

Furthermore, in vivo utility of NIR optogenetics was tested through viral delivery of ChR2, followed by upconversion nanocrystal injection in TH-Cre mice with TA DA neurons sensitized to transcranial NIR stimulation (Fig. 40F). Phasic spike activity of VTA DA neurons was reflected by striatal DA transients. As shown in Fig. 40G, a 2-s NIR stimulation can trigger striatal DA release lasting for more than 15 s while no significant DA release can be detected in control mice without NIR stimulation and nanoparticle injection, or ChR2 expression.

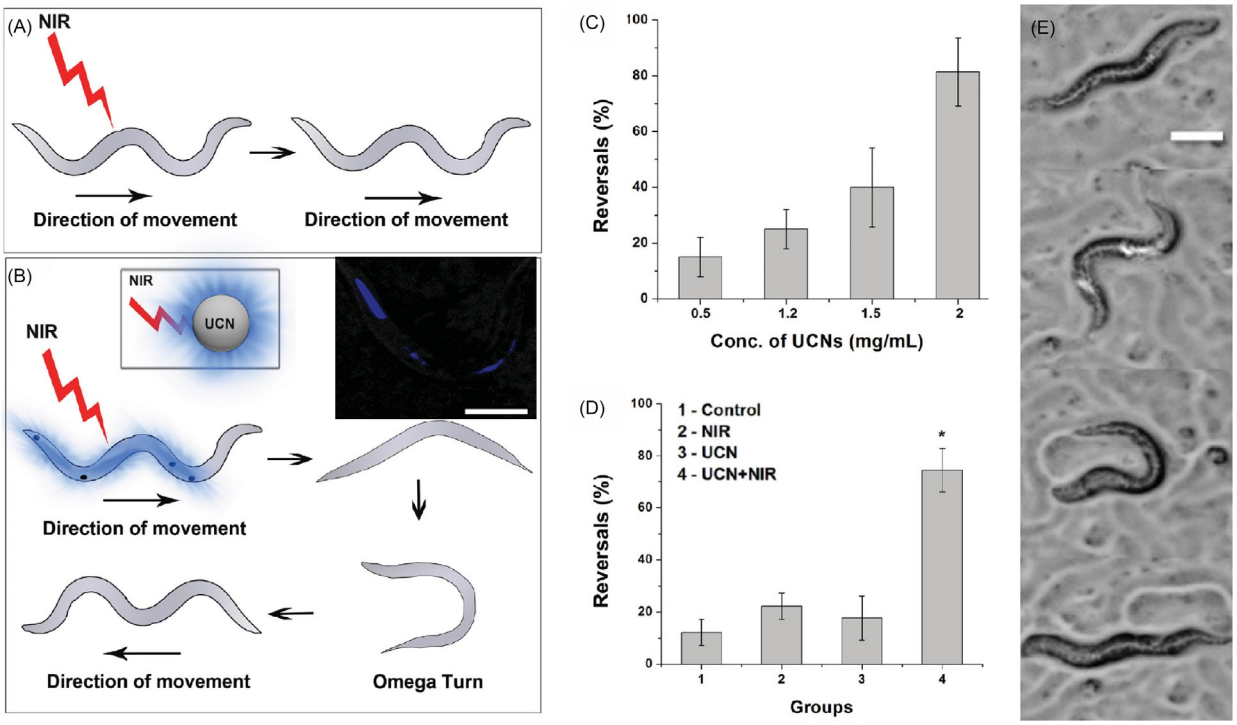

Fig. 38 Schematic showing differences in movement behavior in worms when exposed to NIR light with (A) and without (B) the presence of blue-emitting upconversion nanocrystals. (C) Effect of the upconversion nanocrystal concentration on the percentage of worms showing reversal phenotype upon NIR illumination. (D) Percentage of worms showing reversal phenotype upon different incubation and excitation situations. (E) Images showing NIR -induced reversal phenotype of worms with upconversion nanocrystals. Printed with permission from Ref. Bansal, A.; Liu, H.; Jayakumar, M. K. G.; Andersson-Engels, S.; Zhang, Y. *Small* **2016**, *12*, 1732–1743. Copyright © 2016 WILEY-VCH Verlag GmbH & Co. KGaA, Weinheim.

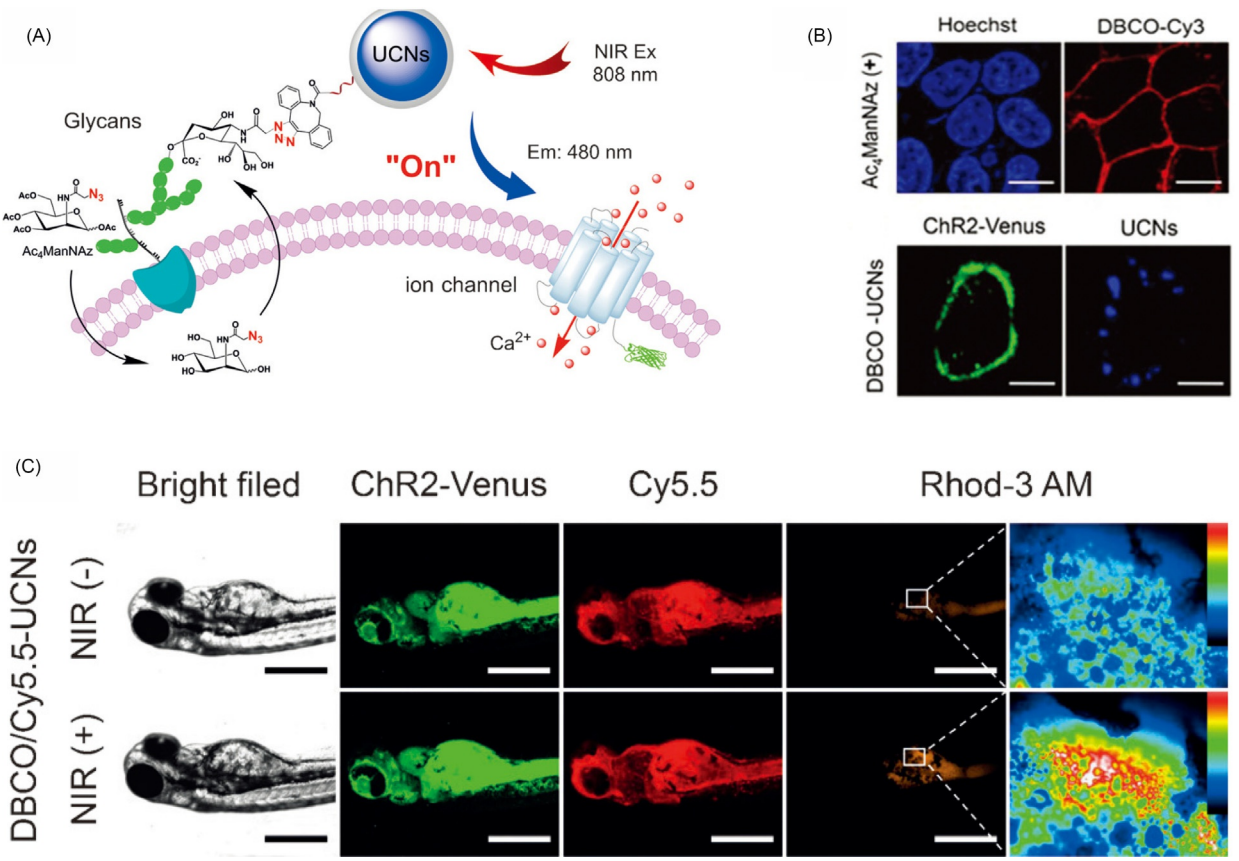

Fig. 39 (A) Labeling strategy for site-specific localization of upconversion nanocrystals on cell membranes for precise optogenetic modulation. (B) Imaging of membrane localization of upconversion nanocrystals through glycan metabolic strategy. (C) In vivo optogenetic activation of ChR2 in zebrafish. Printed with permission from Ref. Ai, X. et al. *Angew. Chem. Int. Ed.* **2017**, *56*, 3031–3035. Copyright © 2017 WILEY-VCH Verlag GmbH & Co. KGaA, Weinheim.

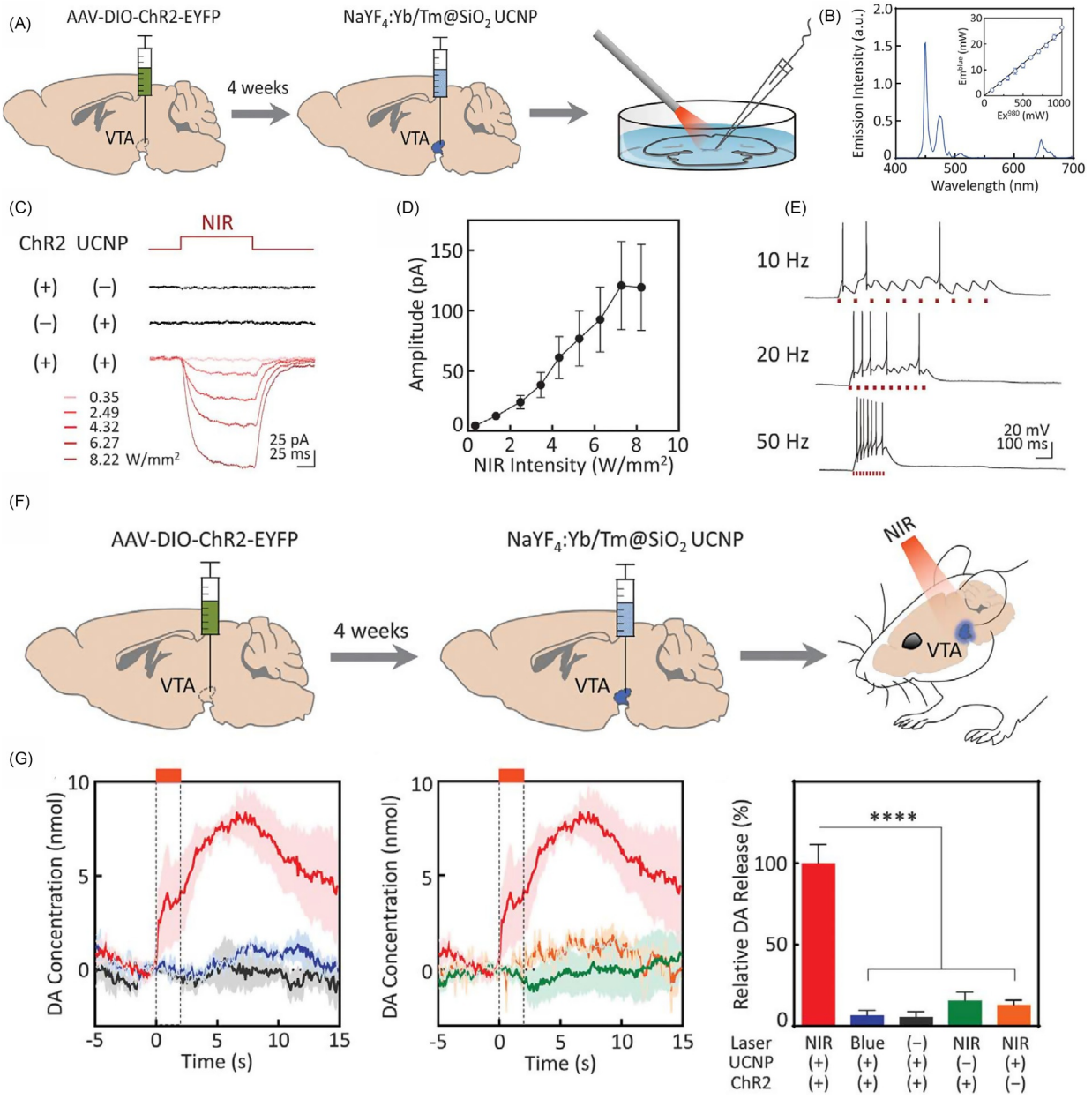

Fig. 40 (A) AAV-DIO-ChR2-EYFP was injected into the VTA of TH-Cre transgenic mice for Cre-dependent expression of ChR2 in DA neurons. (B) Upconversion emission spectra of $NaYF_4$:Yb/Tm@SiO_2 nanocrystals upon 980-nm excitation. Inset shows the upconversion emission intensity of upconversion nanocrystals as a function of excitation power density at 980 nm. (C) Voltage-clamp traces of neurons from VTA slice in response to NIR stimulation at various intensities. (D) Photocurrent amplitude as a function of NIR stimulation intensity. (E) Current-clamp traces of ChR2-expressing DA neurons in response to NIR pulses at different frequencies. (F) In vivo transcranial NIR stimulation of the VTA in anesthetized mice. (G) Transient DA concentrations in the ventral striatum in response to transcranial VTA stimulation under different conditions and corresponding cumulative DA release after the start of transcranial stimulation. Printed with permission from Ref. Chen, S. et al. *Science* **2018**, *359*, 679–684. Copyright © 2018 American Association for the Advancement of Science.

Upconversion nanocrystals embedded in implantable microdevices (e.g., glass microneedles and flexible PEGDA waveguides) for remote in vivo optogenetic control of neuronal functions have also been reported. Although implantation of millimeter-sized devices in the mouse brain is relatively invasive, stimulation efficiency can be remarkably improved, benefiting from high nanoparticle loading in these microdevices and the waveguiding of the stimulating light.

An exciting demonstration of upconversion nanocrystals for night vision in an animal model was reported in 2019 (Fig. 41).[144] Upon surface conjugation of concanavalin A protein (ConA), green-emitting $NaYF_4$:Yb/Er@$NaYF_4$ nanocrystals bind to glycoproteins on the outer photoreceptor segment (Fig. 41A). After injection into the subretinal space, surface-modified nanocrystals remain tightly bound to the inner and outer segments of both rods and cones (Fig. 41B–D). Therefore, a layer of nanoantennae capable of

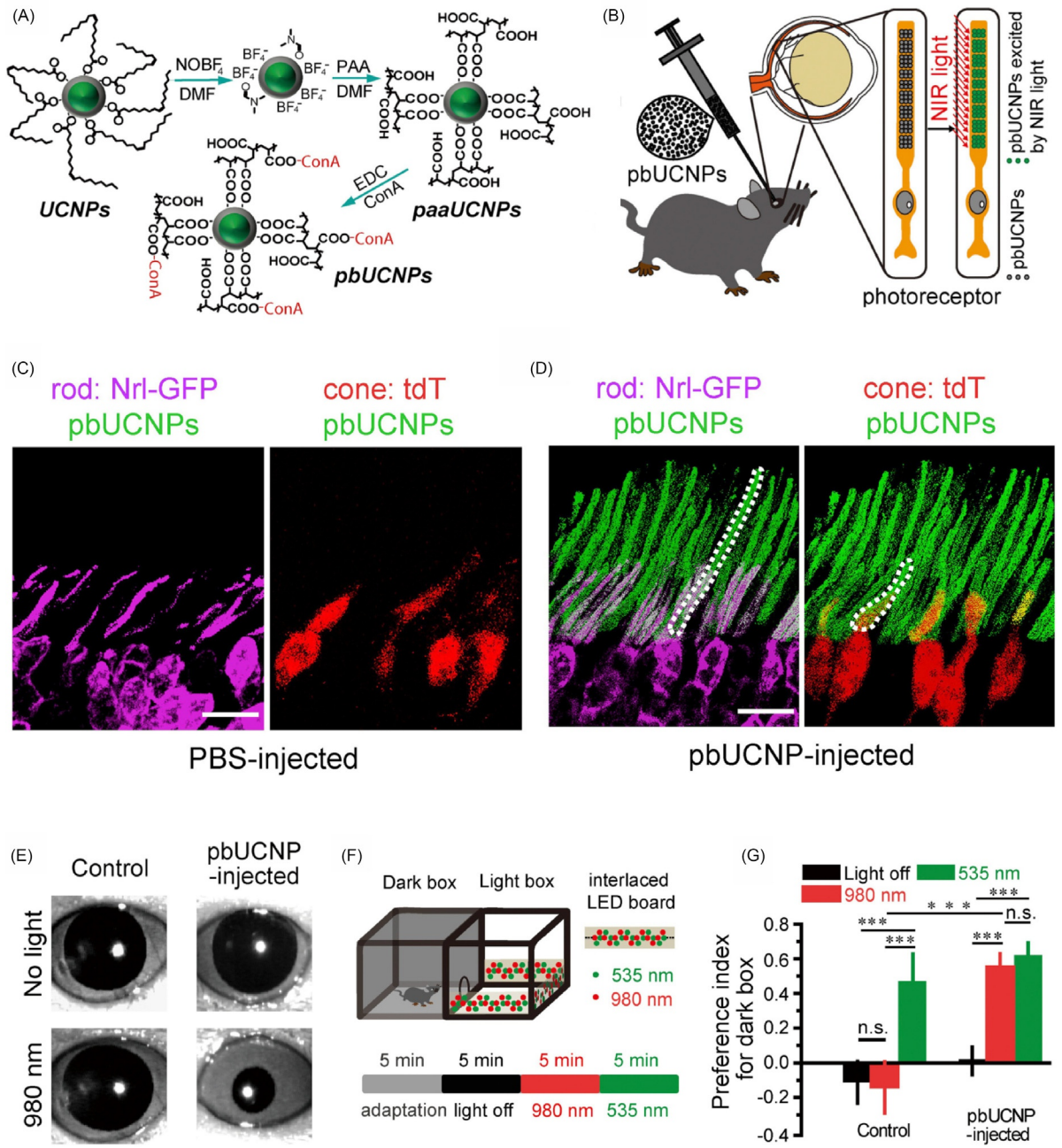

Fig. 41 (A) Surface modification of ConA-functionalized, photoreceptor-binding green-emitting upconversion nanoparticles (pbUCNPs). (B) Illustration of sub-retinal injection of modified upconversion nanocrystals in mice. (C–D) Overlaid green (pbUCNPs)/violet (rods) and green (pbUCNPs)/red (cones) channel fluorescence images of retina from PBS-injected mice (C) and pbUCNP-injected mice (D). Scale bars, 10 μm. (E) Images of pupil constriction from non-injected controls and pbUCNP-injected mice under 980-nm illumination. (F) Light-dark box experiment diagram. (G) Preference index for dark box under three different lightbox conditions (light off, 980 nm, and 535 nm). Printed with permission from Ref. Ma, Y. et al. *Cell* **2019**, *177*, 243–255. Copyright © 2019 Elsevier Inc.

converting NIR excitation to green emission can be constructed. As evidenced in Fig. 41E, strong pupil constriction of nanocrystal-injected mice can be triggered upon 980-nm illumination. However, no response was detected in non-injected control mice, indicating that injection of nanocrystals enhances NIR vision. Furthermore, the light-dark box experiment (Fig. 41F and G) shows that nanocrystal-injected mice exhibit a significant preference for a dark box, whereas non-injected control mice cannot distinguish the NIR-illuminated dark box.

By introducing Nd^{3+} or Er^{3+} sensitization at 730, 800, 860, and 1532 nm, current NIR vision can be further broadened. Beyond vision enhancement, this approach may serve as an integrated, light-controlled nanosystem for visual function correction.

6 Conclusion

Fundamental study of photon upconversion in nanomaterials has been explored, and customization of upconversion phosphors with a targeted physical dimension, morphology, and specific optical properties is no longer a challenging task. In the next decade, one crucial mission will be to optimize available materials further and promote their practical applications. New mechanisms based on lanthanide-doped upconversion may be developed for super-resolution imaging that offers low power and fast imaging in deep tissues. Moreover, small (<5 nm), bright upconversion nanocrystals are anticipated to improve cell labeling. For nano/microcavity lasing, directional, single-mode laser output with programmable emission wavelengths upon low-power CW beam pumping at room temperature is still challenging. Upconversion nanocrystals with orthogonal excitation/emission features may be an alternative to achieve this goal. Furthermore, improving the NIR-to-Vis efficiency of upconversion nanocrystals will facilitate upconversion-mediated optogenetics in deep tissues. In addition to consolidating the above applications, we should further explore applications of lanthanide-doped upconversion nanomaterials in nanophotonics and biophotonics. With a better understanding of the stimulus-response model of emission behavior, disruptive technical innovations may enable significant advances in conversion efficiency and sensitivity.

References

1. Wang, F.; Liu, X. *Chem. Soc. Rev.* **2009**, *38*, 976–989.
2. Liu, X.; Yan, C.-H.; Capobianco, J. A. *Chem. Soc. Rev.* **2015**, *44*, 1299–1301.
3. Zhou, J.; Liu, Q.; Feng, W.; Sun, Y.; Li, F. *Chem. Rev.* **2015**, *115*, 395–465.
4. Boyer, J.-C.; Van Veggel, F. C. *Nanoscale* **2010**, *2*, 1417–1419.
5. Sun, L.-D.; Dong, H.; Zhang, P.-Z.; Yan, C.-H. *Annu. Rev. Phys. Chem.* **2015**, *66*, 619–642.
6. Bünzli, J.-C. G.; Piguet, C. *Chem. Soc. Rev.* **2005**, *34*, 1048–1077.
7. Dong, H.; et al. *ACS Nano* **2017**, *11*, 3289–3297.
8. Wang, H.; Duan, C.-K.; Tanner, P. A. *J. Phys. Chem. C* **2008**, *112*, 16651–16654.
9. Bünzli, J.-C. G. *Chem. Rev.* **2010**, *110*, 2729–2755.
10. Liang, L.; Qin, X.; Zheng, K.; Liu, X. *Acc. Chem. Res.* **2019**, *52*, 228–236.
11. Wang, Y.; et al. *Chem. Soc. Rev.* **2018**, *47*, 6473–6485.
12. Qin, X.; Xu, J.; Wu, Y.; Liu, X. *ACS Cent. Sci.* **2019**, *5*, 29–42.
13. Johnson, N. J.; van Veggel, F. C. *Nano Res.* **2013**, *6*, 547–561.
14. Fischer, S.; Johnson, N. J.; Pichaandi, J.; Goldschmidt, J. C.; van Veggel, F. C. *J. Appl. Phys.* **2015**, *118, 193105.*
15. Vetrone, F.; Naccache, R.; Mahalingam, V.; Morgan, C. G.; Capobianco, J. A. *Adv. Funct. Mater.* **2009**, *19*, 2924–2929.
16. Zhou, J.; Liu, Z.; Li, F. *Chem. Soc. Rev.* **2012**, *41*, 1323–1349.
17. Zhou, B.; Shi, B.; Jin, D.; Liu, X. *Nat. Nanotechnol.* **2015**, *10*, 924–936.
18. Li, Z.; Yuan, H.; Yuan, W.; Su, Q.; Li, F. *Coord. Chem. Rev.* **2018**, *354*, 155–168.
19. Zheng, K.; et al. *Nano Today* **2019**, *29*, 100797.
20. Bogdan, N.; Vetrone, F.; Ozin, G. A.; Capobianco, J. A. *Nano Lett.* **2011**, *11*, 835–840.
21. Bünzli, J.-C. G. *JOL* **2016**, *170*, 866–878.
22. Zhou, J.; et al. *Small* **2018**, *14*, 1801882.
23. Wang, Y.; Song, S.; Zhang, S.; Zhang, H. *Nano Today* **2019**, *25*, 38–67.
24. Yan, J.; Li, B.; Yang, P.; Lin, J.; Dai, Y. *Adv. Funct. Mater.* **2021**, 2104325.
25. Liu, Z.; et al. *Biomaterials* **2013**, *34*, 7444–7452.
26. Yang, D.; Hou, Z.; Cheng, Z.; Li, C.; Lin, J. *Chem. Soc. Rev.* **2015**, *44*, 1416–1448.
27. Yang, Y.; et al. *Angew. Chem. Int. Ed.* **2012**, *124*, 3179–3183.
28. Zhan, Q.; et al. *Nat. Commun.* **2017**, *8*, 1058.
29. Liu, Y.; et al. *Nature* **2017**, *543*, 229–233.
30. Liang, L.; Liu, X. *Chem* **2017**, *2*, 331–333.
31. De Camillis, S.; et al. *Nanoscale* **2020**, *12*, 20347–20355.
32. Liang, L.; et al. *Nat. Nanotechnol.* **2021**, *16*, 975–980.
33. Fernandez-Bravo, A.; et al. *Nat. Nanotechnol.* **2018**, *13*, 572–577.
34. Fernandez-Bravo, A.; et al. *Nat. Mater.* **2019**, *18*, 1172–1176.
35. Yang, X. F.; Lyu, Z. Y.; Dong, H.; Sun, L. D.; Yan, C. H. *Small* **2021**, 2103140.
36. Ji, Y.; et al. Light. *Sci. Appl.* **2020**, *9*, 184.
37. Ji, Y.; et al. *Nano Energy* **2019**, *61*, 211–220.
38. Lian, H.; et al. *Energy* **2013**, *57*, 270–283.
39. Chen, S.; et al. *Science* **2018**, *359*, 679–684.
40. Wang, Z.; Hu, M.; Ai, X.; Zhang, Z.; Xing, B. *Adv. Biosyst.* **2019**, *3*, 1800233.
41. Wu, X.; et al. *ACS Nano* **2016**, *10*, 1060–1066.
42. Zhai, Y.; et al. *Nano Energy* **2020**, *67*, 104262.
43. Shah, S.; et al. *Nanoscale* **2015**, *7*, 16571–16577.
44. Bansal, A.; Liu, H.; Jayakumar, M. K. G.; Andersson-Engels, S.; Zhang, Y. *Small* **2016**, *12*, 1732–1743.
45. Liang, L.; et al. *Nat. Commun.* **2019**, *10*, 1391.
46. Ai, X.; et al. *Angew. Chem. Int. Ed.* **2017**, *56*, 3031–3035.
47. Pawlicki, M.; Collins, H. A.; Denning, R. G.; Anderson, H. L. *Angew. Chem. Int. Ed.* **2009**, *48*, 3244–3266.
48. Venkatakrishnarao, D.; et al. *Adv. Mater.* **2017**, *29*, 1605260.
49. Chu, S.-W.; et al. *Opt. Lett.* **2005**, *30*, 2463–2465.
50. Kawamoto, Y.; Kanno, R.; Qiu, J. *J. Mater. Sci.* **1998**, *33*, 63–67.
51. Yin, W.; et al. *Chem. A Eur. J.* **2012**, *18*, 9239–9245.

52. Zhou, B.; Yang, W.; Han, S.; Sun, Q.; Liu, X. *Adv. Mater.* **2015**, *27*, 6208–6212.
53. Wang, F.; et al. *Nat. Mater.* **2011**, *10*, 968–973.
54. Li, X.; et al. *Angew. Chem. Int. Ed.* **2015**, *54*, 13312–13317.
55. Homann, C.; et al. *Angew. Chem. Int. Ed.* **2018**, *57*, 8765–8769.
56. Kaiser, M.; et al. *Nanoscale* **2017**, *9*, 10051–10058.
57. Zhan, Q.; et al. *ACS Nano* **2011**, *5*, 3744–3757.
58. Huang, X. *J. Alloys Compd.* **2017**, *690*, 356–359.
59. Liang, L.; et al. *Chem. A Eur. J.* **2016**, *22*, 10801–10807.
60. Xie, X.; et al. *J. Am. Chem. Soc.* **2013**, *135*, 12608–12611.
61. Xie, X.; et al. *Small* **2017**, *13*, 1602843.
62. Zhong, Y.; et al. *Adv. Mater.* **2014**, *26*, 2831–2837.
63. Hao, S.; et al. *Nanoscale* **2017**, *9*, 6711–6715.
64. Zou, W.; Visser, C.; Maduro, J. A.; Pshenichnikov, M. S.; Hummelen, J. C. *Nat. Photon.* **2012**, *6*, 560–564.
65. Wang, X.; et al. *Chem. Soc. Rev.* **2017**, *46*, 4150–4167.
66. Han, S.; et al. *Nature* **2020**, *587*, 594–599.
67. Popov, A.; et al. *J. Alloys Compd.* **2020**, *822*, 153654.
68. Alvarez-Ramos, M. E. *J. Alloys Compd.* **2021**, *854*, 157076.
69. Gargas, D. J.; et al. *Nat. Nanotechnol.* **2014**, *9*, 300–305.
70. Zhao, J.; et al. *Nat. Nanotechnol.* **2013**, *8*, 729–734.
71. Wei, W.; et al. *J. Am. Chem. Soc.* **2016**, *138*, 15130–15133.
72. Wang, J.; Wang, F.; Wang, C.; Liu, Z.; Liu, X. *Angew. Chem. Int. Ed.* **2011**, *123*, 10553–10556.
73. Wang, H.; et al. *J. Alloys Compd.* **2015**, *618*, 776–780.
74. Chen, Q.; et al. *Angew. Chem. Int. Ed.* **2017**, *129*, 7713–7717.
75. Wang, J.; et al. *Nat. Mater.* **2014**, *13*, 157–162.
76. Wang, F.; Wang, J.; Liu, X. *Angew. Chem. Int. Ed.* **2010**, *49*, 7456–7460.
77. Su, Q.; et al. *J. Am. Chem. Soc.* **2012**, *134*, 20849–20857.
78. Johnson, N. J. J.; et al. *J. Am. Chem. Soc.* **2017**, *139*, 3275–3282.
79. Zhang, F.; et al. *Nano Lett.* **2012**, *12*, 2852–2858.
80. Würth, C.; Fischer, S.; Grauel, B.; Alivisatos, A. P.; Resch-Genger, U. *J. Am. Chem. Soc.* **2018**, *140*, 4922–4928.
81. Xu, X.; et al. *APL Photonics* **2019**, *4*, 026104.
82. Han, S.; Deng, R.; Xie, X.; Liu, X. *Angew. Chem. Int. Ed.* **2014**, *53*, 11702–11715.
83. Amendola, V.; Pilot, R.; Frasconi, M.; Maragò, O. M.; Iatì, M. A. *J. Phys. Condens. Matter* **2017**, *29*, 203002.
84. Chen, Y.; Ming, H. *Photonic Sens.* **2012**, *2*, 37–49.
85. Törmä, P.; Barnes, W. L. *Rep. Prog. Phys.* **2014**, *78*, 013901.
86. Zijlstra, P.; Paulo, P. M. R.; Orrit, M. *Nat. Nanotechnol.* **2012**, *7*, 379–382.
87. Cao, J.; Sun, T.; Grattan, K. T. *Sens. Actuators B* **2014**, *195*, 332–351.
88. Saboktakin, M.; et al. *ACS Nano* **2012**, *6*, 8758–8766.
89. Mauser, N.; et al. *ACS Nano* **2015**, *9*, 3617–3626.
90. Zhang, C.; Lee, J. Y. *J. Phys. Chem. C* **2013**, *117*, 15253–15259.
91. Xu, W.; Chen, X.; Song, H. *Nano Today* **2017**, *17*, 54–78.
92. Yin, Z.; et al. *Adv. Mater.* **2016**, *28*, 2518–2525.
93. Zhang, F.; Deng, Y.; Shi, Y.; Zhang, R.; Zhao, D. *J. Mater. Chem.* **2010**, *20*, 3895–3900.
94. Li, Z.-X.; et al. *Chem. Commun.* **2009**, 6616–6618.
95. Hu, X.; et al. *Chem. Sci.* **2017**, *8*, 466–472.
96. Mao, C.; et al. *ACS Photon.* **2019**, *6*, 1882–1888.
97. Yin, Z.; et al. *Chem. Commun.* **2013**, *49*, 3781–3783.
98. Liao, J.; et al. *J. Mater. Chem. C* **2013**, *1*, 6541–6546.
99. Hao, S.; et al. *Nanoscale* **2017**, *9*, 10633–10638.
100. Chen, G.; et al. *Nano Lett.* **2015**, *15*, 7400–7407.
101. Chen, G.; et al. *Adv. Opt. Mater.* **2016**, *4*, 1760–1766.
102. Lee, J.; et al. *Adv. Mater.* **2017**, *29*, 1603169.
103. Garfield, D. J.; et al. *Nat. Photon.* **2018**, *12*, 402–407.
104. Das, A.; Mao, C.; Cho, S.; Kim, K.; Park, W. *Nat. Commun.* **2018**, *9*, 4828.
105. Wu, Y.; et al. *Nat. Nanotechnol.* **2019**, *14*, 1110–1115.
106. Liu, H.; et al. *Adv. Mater.* **2019**, *31*, 1807900.
107. Heifetz, A.; Simpson, J. J.; Kong, S.-C.; Taflove, A.; Backman, V. *Opt. Express* **2007**, *15*, 17334–17342.
108. Liu, C.-Y.; Wang, Y.-H. *Physica E* **2014**, *61*, 141–147.
109. Liu, C.-Y.; Lin, F.-C. *Optics Commun.* **2016**, *380*, 287–296.
110. Li, Y.; et al. *ACS Nano* **2017**, *11*, 10672–10680.
111. Peng, X.; et al. *Nanoscale* **2019**, *11*, 1563–1569.
112. Liu, B.; et al. *Nano Lett.* **2020**, *20*, 4775–4781.
113. Chen, C.; et al. *Nat. Commun.* **2018**, *9*, 3290.
114. Jin, D.; et al. *Nat. Methods* **2018**, *15*, 415–423.
115. Plöschner, M.; et al. *Opt. Express* **2020**, *28*, 24308–24326.
116. Denkova, D.; et al. *Nat. Commun.* **2019**, *10*, 3695.
117. Liang, L.; et al. *Angew. Chem. Int. Ed.* **2019**, *59*, 746–751.
118. Rittweger, E.; Han, K. Y.; Irvine, S. E.; Eggeling, C.; Hell, S. W. *Nat. Photon.* **2009**, *3*, 144–147.
119. Blom, H.; Widengren, J. *Chem. Rev.* **2017**, *117*, 7377–7427.
120. Hell, S. W.; Wichmann, J. *Opt. Lett.* **1994**, *19*, 780–782.
121. Theer, P.; Denk, W. *J. Opt. Soc. Am. A* **2006**, *23*, 3139–3149.
122. Wu, Q.; Huang, B.; Peng, X.; He, S.; Zhan, Q. *Opt. Express* **2017**, *25*, 30885–30894.
123. Wang, T.; et al. *ACS Photon.* **2017**, *4*, 1539–1543.
124. Wang, M.; Abbineni, G.; Clevenger, A.; Mao, C.; Xu, S. Nanomedicine: Nanotechnology. *Biol. Med.* **2011**, *7*, 710–729.

125. Lin, M.; et al. *Biotechnol. Adv.* **2012**, *30*, 1551–1561.
126. Liang, L.; et al. *Adv. Mater.* **2013**, *25*, 2174–2180.
127. Zhang, Y.; et al. *J. Am. Chem. Soc.* **2014**, *136*, 4893–4896.
128. Boyer, J.-C.; Vetrone, F.; Cuccia, L. A.; Capobianco, J. A. *J. Am. Chem. Soc.* **2006**, *128*, 7444–7445.
129. Chen, X.; et al. *Nat. Commun.* **2016**, *7*, 10304.
130. Fenno, L.; Yizhar, O.; Deisseroth, K. *Annu. Rev. Neurosci.* **2011**, *34*, 389–412.
131. Deisseroth, K. *Nat. Methods* **2011**, *8*, 26–29.
132. Yizhar, O.; Fenno, L. E.; Davidson, T. J.; Mogri, M.; Deisseroth, K. *Neuron* **2011**, *71*, 9–34.
133. Williams, S. C.; Deisseroth, K. *Proc. Natl. Acad. Sci.* **2013**, *110*, 16287–16288.
134. Dugué, G. P.; Akemann, W.; Knöpfel, T. *Progress in Brain Resarch*; Elsevier, 2012; vol. 196; pp. 1–28.
135. Cui, S.; et al. *ACS Nano* **2013**, *7*, 676–688.
136. Chen, G.; et al. *ACS Nano* **2012**, *6*, 8280–8287.
137. Chen, H.; et al. *Small* **2014**, *10*, 160–168.
138. Xiang, G.; et al. *Inorg. Chem.* **2020**, *59*, 11054–11060.
139. Gao, W.; et al. *Theranostics* **2016**, *6*, 1131–1144.
140. Jayakumar, M. K. G.; Idris, N. M.; Zhang, Y. *Proc. Natl. Acad. Sci.* **2012**, *109*, 8483–8488.
141. Sasaki, Y.; et al. *Angew. Chem. Int. Ed.* **2019**, *58*, 17827–17833.
142. Lin, X.; et al. *Adv. Healthc. Mater.* **2017**, *6*, 1700446.
143. Yu, N.; et al. *Adv. Healthc. Mater.* **2019**, *8*, 1801132.
144. Ma, Y.; et al. *Cell* **2019**, *177*, 243–255.